

Aus dem Institut für Neuro- und Sinnesphysiologie  
(Prof. Dr. rer. nat. S. O. Rizzoli)  
im Zentrum Physiologie und Pathophysiologie  
der Medizinischen Fakultät der Universität Göttingen

**A novel tool for neuronal physiology and  
pathology:  
optimization of secondary ion mass  
spectrometry approaches**

INAUGURAL-DISSERTATION

zur Erlangung des Doktorgrades  
der Medizinischen Fakultät der  
Georg-August-Universität zu Göttingen

vorgelegt von

**Paola Agüí González**

aus

Santa Cruz de Tenerife

Göttingen 2022

Dekan: Prof. Dr. med. W. Brück

### **Betreuungsausschuss**

Betreuer: Prof. Dr. rer. nat. S.O. Rizzoli

Ko-Betreuer: Prof. Dr. rer. nat. P. Rehling

### **Prüfungskommission**

Referent: Prof. Dr. rer. nat. S.O. Rizzoli

Ko-Referent: Prof. Dr. rer. nat. P. Rehling

Drittreferent: Prof. Dr. Mult. T. Meyer

Datum der mündlichen Prüfung: 11. May 2023

Some of the data on which the present dissertation is based has already been published:

Kabatas S, **Agüi-Gonzalez P**, Saal K, Jähne S, Opazo F, Rizzoli SO, Phan NTN (2019): Boron-Containing Probes for Non-optical High-Resolution Imaging of Biological Samples. *Angew Chemie Int Ed* 58, 3438–43

Kabatas S, **Agüi-Gonzalez P**, Hinrichs R, Jähne S, Opazo F, Diederichsen U, Rizzoli SO, Phan NTN (2019b): Fluorinated Nanobodies for Targeted Molecular Imaging of Biological Samples Using Nanoscale Secondary Ion Mass Spectrometry. *J Anal At Spectrom* 34, 1083–87

**Agüi-Gonzalez P**, Jähne S, Phan NTN (2019): SIMS Imaging in Neurobiology and Cell Biology. *J Anal At Spectrom* 34, 1355–68

**Agüi-Gonzalez P**, Guobin B, Gomes de Castro MA, Rizzoli SO, Phan NTN (2021a): Secondary Ion Mass Spectrometry Imaging Reveals Changes in the Lipid Structure of the Plasma Membranes of Hippocampal Neurons Following Drugs Affecting Neuronal Activity. *ACS Chem Neurosci* 12, 1542–51

**Agüi-Gonzalez P**, Dankovich TM, Rizzoli SO, Phan NTN (2021b): Gold-Conjugated Nanobodies for Targeted Imaging Using High-Resolution Secondary Ion Mass Spectrometry. *Nanomaterials* 11, 1797

Lange F\*, **Agüi-Gonzalez P\***, Riedel D, Phan NTN, Jakobs S, Rizzoli SO (2021): Correlative Fluorescence Microscopy, Transmission Electron Microscopy and Secondary Ion Mass Spectrometry (CLEM-SIMS) for Cellular Imaging. Edited by Stephane Gasman. *PLoS One* 16, e0240768

*\*both authors contributed equally to this work*

Meschkat M, Steyer AM, Weil M-T, Kusch K, Jahn O, Piepkorn L, **Agüi-Gonzalez P**, Phan NTN, Ruhwedel T, Sadowski B et al. (2022): White Matter Integrity in Mice Requires Continuous Myelin Synthesis at the Inner Tongue. *Nat Commun* 13, 1163

Hiermit erkläre ich, die Dissertation mit dem Titel "A novel tool for neuronal physiology and pathology: optimization of secondary ion mass spectrometry approaches" eigenständig angefertigt und keine anderen als die von mir angegebenen Quellen und Hilfsmittel verwendet zu haben.

Göttingen, den 28.07.2022

---

# TABLE OF CONTENTS

---

<b>TABLE OF CONTENTS</b> .....	<b>I</b>
<b>LIST OF FIGURES</b> .....	<b>III</b>
<b>LIST OF TABLES</b> .....	<b>V</b>
<b>LIST OF ABBREVIATIONS</b> .....	<b>VI</b>
<b>1. INTRODUCTION</b> .....	<b>1</b>
<b>1.1 GENERAL INTRODUCTION</b> .....	<b>1</b>
1.1.1 Thesis structure .....	1
1.1.2 Secondary Ion Mass Spectrometry.....	1
1.1.3 SIMS Modes.....	2
1.1.4 Fundamentals of SIMS.....	3
1.1.5 SIMS polarities.....	5
1.1.6 Imaging mass spectrometry.....	6
1.1.7 Sample preparation .....	7
1.1.8 Specific targets in biological samples.....	9
1.1.9 Mass analyzer types.....	9
<b>1.2 INTRODUCTION AIM I: STUDY OF THE PLASMA MEMBRANE LIPID DISTRIBUTION ON HIPPOCAMPAL NEURONS WITH TOF-SIMS</b> .....	<b>13</b>
1.2.1 Lipids.....	13
1.2.2 Lipid composition and physical properties of cellular membranes.....	19
1.2.3 Lipids in the nervous system.....	21
1.2.4 Membrane lipid analysis with ToF-SIMS .....	22
<b>1.3 INTRODUCTION AIM II: DUAL PROBES FOR BIOLOGICAL STUDIES</b> .....	<b>24</b>
1.3.1 Binding strategies .....	25
1.3.2 Nanoprobes.....	27
<b>1.4 INTRODUCTION AIM III: STUDY OF THE MYELIN TURNOVER COMBINING ELECTRON MICROSCOPY AND SECONDARY ION MASS SPECTROMETRY</b> .....	<b>27</b>
1.4.1 Imaging techniques correlation .....	27
1.4.2 Myelin.....	28
1.4.3 Myelin turnover .....	29
<b>1.5 INTRODUCTION AIM IV: CORRELATIVE FLUORESCENCE MICROSCOPY, TRANSMISSION ELECTRON MICROSCOPY AND SECONDARY ION MASS SPECTROMETRY (CLEM-SIMS)</b> .....	<b>30</b>
1.5.1 Imaging techniques correlation .....	30
1.5.2 CLEM-SIMS .....	31
<b>2. MATERIAL AND METHODS</b> .....	<b>33</b>
<b>2.1 MATERIAL AND METHODS AIM I</b> .....	<b>33</b>
2.1.1 Hippocampal neurons culture .....	33
2.1.2 Fixation methods .....	35
2.1.3 ToF-SIMS imaging.....	35
2.1.4 Mass spectra calibration .....	35
2.1.5 Data analysis.....	36
<b>2.2 MATERIAL AND METHODS AIM II</b> .....	<b>36</b>
2.2.1 Sample preparation for FluorLink .....	36

2.2.2	Sample preparation for BorEncode.....	37
2.2.3	Sample preparation for BorLink .....	38
2.2.4	Plastic embedding and sectioning.....	38
2.2.5	SIMS imaging.....	38
2.2.6	Data analysis.....	39
<b>2.3</b>	<b>MATERIAL AND METHODS AIM III.....</b>	<b>39</b>
2.3.1	Sample preparation: 13C-labeling .....	39
2.3.2	Sample sectioning and mounting .....	39
2.3.3	NanoSIMS imaging.....	40
2.3.4	Image registration.....	40
2.3.5	Isotopic enrichment calculation .....	41
<b>2.4</b>	<b>MATERIAL AND METHODS AIM IV .....</b>	<b>41</b>
2.4.1	Sample preparation for high-accuracy CLEM .....	41
2.4.2	NanoSIMS imaging.....	41
2.4.3	Image registration.....	42
2.4.4	Calculation of isotopic enrichment .....	42
<b>3.</b>	<b>RESULTS.....</b>	<b>43</b>
<b>3.1</b>	<b>RESULTS AIM I .....</b>	<b>43</b>
3.1.1	Sample preparation .....	44
3.1.2	Neighborhood cross-correlation coefficients (NBCC) and independent component analysis (ICA) to uncover the lipid organization across different plasma membrane regions. ....	45
3.1.3	Independent components content.....	47
3.1.4	Study of the neuronal membrane lipid composition after drug treatment by cross-correlation coefficient difference analysis. ....	48
3.1.5	Drug treatments induce particular lipids subclasses changes on hippocampal neuronal plasma membranes. ....	50
3.1.6	Lipid distribution of hippocampal neuronal plasma membranes and its link to homeostatic plasticity. ....	55
<b>3.2</b>	<b>RESULTS AIM II.....</b>	<b>57</b>
3.2.1	Fluorinated nanobodies: FluorLink .....	57
3.2.2	Boron containing-probes: BorEncode and BorLink .....	60
<b>3.3</b>	<b>RESULTS AIM III .....</b>	<b>65</b>
<b>3.4</b>	<b>RESULTS AIM IV.....</b>	<b>67</b>
3.4.1	Sample preparation .....	67
3.4.2	NanoSIMS imaging.....	67
3.4.3	CLEM-SIMS image and data analysis .....	68
<b>4.</b>	<b>DISCUSSION.....</b>	<b>71</b>
<b>4.1</b>	<b>GENERAL DISCUSSION .....</b>	<b>71</b>
<b>4.2</b>	<b>DISCUSSION AIM I .....</b>	<b>74</b>
<b>4.3</b>	<b>DISCUSSION AIM II .....</b>	<b>74</b>
<b>4.4</b>	<b>DISCUSSION AIM III .....</b>	<b>75</b>
<b>4.5</b>	<b>DISCUSSION AIM IV .....</b>	<b>75</b>
<b>4.6</b>	<b>FINAL CONCLUSIONS .....</b>	<b>77</b>
<b>5.</b>	<b>APPENDIX .....</b>	<b>79</b>
<b>6.</b>	<b>BIBLIOGRAPHY.....</b>	<b>88</b>

## LIST OF FIGURES

---

<b>Figure 1.</b> Secondary Ion Mass Spectrometry principle. ....	2
<b>Figure 2.</b> Periodic table showing the best polarity to enhance the yield of each element. ....	6
<b>Figure 3.</b> Imaging mass spectrometry. ....	6
<b>Figure 4.</b> 2D imaging with ToF-SIMS. ....	7
<b>Figure 5.</b> 3D mass spectrometry imaging. ....	7
<b>Figure 6.</b> Quadrupole mass spectrometer. ....	10
<b>Figure 7.</b> Orbitrap. ....	10
<b>Figure 8.</b> Time of flight SIMS scheme. ....	11
<b>Figure 9.</b> NanoSIMS 50L scheme. ....	12
<b>Figure 10.</b> Coaxial configuration. ....	12
<b>Figure 11.</b> Ketoacyl and isoprene subunits. ....	14
<b>Figure 12.</b> Examples of saturated and unsaturated fatty acids. ....	14
<b>Figure 13.</b> Triacylglycerols formation. ....	15
<b>Figure 14.</b> Scheme of GPs structure. ....	16
<b>Figure 15.</b> Representative phosphatidic acid structure. ....	16
<b>Figure 16.</b> 2D structure of a phosphatidylcholine molecule. ....	17
<b>Figure 17.</b> General sphingolipid structures. ....	18
<b>Figure 18.</b> 3D structure of a cholesterol molecule. ....	18
<b>Figure 19.</b> Structure of Kdo2-Lipid A. ....	19
<b>Figure 20.</b> Examples of a polyketide structure. 3D structure of a Cyanidin molecule. ....	19
<b>Figure 21.</b> Schematic representation of a eukaryotic plasma membrane. ....	19
<b>Figure 22.</b> Membrane lipid composition and physical properties. ....	20
<b>Figure 23.</b> Lipid geometry influences membrane curvature. ....	21
<b>Figure 24.</b> Ionoptika J105 scheme. ....	23
<b>Figure 25.</b> Comparison of nanobodies and antibodies. ....	25
<b>Figure 26.</b> Strategies to bind conjugated probes to cellular proteins. ....	26
<b>Figure 27.</b> Clickable nanoprobe binding strategies. ....	26
<b>Figure 28.</b> Myelination in the peripheral and central nervous systems. ....	29
<b>Figure 29.</b> Myelin sheaths formation stages. A) ....	29
<b>Figure 30.</b> Workflow overview for CLEM-SIMS imaging. ....	32
<b>Figure 31.</b> Banker culture workflow. ....	33
<b>Figure 32.</b> TEM low magnification overview of a finder grid used as a guide to locate the same area of interest with NanoSIMS CCD. ....	40
<b>Figure 33.</b> Comparison of sample preparation methods for ToF-SIMS imaging of hippocampal neurons. ....	45
<b>Figure 34.</b> Representative images of the masks after applying a Gaussian mixture model. ....	46
<b>Figure 35.</b> Representative example of the first 9 ICs of each category. ....	46
<b>Figure 36.</b> NanoSIMS imaging of vGlut in rat hippocampal neurons employing Au anti-vGlut1 nanobody. ....	47
<b>Figure 37.</b> Cross-correlation coefficient differences analysis. ....	49
<b>Figure 38.</b> 3D representation of the relative changes trends of different membrane lipid subclasses following TTX or BIC treatments. ....	56
<b>Figure 39.</b> Scheme of a FluorLink nanobody. ....	58
<b>Figure 40.</b> Co-localization of ROIs using fluorescence and CCD camera images. ....	58
<b>Figure 41.</b> Direct targeting of specific proteins for fluorescence microscopy and NanoSIMS with FluorLink-nanobody. ....	59
<b>Figure 42.</b> NanoSIMS imaging of indirectly labeled proteins with FluorLink. ....	59
<b>Figure 43.</b> Boron containing-probes. ....	60

---

<b>Figure 44.</b> Incorporation of HPG in BHK cells enables the labeling of all newly synthesized proteins with BorEncode. ....	<b>61</b>
<b>Figure 45.</b> Site-specific labeling with BorEncode of BHK cells expressing PRK-modified syntaxin-1. ....	<b>62</b>
<b>Figure 46.</b> Large-scale light microscopy image of COS-7 cells immunostained with BorLink-antiGFP-Nbs. ....	<b>63</b>
<b>Figure 47.</b> COS-7 cells expressing TOM70-GFP labeled with anti-GFP BorLink nanobodies. ....	<b>64</b>
<b>Figure 48.</b> Myelin turnover analysis with <sup>13</sup> C-lysine feeding and NanoSIMS imaging in MBP iKO. ....	<b>66</b>
<b>Figure 49.</b> TEM and NanoSIMS imaging of MBP iKO spinal cord after 60 d <sup>13</sup> C-lysine diet feeding. ....	<b>67</b>
<b>Figure 50.</b> Detailed views of CLEM-SIMS. ....	<b>68</b>
<b>Figure 51.</b> Analysis of CLEM-SIMS data determines isotopic distribution differences between cellular compartments in cultured HeLa cells ....	<b>70</b>
<b>Figure 52.</b> CLEM-SIMS lateral resolutions. ....	<b>71</b>



---

## LIST OF TABLES

---

<b>Table 1.</b> Peak composition of the main ICs at the plasma membrane of the cell body and neurites.....	<b>48</b>
<b>Table 2.</b> Tentative peak assignment in positive and negative SIMS mode.....	<b>51</b>
<b>Table 3.</b> Lipids and fragments significantly affected after drug treatments.....	<b>54</b>
<b>Table 4.</b> Relative changes of lipid subclasses in the plasma membrane of hippocampal neurons after their incubation with TTX and BIC.....	<b>55</b>

---

**LIST OF ABBREVIATIONS**

---

<b>Ab</b>	Antibody
<b>AD</b>	Alzheimer's disease
<b>amu</b>	Atomic mass unit
<b>AS</b>	Aperture slit
<b>BIC</b>	Bicuculline
<b>BHK</b>	Baby hamster kidney cells
<b>CCCC</b>	Cross correlation coefficient change
<b>CCD</b>	Cross correlation difference
<b>CL</b>	Cardiolipin
<b>CLEM</b>	Correlated light and electron microscopy Correlated light, electron microscopy and secondary ion mass
<b>CLEM-SIMS</b>	spectrometry
<b>CNS</b>	Central nervous system
<b>CuAAC</b>	Copper(I)-catalyzed azide-alkyne cycloaddition
<b>DAG</b>	Diacylglycerols
<b>DMEM</b>	Dulbecco's modified eagle medium
<b>EM</b>	Electron microscopy
<b>ES</b>	Entrance slit
<b>FA</b>	Fatty acid
<b>GA</b>	Glutaraldehyde
<b>GCIB</b>	Gas cluster ion beams
<b>GFP</b>	Green fluorescent protein
<b>GL</b>	Glycerolipid
<b>GMM</b>	Gaussian mixture model
<b>GP</b>	Glycerophospholipid
<b>HBSS</b>	Hanks' Balanced Salt Solution
<b>hcAbs</b>	Heavy chain antibodies
<b>HEPES</b>	(4-(2-hydroxyethyl)-1-piperazineethanesulfonic acid)
<b>HPG</b>	Homopropargyl-L-glycine
<b>IC</b>	Independent component
<b>ICA</b>	Independent component analysis
<b>iKO</b>	Inducible knockout mice
<b>IMS</b>	Imaging mass spectrometry
<b>IP3</b>	Inositol triphosphate
<b>ITO</b>	Indium tin oxide
<b>LMIG</b>	Liquid metal ion guns
<b>m/z</b>	Mass to charge ratio
<b>MAG</b>	Monoacylglycerols
<b>MBP</b>	Myelin basic protein
<b>MRP</b>	Mass resolution power
<b>MS</b>	Mass spectrometry
<b>MVA</b>	Multivariate analysis

---

<b>NanoSIMS</b>	Nano-scale secondary ion mass spectrometry
<b>Nb</b>	Nanobody
<b>NBCC</b>	Neighborhood cross-correlation coefficient
<b>PA</b>	Phosphatidic acid
<b>PBS</b>	Phosphate buffered saline
<b>PC</b>	Phosphatidylcholines
<b>PCA</b>	Principal component analysis
<b>PD</b>	Parkinson 's disease
<b>PE</b>	Phosphatidylethanolamine
<b>PFA</b>	Paraformaldehyde
<b>PG</b>	Phosphatidylglycerol
<b>PI</b>	Phosphatidylinositol
<b>PIP</b>	Phosphoinositide
<b>PK</b>	Polyketide
<b>PKC</b>	Protein kinase C
<b>PNS</b>	Peripheral nervous system
<b>POI</b>	Protein of interest
<b>ppb</b>	parts per billion
<b>ppm</b>	parts per million
<b>PR</b>	Prenol
<b>PRK</b>	Propargyl-l-lysine
<b>PS</b>	Phosphatidylserine
<b>pti</b>	Post tamoxifen injection
<b>PUFA</b>	Polyunsaturated fatty acid
<b>RF</b>	Radio frequency
<b>ROI</b>	Region of interest
<b>RT</b>	Room Temperature
<b>sdAb</b>	Single domain antibody
<b>SEM</b>	Scanning electron microscopy
<b>SILAC</b>	Stable isotope-labeled amino acids
<b>SIMS</b>	Secondary ion mass spectrometry
<b>SL</b>	Saccharolipid
<b>SM</b>	Sphingomyelin
<b>SP</b>	Sphingolipid
<b>ST</b>	Sterol
<b>TEM</b>	Transmission electron microscopy
<b>TG</b>	Triacylglycerol
<b>TOF</b>	Time of flight
<b>TTX</b>	Tetrodotoxin
<b>UAA</b>	Unnatural amino acid
<b>VH</b>	Variable domain of the heavy chain
<b>VHH</b>	Variable domain of the hcAbs / Nanobody
<b>VL</b>	Variable domain of the light chain
<b>YFP</b>	Yellow fluorescent protein

# 1. INTRODUCTION

---

## 1.1 GENERAL INTRODUCTION

### 1.1.1 Thesis structure

Since the work here included comprehends different projects that are not directly related, this thesis has been divided in four aims:

Aim I: Study of the plasma membrane lipid distribution on hippocampal neurons with ToF-SIMS

Aim II: Dual probes for biological studies

Aim III: Study of the myelin turnover combining electron microscopy and secondary ion mass spectrometry

Aim IV: Correlative fluorescence microscopy, transmission electron microscopy and secondary ion mass spectrometry (CLEM-SIMS)

Within each main section (1. Introduction, 2. Material and methods, 3. Results and 4. Discussion), a subsection that describes the particular details of each aim can be found.

### 1.1.2 Secondary Ion Mass Spectrometry

Mass spectrometry (MS) is an analytical technique that allows the sorting of ions according to their mass-to-charge ratio ( $m/z$ ). MS is used in many different fields to analyze the chemical composition of pure samples as well as highly complex mixtures. The obtained mass spectra can describe the molecular, elemental, and isotopic composition of the samples.

Secondary ion mass spectrometry (SIMS) is an MS technique used to determine the chemical composition of solid samples and thin films. To obtain the secondary ions, SIMS instruments bombard the surface of the sample with a highly focused beam of ions (in a range from  $< 1$  to tens of keV). The impact of this primary ion beam produces the emission of secondary particles; neutral molecules, atoms, and ions (**Figure 1**). Due to their charge, only the secondary ions can be extracted and driven through a mass analyzer. In this section of the mass spectrometer, they are sorted accordingly to their mass to charge ratio ( $m/z$ ) while their abundance is recorded. Determining in this way the elemental, isotopic, or molecular composition of the analyzed surface.

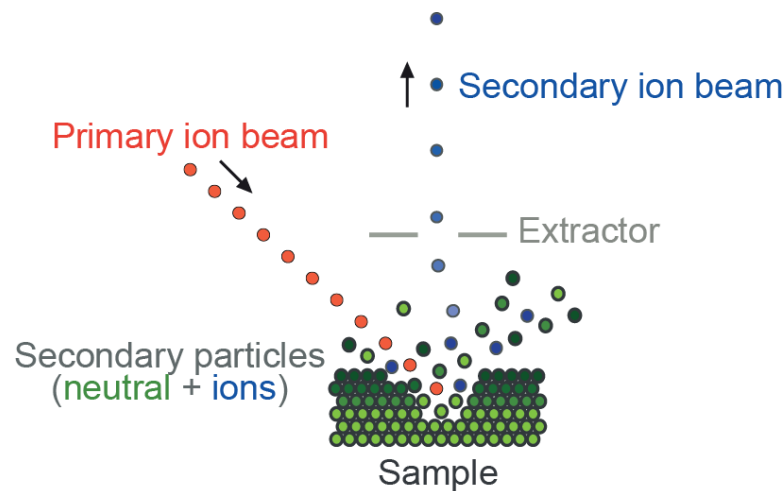


**Figure 1. Secondary Ion Mass Spectrometry principle.** The primary ion beam sputters the sample surface producing secondary particles, which include neutrals and ions. The secondary ions are then extracted into the mass spectrometer. Figure adapted from Agüi-Gonzalez et al. (2019), courtesy of the Royal Society of Chemistry.

According to their components and arrangement, there are multiple SIMS modalities. Across different SIMS instruments, the main differences are related to the primary ion sources and the type of mass spectrometers. Presenting different advantages and disadvantages, each configuration is useful to collect particular ranges of secondary ion species, achieving different levels of sensitivity, transmission, mass, and spatial resolutions (Gorman and Kraft 2020).

### 1.1.3 SIMS Modes

All SIMS techniques require the sputtering of secondary particles from the sample surface which are later analyzed by a mass spectrometer. However, depending on the level of destruction and chemical damage (fracture of the molecules in smaller fragments), SIMS techniques are divided in two modes: static and dynamic.

#### 1.1.3.1 Static mode

The primary ion dose remains below the static limit ( $10^{13}$  ions/cm<sup>2</sup>) (Massonnet and Heeren 2019). This dose causes just a small chemical damage since less than 1 % of the surface particles receive an impact. This mode ensures that the chemical information is obtained from an almost non-altered surface unraveling the composition of the uppermost layer.

#### 1.1.3.2 Dynamic mode

When the primary ion dose overpasses the static limit, and the number of incident ions exceeds the number of surface atoms (Pacholski and Winograd 1999), the sample is eroded while imaging takes place, meaning that the next layer of molecules gets exposed. Despite the emergence of new primary ion sources such as the Gas Cluster Ion Beams (GCIB) which allows the procurance of almost intact ions (Guerquin-Kern et al. 2005; Hanrieder et al. 2013b), the dynamic mode enhances the secondary ion yield but also increases the fragmentation level. This mode also offers the possibility of obtaining 3D images.

To calculate the primary ion dose the following equation is used:

$$\text{Primary ion dose} = \frac{I_p \cdot t}{A}$$

Being  $I_p$  the primary ion flux (ions/s),  $t$  represents the analysis time in seconds and,  $A$  the sputtered area of the surface in  $\text{cm}^2$  (Oran 2005).

Traditionally, the primary ion dose is what determines if a static or dynamic SIMS analysis is performed. Yet, since the new primary sources are way less harmful than the older ones, the line between statics and dynamics is getting diffuse. Furthermore, some techniques combine both modes, using a dual beam. While a big cluster of ions is used to erode the sample (dynamic mode), usually a liquid metal ion beam is applied for the imaging working under the static limit (Tian et al. 2016; Fletcher 2015).

#### 1.1.4 Fundamentals of SIMS

The following is the main SIMS equation and resolves the intensity of the secondary ions for a concrete species ( $m$ ):

$$I_s^m = I_p \cdot Y_m \cdot \alpha \theta^m \cdot \eta$$

On this equation,  $I_s^m$  represents the secondary ion current (counts/s) for a charged species.  $I_p$  refers to the primary ion flux (ions/s),  $Y_m$  to the total secondary sputtered yield (neutral and ionic particles) per primary impact,  $\alpha$  represents the ionization probability of the particular species (in positive or negative ion mode) and  $\theta^m$  refers to the fractional concentration of such species within the surface layer and  $\eta$  to the transmission efficiency of the instrument (Popczun et al. 2017; Oran 2005).

##### 1.1.4.1 Primary ion beam

To produce ionization and molecular desorption, the energy of the primary ions has to be strong enough. The higher the energy, the bigger the yield of secondary ions, but despite it is not linear, a high energy also brings more fragmentation (causing the loss of chemical information) and a bigger disturbance of the sub-surface layers (precluding depth profiling and 3D imaging). Although the fragmentation grade and the spatial resolution partially rely on the species of interest, the projectile features play a key role (Adams et al. 2016).

There are two main groups of SIMS sources, monatomic and polyatomic. Monatomic projectiles such as  $\text{In}^+$ ,  $\text{Au}^+$ ,  $\text{Cs}^+$  or  $\text{O}^+$ , can be focused on very small spot sizes offering great lateral resolutions. However, due to their high energy per atom, they damage the chemical structure of the subsurface layers and cause a huge fragmentation of the secondary species, providing only monatomic or very small fragments. Monatomic sources are often used in dynamic SIMS.

On the contrary, polyatomic sources serve to preserve the chemical information since they cause much less fragmentation and sub-surface damage. It has also been shown that for the analysis of biological samples, polyatomic sources help to enhance the secondary ion yield, especially for high mass species. Within the polyatomic sources, several types are included. Liquid metal ion guns (LMIG) are formed by small ion-clusters, such as  $\text{Au}_3^+$  or  $\text{Bi}_3^+$ . They combine the best lateral resolution among the polyatomic sources and a high secondary yield (Kollmer 2004). However, their use is limited by the chemical damage and the disturbance of the sub-surface layers (Berrueta Razo et al. 2015). As LMIG can be emitted in short pulses, they are commonly used in static SIMS.

Compared with LMIG, carbon sources ( $\text{C}_{60}^+$ ) provide a softer sputtering, reducing the chemical damage while notoriously enhancing the secondary ion yield. Likewise, carbon sources offer a better lateral resolution and can be used over the static limit routinely achieving  $< 300 \text{ nm}$  (Tian et al. 2016; Fletcher et al. 2007). Nonetheless, the chemical damage is still a limitation and carbon deposits have been noticed (Berrueta et al. 2015).

On the other hand, one of the biggest improvements in SIMS came with the appearance of Gas Cluster Ion Beams (GCIB). They are great sources for organic analysis due to their low energy per atom. This type of source produces lower fragmentation, extending the detectable mass range to  $> 2$  kDa (Winograd 2018), and producing lower sub-surface damage than carbon sources. Nonetheless, GCIB sources have two big disadvantages; the number of atoms limits the reduction of the beam size and a lower secondary yield compared with carbon sources (Winograd et al. 2006). Within GCIB sources,  $\text{Ar}_n^+$  clusters have historically been the favorite, but  $(\text{CO}_2)_n^+$  has proved to be more stable and easier to focus (Tian et al. 2016). That is why, in many laboratories,  $\text{Ar}_n^+/\text{CO}_2$  mixtures are commonly used, and pure  $\text{CO}_2$  has become the first choice. Alternatively, new types of primary beams, adding water or oxygen flooding have proved to increase the yield of molecules that suffer matrix suppression and to boost the ionization of neutral molecules (Kikuma and Imai 2001; Rabbani et al. 2013).

#### 1.1.4.2 Secondary ion yield

When the primary ions hit the sample surface, the energy that they carry is transmitted to the atoms of contact. In a cascade reaction, this energy is spread to the surrounding atoms, producing the displacement and emission of particles from the most upper layers ( $< 1$  to a few nanometers) of the surface. Most of the sputtered particles are neutral atoms and molecules, while only about  $< 10^{-4}$  of the emitted particles are expected to get ionized (Benninghoven 1994; Popczun et al. 2017).

Yet, the secondary ion yield is not only influenced by the primary ion beam features but also by the properties of the targeted analytes and its chemical and morphological environment. The variability of the yield, according to the particular chemical environment and other characteristics of the analyzed surface, is known as the matrix effect. Since this effect causes large variations on the ionization probability, SIMS is generally considered a non-quantitative technique (Priebe et al. 2020). At the same time, SIMS is recognized as the most sensitive elemental and isotopic surface analysis technique and obtaining relative quantitation requires the use of internal standards. Alternatively, the matrix effect can be also employed to enhance the yield. As mentioned above, the addition of particular species such as oxygen or water can increase the secondary ion yield in several folds (Kikuma and Imai, 2001; Rabbani et al. 2013).

To work with biological samples, it also has to be considered that the number of molecules on the upper layers is limited, especially because not only the most abundant species are relevant, but the ones present in a very low concentration can be the target of our analysis. On top of that, the ionization probability for most of the particles is lower than  $10^{-4}$  (Benninghoven 1994) what becomes particularly relevant for high-resolution images, where the number of available molecules can get too low for being even detected. Thanks to their bigger secondary ion yield, this issue has been partially overcome by dynamic SIMS techniques (Hanrieder et al. 2013a).

To assess the secondary ion yield, we can calculate several parameters. The ionization rate, to obtain the number of emitted ions divided by the number of atoms present within the analyzed volume (Guerquin-Kern et al. 2005) or the ionization efficiency, which indicates the number of collected ions divided by the number of applied primary ions (Kollmer 2004).

#### 1.1.4.3 Transmission and Sensitivity

High transmission power is required to avoid a big gap between the number of produced and collected secondary ions. SIMS devices are therefore characterized by having high transmission efficiency and high sensitivity. Ranging their sensibility from parts per million

(ppm) to parts per billion (ppb) (Guerquin-Kern et al. 2005) and a transmission efficiency that reaches > 90 % (Kita et al. 2009).

#### 1.1.4.4 Spatial resolution

Due to its destructive nature, in SIMS two types of spatial resolution are considered, lateral and depth resolution. The lateral resolution for SIMS instruments (X and Y axis) ranges from microns to hundreds of nanometers when employing Time of Flight Secondary Ion Mass Spectrometry (ToF-SIMS) to tens of nanometers for Nanoscale Secondary Ion Mass Spectrometry (NanoSIMS) (< 40 nm) (Massonnet and Heeren 2019; Nuñez et al. 2018). Despite the lateral resolution is mainly determined by the diameter of the primary beam, as mentioned above, when analyzing organic samples the limit of the spatial resolution is also determined for the availability of molecules and their probability of ionization. That is why the concept of useful lateral resolution, the minimum square area required to detect a certain analytes, may be more appropriate to work with biological samples (Hanrieder et al. 2013b; Kollmer et al. 2013; Fletcher and Vickerman 2010). To optimize the lateral resolution, it is crucial to reduce the beam size but also to increase the sensitivity and transmission of the instruments.

Secondly, the so-called depth resolution measures how well the interface between two adjacent layers can be resolved (Magee et al. 1982). For most SIMS instruments, depth resolution ranges from 1 to a few nanometers. However, this is rapidly improving and some optimized instruments are able now to reach atomic depth resolution (Michalowski et al. 2019).

In SIMS, both spatial resolution are commonly calculated based on the drop of signal from 84 % to 16 % of its maximum intensity (Saka et al. 2014).

#### 1.1.4.5 Mass resolution

In mass spectrometry, the mass resolution power (MRP) is the ability to resolve the difference between two peaks with a similar mass to charge ratio (e. g.  $^{13}\text{C}^{14}\text{N}^-$ , 27.0064 a.m.u., from  $^{12}\text{C}^{15}\text{N}^-$ , 27.0001 a.m.u.). The required MRP is calculated by dividing the nominal mass ( $M$ ) by the exact difference ( $\Delta M$ ) of the two species (Gorman and Kraft 2020).

$$MRP = M/\Delta M$$

#### 1.1.4.6 Mass dispersion

This parameter describes for SIMS instruments the heaviest and lightest secondary ions that can be collected simultaneously (Gorman and Kraft 2020).

$$\text{Mass dispersion} = M_{\max}/M_{\min}$$

#### 1.1.5 SIMS polarities

Depending on the secondary ions that we want to analyze, positive or negatives, we have to set the polarity of the instrument. Primary ion sources such as  $\text{Cs}^+$  will enhance the emission of negative secondary ions while sources such as  $\text{O}^-$  will increase the production of positive secondary ions (Figure 2) (Nuñez et al. 2018).



<p> <span style="color: green;">■</span> Secondary ion yield enhanced with O<sup>-</sup>  <span style="color: yellow;">■</span> Secondary ion yield enhanced with Cs<sup>+</sup> </p>																		HELIUM 2 He 4.0026					
LITHIUM 3 Li 6.941		BERYLLIUM 4 Be 9.0122																BORON 5 B 10.811	CARBON 6 C 12.011	NITROGEN 7 N 14.007	OXYGEN 8 O 15.999	FLUORINE 9 F 18.998	NEON 10 Ne 20.180
SODIUM 11 Na 22.990		MAGNESIUM 12 Mg 24.305																ALUMINIUM 13 Al 26.982	SILICON 14 Si 28.086	PHOSPHORUS 15 P 30.974	SULFUR 16 S 32.065	CHLORINE 17 Cl 35.453	ARGON 18 Ar 39.948
POTASSIUM 19 K 39.098	CALCIUM 20 Ca 40.078	SCANDIUM 21 Sc 44.956	TITANIUM 22 Ti 47.867	VANADIUM 23 V 50.942	CHROMIUM 24 Cr 51.996	MANGANESE 25 Mn 54.938	IRON 26 Fe 55.845	COPPER 27 Cu 63.546	NICKEL 28 Ni 58.693	COPPER 29 Cu 63.546	ZINC 30 Zn 65.38	GALLIUM 31 Ga 69.723	GERMANIUM 32 Ge 72.64	ARSENIC 33 As 74.922	SELENIUM 34 Se 78.96	BROMINE 35 Br 79.904	KRYPTON 36 Kr 83.798						
RUBIDIUM 37 Rb 85.468	STRONTIUM 38 Sr 87.62	YTIUM 39 Y 88.906	ZIRCONIUM 40 Zr 91.224	NIOBIUM 41 Nb 92.906	MOLYBDENUM 42 Mo 95.96	TECHNETIUM 43 Tc [98]	RUTHENIUM 44 Ru 101.07	RHODIUM 45 Rh 102.91	PALLADIUM 46 Pd 106.42	SILVER 47 Ag 107.87	CADMIUM 48 Cd 112.41	INDIUM 49 In 114.82	TIN 50 Sn 118.71	ANTIMONY 51 Sb 121.76	TELURIUM 52 Te 127.6	IODINE 53 I 126.90	XENON 54 Xe 131.29						
CAESIUM 55 Cs 132.91	BARIUM 56 Ba 137.33	LANTHANUM 57 La 138.91	HAFNIUM 72 Hf 178.49	TANTALUM 73 Ta 180.95	TUNGSTEN 74 W 183.84	RHENIUM 75 Re 186.21	OSMIUM 76 Os 190.23	IRIDIUM 77 Ir 192.22	PLATINUM 78 Pt 195.08	GOLD 79 Au 196.97	MERCURY 80 Hg 200.59	THALLIUM 81 Tl 204.38	LEAD 82 Pb 207.2	BISMUTH 83 Bi 208.98	POLONIUM 84 Po [209]	ASTATINE 85 At [210]	RADON 86 Rn [222]						
FRANCIUM 87 Fr [223]	RADIUM 88 Ra [226]	ACTINIUM 89 Ac [227]	RUTHERFORDIUM 104 Rf [261]	DUBNIUM 105 Db [262]	SEABORGIUM 106 Sg [266]	BOHRIUM 107 Bh [264]	HASSIUM 108 Hs [277]	MITHENIUM 109 Mt [268]	DARMSTADTIUM 110 Ds [271]	ROENTGENIUM 111 Rg [272]													

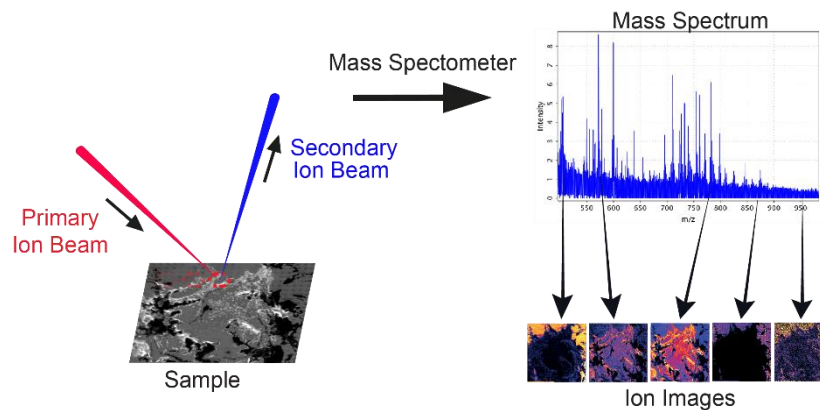
  

CELIUM 58 Ce 140.12	PRASEODYMIUM 59 Pr 140.91	NEODYMIUM 60 Nd 144.24	PROMETHIUM 61 Pm [145]	SAMARIUM 62 Sm 150.36	EUROPIUM 63 Eu 151.96	GADOLINIUM 64 Gd 157.25	TERBIUM 65 Tb 158.93	DYSPROSIUM 66 Dy 162.50	HOLMIUM 67 Ho 164.93	ERBIUM 68 Er 167.26	THULIUM 69 Tm 168.93	YTERBIUM 70 Yb 173.05	LUTETIUM 71 Lu 174.97
THORIUM 90 Th 232.04	PROTACTINIUM 91 Pa 231.04	URANIUM 92 U 238.03	NEPTUNIUM 93 Np [237]	PLUTONIUM 94 Pu [244]	AMERICIUM 95 Am [243]	CURIUM 96 Cm [247]	BERKELIUM 97 Bk [247]	CALIFORNIUM 98 Cf [251]	EINSTEINIUM 99 Es [252]	FERMIUM 100 Fm [257]	MENDELEVIUM 101 Md [258]	NOBELIUM 102 No [259]	LAWRENCIUM 103 Lr [262]

**Figure 2. Periodic table showing the best polarity to enhance the yield of each element.** In Green, elements that have more tendency to form positive secondary ions using a negative primary ion source such as O<sup>-</sup>, in yellow, the elements with a higher tendency to form negative secondary ions using a positive primary ion source such as Cs<sup>+</sup>.

### 1.1.6 Imaging mass spectrometry

Imaging mass spectrometry techniques (IMS) combine the ability to unravel the chemical composition of solid surfaces with the ability to reconstruct the distribution and abundance of the different ion species in 2- or 3-dimensions images. Regarding IMS, there is always a competition between the achievable spatial resolution (lateral and depth), the mass resolution power and the challenge to obtain images within a compatible working time. Different modes and primary sources are chosen according to the features that want to be optimized. To generate such chemical maps, the primary ion beam sequentially scans the surface of the sample collecting the entire mass spectrum from each pixel (Agüi-Gonzalez et al. 2019; Pacholski and Winograd 1999). Later, chemical map images are formed recalling the distribution and abundance of the different ion species (**Figure 3**).



**Figure 3. Imaging mass spectrometry.** The surface of a solid sample is sequentially scanned by the primary ion beam of the SIMS instrument. Together with the coordinates, the secondary ions detected on each individual pixel are collected to later reconstruct images that reproduce the distribution and abundance of the different ion species.

Later, the signal intensity for a particular  $m/z$  value at every acquisition coordinate is included to reconstruct a 2-dimensional ion density map, or image for each of the mass signals detected throughout the section (Figure 4).

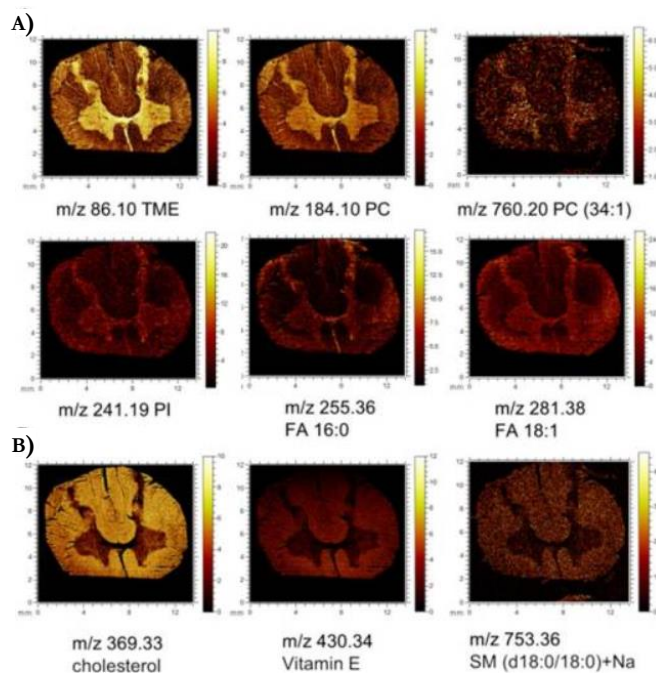


**Figure 4. 2D imaging with ToF-SIMS.** Single ion images of individual molecular species that localize to distinct anatomical regions of the spinal cord. **A)** Lipid species that localize predominantly in the gray matter. In the upper row, phospholipids detected in positive mode including trimethylethylenimine ( $m/z$  86.1), phosphatidylcholine headgroup ( $m/z$  184.09), phosphatidylcholine 34:1 ( $m/z$  760.20). In the lower row of panel (A), ions detected in negative mode like phosphoinositol headgroup ( $m/z$  241.19) as well as fatty acids (FA) such as palmitic acid (FA 16:0,  $m/z$  255.36) and oleic acid (FA 18:1,  $m/z$  281.38). **B)** Chemical species that localize within the white matter including cholesterol ( $m/z$  369.33), vitamin E ( $m/z$  430.34), and sphingolipids such as sphingomyelin (SM(d36:0)+Na<sup>+</sup>,  $m/z$  753.36). Figure adapted from Hanrieder et al. (2013b), courtesy of the American Chemical Society.

Yet, SIMS is also able to reconstruct 3D images, displaying the abundance and distribution of different ion species across subsequent layers of the sample. The depth resolution of those images varies across instruments and primary ion sources but it is commonly below 10 nm (Figure 5).

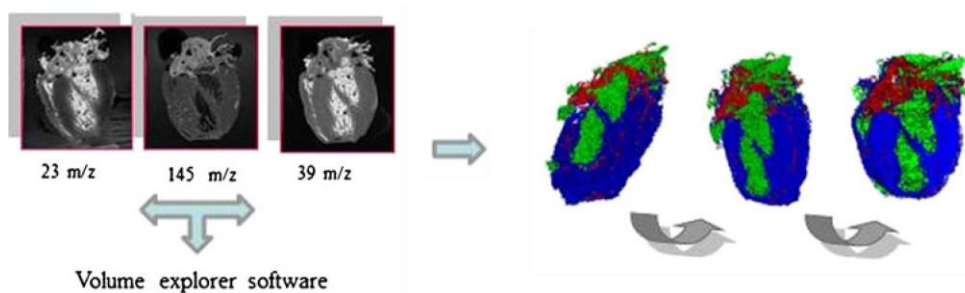


**Figure 5. 3D mass spectrometry imaging.** Reconstruction of the heart showing 3D-spatial distributions of three different ions 23  $m/z$  (green), 145  $m/z$  (red), and 39  $m/z$  (blue) with the co-registration of 40 individual MS images. Figure adapted from Fornai et al. (2012), courtesy of the American Chemical Society.

### 1.1.7 Sample preparation

Due to its nature, all SIMS techniques require working under high vacuum levels ( $< 10^{-4}$ Pa). These pressure levels minimize the collisions of secondary ions with atmospheric gasses, as

well as preventing the contamination of the sample surface by deposition of background gas particles (Neikov and Yefimov 2019). Sample preparation, which includes water removal and fixation, must enable the analysis of biological samples under these vacuum levels while preserving as much as possible their native states, maintaining the original composition and distribution of their biomolecules. There are numerous methods to process biological samples in IMS, being the most widely used: physical fixation methods (such as frozen-hydrated and freeze-drying), chemical fixation, and resin embedding.

For both physical fixation methods, frozen-hydrated and freeze-drying, once the experimental part has concluded, the samples are submerged in liquid propane (85 K). Plunged freezing reduces the ice crystal formation, which can perturb on a big scale the original arrangement of the surface molecules. The samples are subsequently transferred and can be stored in liquid nitrogen (77 K) until they are analyzed (Passarelli and Winograd 2011; Agüi-Gonzalez et al. 2019).

The frozen-hydrated method has demonstrated to preserve better the morphology and natural distribution of biomolecules. It maintains the samples hydrated and it keeps the material distribution as closely as possible to *in vivo* conditions. Thus, it represents the gold standard for cellular studies (Yoon and Lee 2018; Cunha, da et al. 2016). However, to work with frozen-hydrated samples, the instrument must be previously cooled, both loading and analysis chambers and, to avoid thawing and ice crystal formation, the temperature needs to remain stable during the whole process (Fletcher et al. 2008b). Apart from the fact that not all SIMS instruments can be cooled, the high risk of ice condensation and the difficulty of keeping the temperature within this narrow range during the entire process (transference and analysis), makes it a challenging a less reproducible choice.

On the other hand, freeze-drying represents the simplest method to preserve biological samples for SIMS. After snap freezing and storage in liquid nitrogen, samples are transferred into a vacuum dryer ( $\sim 10^{-5}$  Torr) where the water is removed by sublimation before any melting occurs (Kurczy et al. 2008). Subsequently, the dehydrated samples can be handled at room temperature (RT) for analysis. The main issue of this sample preparation is that due to the loss of water during the drying phase, changes in the cellular membrane structure are prompt to occur and there are some doubts about the use of freeze-drying for sub-cellular analysis (Nygren et al. 2006).

Chemical fixation methods are the gold standard for other imaging techniques, (e. g. glutaraldehyde for protein fixation or osmium tetroxide for lipids) but for SIMS, the addition of chemical fixatives can interfere with the later analysis. However, for some SIMS studies, where the targets are only particular molecules, this may not be an issue.

Embedded samples are a great alternative for SIMS experiments when the chemical information is not required (e. g. NanoSIMS experiments) and the target biomolecules are not removed during the process, however this sample preparation method may preclude the analysis of some biomolecules such as lipids. Once the samples are fixed with other methods, such as glutaraldehyde for protein crosslinking, resin embedding enables to slice the samples, to analyze concrete parts of the samples (a concrete depth in a tissue or inner parts of the cells). This removes the artifacts due to the topography and protects the morphological preservation of the sample. On the other hand, when the samples are embedded, the introduced material can dilute the signals of interest, for example, since resins contain a significant amount of carbon it will affect the measured  $^{12}\text{C}$  and  $^{13}\text{C}$ . Likewise, the residual presence of salts and other compounds can interfere with the ionization of the analytes (Nuñez et al. 2018; Rogge et al. 2018).

Independently of the sample preparation method, for SIMS analysis, the samples must be placed on a conductive surface such as indium tin oxide (ITO) coated glass, silicon wafers,

or transmission electron microscopy (TEM) grids. If the samples are therefore placed on conductive surfaces and their thickness and characteristics allow an appropriate current flow, the samples can be analyzed with SIMS. On the contrary, if the current does not flow properly, because we are working with insulating samples, charging effects will appear, decreasing or even eliminating the secondary ion signal. Often, a conductive layer (such as Au, Pd, Ir, or C) is deposited over the sample surface to increase its conductance and an electron gun is included in many instruments to compensate for charging effects (Gorman and Kraft 2020; Nuñez et al. 2018).

### 1.1.8 Specific targets in biological samples

One of the main advantages of SIMS is that it can work without adding exogenous labels. However, to address specific biological questions, rare stable-isotopes and other types of markers are widely used.

Isotopes are variants of a particular chemical element that contain the same number of protons but a different number of neutrons. For example, carbon 12 ( $^{12}\text{C}$ ) is the most abundant of the carbon isotopes, contributing to  $\sim 98.9\%$  of the total amount of carbon in nature. Its nucleus is composed of 6 protons and 6 neutrons, while carbon 13 ( $^{13}\text{C}$ ) contains 6 protons and 7 neutrons and represents only about  $1.1\%$  of the total. Because neutrons have no charge, isotopes do not present different chemical properties, but only different atomic weights, and it is exactly the difference in their mass to charge ratio what SIMS uses to distinguish and sort them. Isotopes can be included in the synthesis of any type of biomolecules, enabling their tracing within tissues or cellular compartments. This is a common strategy in SIMS for the study of metabolic processes regarding all types of biological macromolecules (proteins, lipids, carbohydrates, etc.) (Jähne et al. 2021; Kraft 2017; Passarelli et al. 2017).

Nonetheless, the relative abundance of isotopes for a particular element is not universal and slight variations are present among different materials and samples. That is the reason why we should always include an internal control in our sample set. These controls are samples produced following the same protocols that do not contain exogenous amounts of the isotope or element of interest. This will set the threshold for its specific natural abundance, allowing later a more accurate quantification of the relative enrichment (Boxer et al. 2009; Kraft 2017).

Besides using biomolecule homologous that carry rare-stable-isotopes, SIMS can also explore the kinetics of other chemical substances, for example, tracing the specific absorption of drugs according to the cell type or subcellular compartment (Jiang et al. 2017; Tian et al. 2017). Moreover, diverse types of probes have been recently developed to label particular biological targets such as specific proteins of interest (POIs). These and other labeling methods for SIMS will be further discussed in Aim II.

### 1.1.9 Mass analyzer types

According to the way of sorting secondary ions, there are four main types of mass analyzers: quadrupole, ion trap, time-of-flight, and sector instruments. Each type has its strengths and weaknesses directly depending on the purpose of the analysis. Quadrupole analyzers, which consist of four parallel metal rods, apply oscillating electric fields to sort the secondary ions according to the stability of their trajectories (**Figure 6**) (Chernushevich et al. 2001).

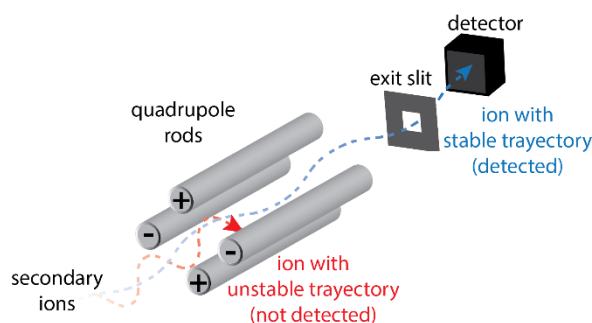


**Figure 6. Quadrupole mass spectrometer.** The rods are electrically connected to their opposite one, and a radio frequency voltage is applied between each pair. The emitted secondary ions travel between the rods and only the ions with a certain  $m/z$  ratio can reach the detector. On the contrary, ions with a different  $m/z$  ratio will present unstable trajectories, colliding with the rods and not being able to reach the detector. Either this permits the selection of a secondary ion species with a particular mass-to-charge ratio or to detect a range of  $m/z$ -values by continuously adjust the applied voltage.

Due to their mass accuracy and mass range, orbitraps and other ion trap mass analyzers are gaining recognition in biology. Orbitraps are composed of a coaxial inner spindle-like and an outer barrel-like electrode that trap ions spinning in between (**Figure 7**). The oscillations frequencies are decoded by Fourier transformations providing a very precise reading of their  $m/z$  (Scigelova and Makarov 2006).

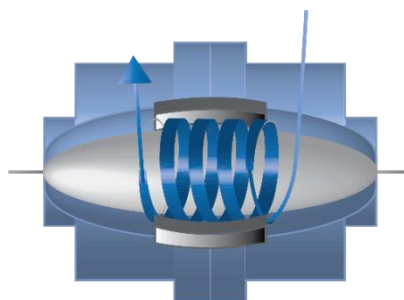


**Figure 7. Orbitrap.** Orbitraps are ion trap mass analyzers that consists of a central and an outer electrode. The injected secondary ions are trapped because their electrostatic attraction to the inner electrode is balanced by their inertia. By measuring the frequencies induced on the outer electrode by the oscillations of the ions, their mass-to-charge ratio can be calculated. Thus, the trap can act as analyzer and detector. Figure adapted from Agüi-Gonzalez et al. (2019), courtesy of the Royal Society of Chemistry.

Time of Flight (ToF) mass analyzers contain a long electric sector that accelerates all ions with an equal charge to the same kinetic energy. The velocity of their flight relies then on their mass to charge ratio, and the ionic sorting is based on the time that they take to fly from the surface of the sample to the detector plate. At equal charge, the longer the time of flight, the higher the mass of the molecule. This type of mass analyzer requires a pulsed sputtering and can record, within a range, the entire spectra of secondary ions (Massonnet and Heeren 2019). On magnetic mass analyzers, when passing through the magnetic sector, the incoming ions are deflected drawing a curve. The radius of the curve is determined by the mass to charge ratio of the ions and the detectors need to be placed specifically to collect the target masses (Nuñez et al. 2018). Within this thesis, only ToF-SIMS, which has the ToF analyzer, and NanoSIMS, which contains a magnetic sector analyzer, will be deeply addressed. Further information about these techniques can be respectively found in Aim I and Aim II.

### 1.1.9.1 ToF-SIMS

The basic principle of ToF-SIMS is that at equal charge, the heavy ions move slower than the light ones, thus, different masses will reach the detector at different times (**Figure 8**). This principle enables ToF mass analyzer to sort secondary ions by their mass to charge ratio based on the time that they take to reach the detector. To enable this, all ions must previously have the same kinetic energy level. For this, the primary beam needs to be pulsed or bunched (Fletcher et al. 2008a) and secondary ions must be accelerated by an electric field before entering into the ToF sector (Boxer et al. 2009; Agüi-Gonzalez et al. 2019).

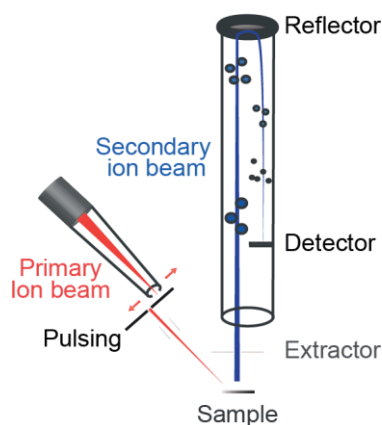


**Figure 8. Time of flight SIMS scheme.** ToF-SIMS instrument representation with a pulsed primary ion beam. The pulsed or bunched primary ion beam provides the same initial kinetic energy level to the secondary ions. Time-of-flight mass analyzers sort the secondary ions according to the time that they take to flight into the detector. Figure adapted from Agüi-Gonzalez et al. (2019), courtesy of the Royal Society of Chemistry.

ToF analyzers collect the whole spectrum at each pixel, detecting molecules from a few up to 2 kDa with a sensitivity of ppb, offering an MRP of  $> 10.000$ . According to the chosen primary source, their lateral resolution differs substantially, but sub-micrometer images are commonly achieved together with an exceptional depth resolution ( $< 10$  nm) (Fletcher 2015; Singh et al. 2020).

One of the main advantages is that ToF-SIMS admits experiments without specific targets, facilitating the discovery of biomolecules involved in particular biological processes (Agüi-Gonzalez et al. 2019). However, analyzing and interpreting these big datasets demands long working times. Moreover, since the images contain the entire mass spectrum for each pixel, a method to identify high mass peaks is required. ToF-SIMS rely on two main strategies, a very high mass resolution to ensure a reliable peak assignment or the use of MS/MS capabilities (Massonnet and Heeren 2019). MS/MS is used to break initial secondary ions into smaller fragments, identifying the original molecules thanks to the specific fragments that are produced (Fisher et al. 2016; Phan et al. 2017).

### 1.1.9.2 NanoSIMS

The NanoSIMS (Cameca, Gennevilliers Cedex, France) is a dynamic SIMS instrument (primary ion dose  $> 10^{15}$  ions/cm<sup>2</sup>) composed of an electrostatic and a magnetic sector (Kraft and Klitzing 2014). This type of mass analyzer applies a magnetic field, forcing the secondary ions to travel following a circular path. The radius of the arc differs in consonance to the  $m/z$  of the secondary ions (**Figure 9**). By scanning across the surface with the primary beam, each detector will obtain the number of counts per pixel of a concrete species with a sensitivity of parts per million (ppm) (Steinhauser and Lechene 2013).

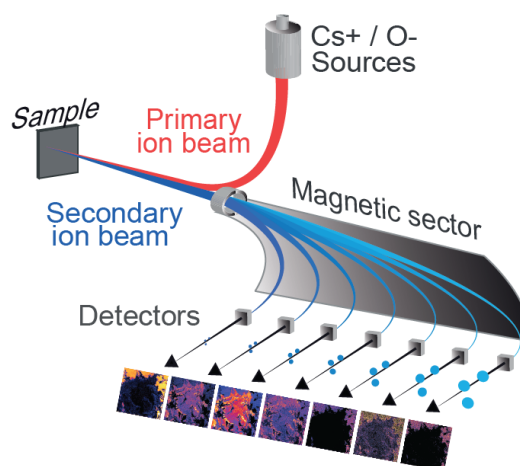


**Figure 9. NanoSIMS 50L scheme.** Instrument built with a dual source (RF-plasma  $O^-$  and  $Cs^+$ ) and coaxial configuration between the primary and secondary ion beams. NanoSIMS contains a magnetic sector, and a multi-collection system of 7 detectors. Figure adapted from Agüi-Gonzalez et al. (2019), courtesy of the Royal Society of Chemistry.

The newest version, the NanoSIMS 50L, counts with 7 detectors, reproducing the localization and the abundance of different molecular species together with a scanning electron microscopy (SEM) that appends the topographical information of the samples. The coaxial configuration of the instrument, with the primary and secondary ion beams sharing the same axis (**Figure 10**), improves the focus of the primary beam, decreasing at the same time the loss of secondary ions and aberrations (Guerquin-Kern et al. 2005; Nuñez et al. 2018). Due to its high transmission efficiency ( $\sim 80\%$ ) and sensitivity, NanoSIMS generates high lateral resolution images in a practical timeframe with an MRP of  $> 10.000$  (Nuñez et al. 2018; Gorman and Kraft 2020).

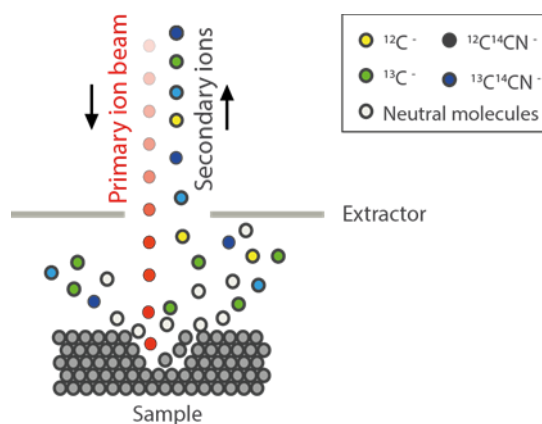


**Figure 10. Coaxial configuration.** The primary and secondary ion beams share the same axis, downsizing the focus diameter of the primary ion beam, the loss of secondary ions and aberrations.

The instrument is equipped with two sources, a cesium primary ion beam, and a radio frequency (RF) oxygen source. As previously explained, the cesium source ( $Cs^+$ ) enhances the yield of negative secondary ions (such as  $C^-$ ,  $N^-$ ,  $O^-$  or  $S^-$ ), while the oxygen source augments the yield of positive secondary ions (like  $Na^+$ ,  $K^+$ ,  $Mg^+$  or  $Ca^+$ ) (Gorman and Kraft 2020). With the incorporation of the new RF oxygen source, now both primary beams can be focused to  $< 50$  nm (Malherbe et al. 2016; Nuñez et al. 2018). However, on biological samples, a lateral resolution of  $\sim 100$  nm is more often used, since it ensures to obtain enough secondary ions from the analyzed voxels (Kraft and Klitzing 2014; Agüi-Gonzalez et al. 2019; Gorman and Kraft 2020). Due to the high energy of its primary monoatomic sources ( $Cs^+$  and  $O^-$ ), only elementary and isotopic distribution can be obtained at a nanometer scale (Nuñez et al. 2018; Gorman and Kraft 2020).

The NanoSIMS 50 mass analyzer offers a maximum mass dispersion of 13.2 (mass dispersion is equal to the highest mass divided by the lowest mass), which is for example lower than the mass dispersion required to simultaneously collect  $^{12}\text{C}^-$  and  $^{197}\text{Au}^-$  ( $\sim 16.5$ ). Together with the 2 additional detectors (7 instead of 5), the more recent NanoSIMS 50L has a larger magnet which increases the mass dispersion to 21. In addition, the magnetic field switching mode can further increase this range, offering the possibility of collecting additional masses (Gorman and Kraft 2020; Gyngard and Steinhauser 2019). Thus, this instrument is optimal for experiments that require high lateral resolution and predefined targets but do not require the preservation of intact molecules. The targets can be identified through the detection of distinguishable isotopes internally included in their molecules or by labeling them with SIMS-compatible probes (He et al. 2018; Wilson et al. 2012).

## 1.2 INTRODUCTION AIM I: STUDY OF THE PLASMA MEMBRANE LIPID DISTRIBUTION ON HIPPOCAMPAL NEURONS WITH TOF-SIMS

\*Work based on:

**Agüi-Gonzalez P**, Guobin B, Gomes de Castro MA, Rizzoli SO and Phan NTN (2021): Secondary Ion Mass Spectrometry Imaging Reveals Changes in the Lipid Structure of the Plasma Membranes of Hippocampal Neurons Following Drugs Affecting Neuronal Activity. *ACS Chem Neurosci* 12, 1542–51

---

### 1.2.1 Lipids

The term lipid includes a broad and diverse group of biomolecules, which share some common features. Lipids are all hydrophobic or amphipathic molecules that have a very limited water solubility and are easily dissolvable in organic solvents (Fahy et al. 2011). Traditionally, the cellular functions associated with lipids were restricted to create physical barriers or to constitute energy sources for cells and organisms. In fact, lipids form bilayer membranes that separate cells and organelles from their environment. Likewise, lipids constitute a crucial source of energy. Nonetheless, thanks to the emergence of new methods and further studies, lipids have been progressively related to many other biological processes and functions (Vázquez et al. 2018).

Lipids can be classified in numerous manners; one of them is to divide them into neutral or polar lipids. When the electrons shared in their bonds (carbon-carbon or carbon-hydrogen bonds) are relatively equally shared, lipids are considered neutral or non-polar (e. g. Triacylglycerols). On the contrary, the electrons in polar lipid bonds are not so equally distributed. Like in the case of oxygen-hydrogen bonds in water molecules, the electronegativity of hydrogens is considerably smaller than the one of oxygen atoms (Poltzer and Murray 2018). Thus, electrons will spend more time close to the oxygen, giving a slight negative charge to this end of the molecule, while hydrogens present a slight positive charge. Polar molecules, like phospholipids, are often amphiphilic, meaning that within the same



molecule there are hydrophobic and hydrophilic ends, showing these two regions contrasting degrees of solubility in polar and non-polar solvents (Zhang 2016). Polar lipids are normally composed of one or two hydrophobic acyl chains together with a polar headgroup. The concrete type of headgroup, its charge, size, and acyl chain compositions will have a strong effect on the physical properties of the membranes, regulating its curvature, flexibility, thickness, fluidity, permeability, etc (Wilde 2014).

Another way of classifying lipids relies on their biochemical origin. Biological lipids can be partially or completely originated from two biochemical subunits: ketoacyl or isoprene groups. According to this, lipids can be sorted into eight categories. Fatty acids (FA), glycerolipids (GL), glycerophospholipids (GP), sphingolipids (SP), saccharolipids (SL), and polyketides (PK) are built based on ketoacyl subunits, while sterols (ST) and prenols (PR) are based on isoprene subunits (**Figure 11**) (Fahy et al. 2005; 2009).

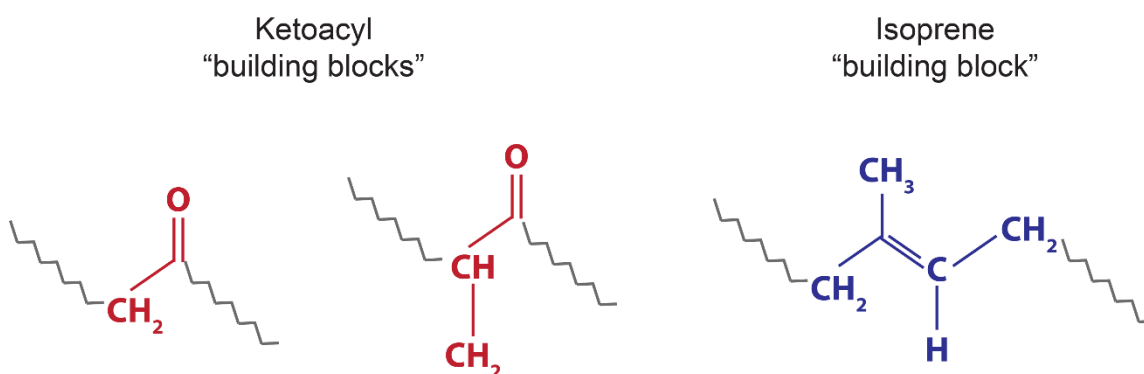


**Figure 11. Ketoacyl and isoprene subunits.** In red, the two Ketoacyl building blocks, Acetyl and Propionyl. In blue, the Isoprene building block. Molecule structures obtained with permission from Lipid Maps (Fahy et al. 2009).

### 1.2.1.1 Fatty Acids

Fatty acids (FA) are essential structural components of the cellular membranes, also playing important roles in energy storage and signal cascades. FA are hydrocarbons that contain a terminal carboxyl group (R-COOH) together with an aliphatic chain (**Figure 12**). The carboxylic acid group represents the hydrophilic part of these molecules, while the hydrocarbon chain is hydrophobic. Thus, the water solubility of these molecules is reduced in concordance to the length of their acyl chains. FA are termed saturated, if all the carbons in their structure are linked by single bonds, or unsaturated if one (monounsaturated) or several carbon-carbon (polyunsaturated) double bonds are present (Beare-Rogers et al. 2001). The presence of single or double bonds implies structural differences, affecting also the way that FAs cluster and conferring different physical properties to the membranes that they constitute (Hashimoto and Hossain 2018).

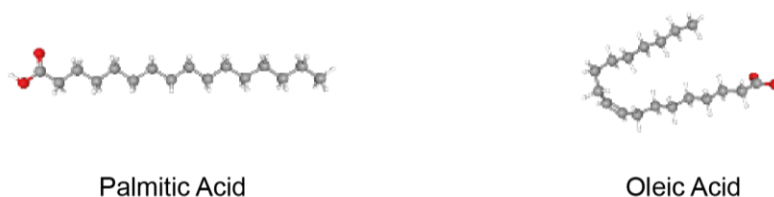


**Figure 12. Examples of saturated and unsaturated fatty acids.** Saturated fatty acids (like palmitic acid) present a linear structure while unsaturated fatty acids (such as oleic acid) bend due to the presence of double bonds. Molecular structure extracted from PubChem (Kim.S et al. 2021), courtesy of the National Center for Biotechnology Information.

### 1.2.1.2 Glycerolipids

Glycerolipids (GLs) are a large and heterogeneous group of amphipathic lipids that play key roles in membrane formation, energy storage, and intracellular signaling. All GLs contain at least a hydrophobic acyl or alkyl chain bond by an ester or ether link to a glycerol backbone (**Figure 13**) (Voelker 2013). GLs connect with other lipids and proteins with non-covalent interactions that are essential for membrane dynamics and are also related to the formation of microdomains and phase separations. Within this group, neutral glycerolipids like mono-, di- and triacylglycerols (TG) are included. TGs contain three fatty acids linked by an ester bond to a glycerol backbone, and constitute the main form of fat storage in eukaryotes. With the hydrolysis of their ester bonds, TGs provide precursors (fatty acids and diacylglycerols) for membrane synthesis. The formation of TGs also reduces fat excess from cells, diminishing lipotoxicity. GLs are involved in many metabolic pathways, serving both as precursors and direct secondary messengers (Bittman 2013).

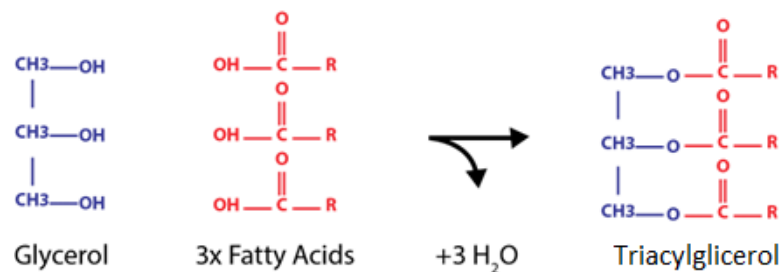


**Figure 13. Triacylglycerols formation.** To constitute a triacylglycerol molecule, three fatty acids are linked to a glycerol moiety by ester linkages.

### 1.2.1.3 Glycerophospholipids

Glycerophospholipids (GPs), commonly known as phospholipids, compose the major structural lipids class in eukaryotic membranes (cellular plasma membrane, Golgi, endoplasmic reticulum, endosomes, and mitochondria). The differences among the > 1000 types of phospholipids are based on the different acyl chains attached to sn-1 and sn-2 of the glycerol backbone, as well as the specific headgroup linked to sn-3 (**Figure 14**) (El-Bacha and Torres 2016). The headgroup conforms the polar end, which is charged by the ionization of the phosphate group and the nitrogenous base. GPs play a broad range of roles in human bodies, but they have special relevance on brain functions, conforming ~ 20-25 % of the brain dry weight in adults (Tracey et al. 2018). Among others, neural membrane GPs have been described as second messenger reservoirs, showing that they are also involved in transport mechanisms, enzymatic bounding, direct lipid second messengers, and apoptotic processes. The abundance and distribution of different GP types vary across the neural membranes. This distribution influence the physical properties of the membranes and their balance has been associated with neurological and neurodegenerative disorders (Farooqui et al. 2000).

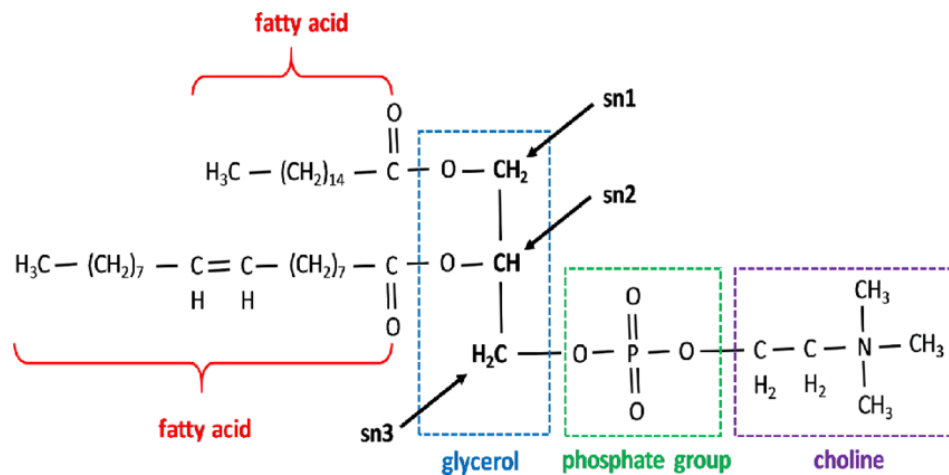


**Figure 14. Scheme of GPs structure.** GPs are subdivided into several subclasses based on the headgroup that is linked to the glycerol backbone on position sn-3. Figure extracted from MacDonald et al. (2019), courtesy of Scientific Research.

**Phosphatidic acid (PA):** PAs are formed through the acetylation of glycerol-3-phosphate (Figure 15), serving as the basic precursor for the synthesis of all the other phospholipid subclasses. In neurotransmission studies, PAs have been directly related to membrane fusion and with the modifications of protein location and activity (Raben and Barber 2017).

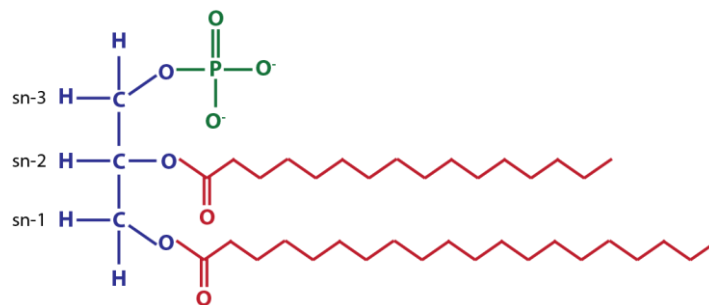


**Figure 15. Representative phosphatidic acid structure.** PAs contain two FAs (shown in red) and a phosphate group (green) linked to a glycerol moiety (blue). The glycerol positions (sn-1, 2, and 3) are respectively indicated.

**Phosphatidylcholine (PC):** PCs are the most abundant phospholipid subclass in all mammalian cells and are essential to preserve the membrane integrity. PCs are constituted of two FAs and a phosphorylcholine linked to the glycerol moiety (Figure 16) (Kanno et al. 2007). PCs are synthesized not only from the addition of the choline headgroup to the diacylglycerol (DAG) but also from the conversion of phosphatidylethanolamine (PE). PCs, which are mainly present on the outer leaflet, are defined as a membrane-mediated cell signal player as well as being involved in the activation of numerous enzymes (Tracey et al. 2018).

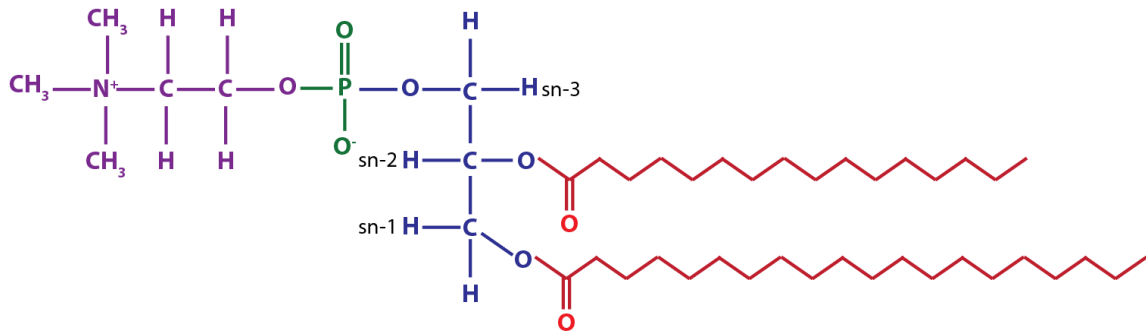


**Figure 16. 2D structure of a phosphatidylcholine molecule.** PCs are constituted for two FAs (displayed in red), a choline (purple) and a phosphate group (green) linked to the glycerol moiety (blue). The glycerol positions (sn-1, 2, and 3) are respectively indicated.

**Phosphatidylethanolamine (PE):** In combination with PCs, PEs constitute the major constituents of the cellular membranes. However, PEs present a clear asymmetric distribution in the plasma membrane, being > 80 % on the inner leaflet (Vance 2008). The conical shape of PEs facilitates membrane fusion and among other functions, PEs have been related to blood clotting and the synthesis of the endocannabinoid neurotransmitter anandamide.

**Phosphatidylserine (PS):** PSs are produced when the head groups of phosphatidylcholines or phosphatidylethanolamines are replaced by serine. PSs are the most abundant negatively charged phospholipids, and in healthy cells, PSs are almost totally found on the inner leaflets of plasma membranes. The alteration of PS asymmetry may be an early indicator of apoptosis serving also as a signal for phagocytosis and blood coagulation (Leventis and Grinstein 2010; Martínez-Gardeazabal et al. 2017; Vance 2008).

**Phosphatidylglycerol (PG):** regardless of the high PGs concentration in the lungs, this lipid subclass has a low presence in most tissues. They do not play a major role in eukaryotic plasma membranes, but on the contrary, they are quite abundant in mitochondria. There, cardiolipin, a metabolite of PGs, constitutes more than 15 % of all lipids, and it seems to be involved in the maintenance of the membrane potential and supports proteins for mitochondrial respiration (Tracey et al. 2018).

**Phosphatidylinositol (PI):** Despite the low abundance of this lipid subclass in cellular plasma membranes, these negatively charged lipids, mostly present on the cytoplasmic leaflet of neurons and glial cells, are considered a key element for vesicular activity and cell signaling (Piomelli et al. 2007). Some of the most relevant examples, PI(4,5)P<sub>2</sub> and PI(3,4,5)P<sub>3</sub>, can act as signals for cellular growth, proliferation, and mobility. Particularly in neurons, they are also linked to the regulation of plasma membrane events such as neurotransmitter release, neuronal excitability, and synaptic plasticity. Furthermore, numerous studies have shown that more than 100 ion channels and transporters are directly regulated by these lipids (Dickson 2019).

#### 1.2.1.4 Sphingolipids

Ceramides constitute the simplest form of sphingolipids (SPs). These molecules are formed by the linkage of a FA to a sphingosine backbone and different groups can be added to ceramides, to form more complex molecules (**Figure 17**). For example, glycosphingolipids, also referred as cerebroside, append a single sugar residue to a ceramide. While galactose is the sugar typically attached in the brain, glucose is more common in other tissues. Interestingly, SPs have been largely described as signaling lipids for apoptosis while some of their metabolic products have been related to cell growth and proliferation (Rosen and Goetzl 2005).

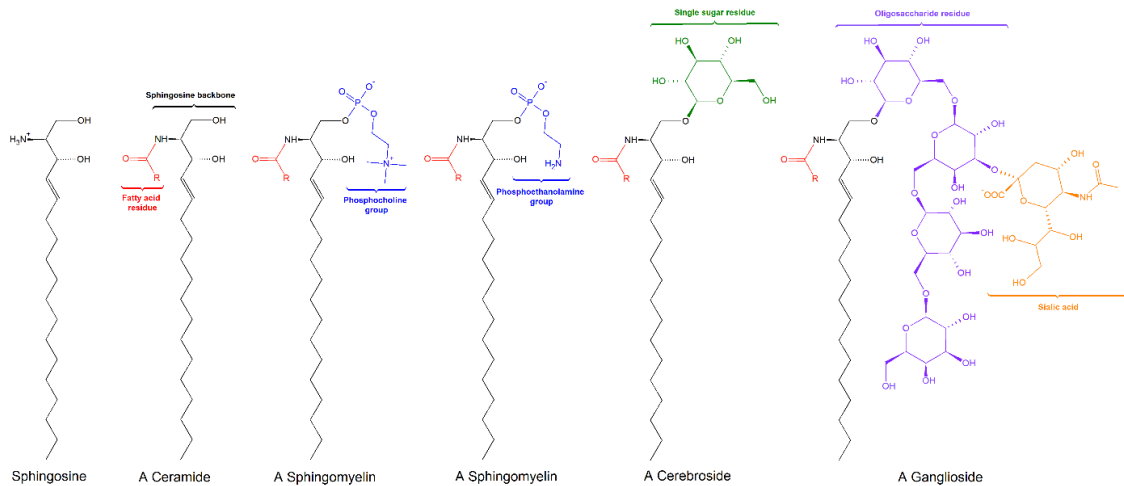


**Figure 17. General sphingolipid structures.** Sphingolipids are based on a sphingoid backbone, which contains several aliphatic amino alcohols that includes sphingosine. The sphingosine is usually bond to a charged head group such as choline, ethanolamine or serine. Figure extracted with permission from Wikimedia Commons.

### 1.2.1.5 Sterol lipids

Among many other types, cholesterol represents the main form of sterols (STs) in mammalian cells, having particular importance in the brain (Tracey et al. 2018). Cholesterol molecules present a steroid ring as its hydrophobic part while having a hydroxyl group as a polar end, and a small hydrocarbon tail (**Figure 18**).

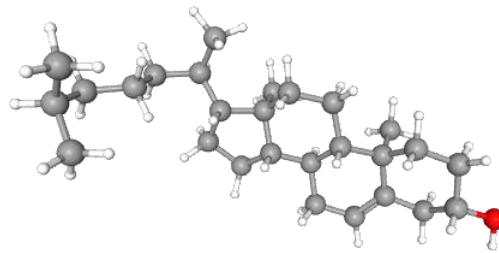


**Figure 18. 3D structure of a cholesterol molecule.** Molecular structure extracted from PubChem (Kim.S et al. 2021), courtesy of the National Center for Biotechnology Information.

### 1.2.1.6 Prenol Lipids

Prenol lipids (PR) include lipids such as carotenoids, isoprenoid precursors, and Vitamins. As an example of their relation with physiological brain function, deficiencies in vitamin E are related to peripheral neuropathy and ataxia, and this vitamin is also involved in the balance of inflammatory and anti-inflammatory levels in the brain (Stephenson et al. 2017).

### 1.2.1.7 Saccharolipids

Instead of having a glycerol moiety, saccharolipids (SL) contain fatty acids directly linked to a sugar backbone (**Figure 19**). The most known SLs are precursors related to the toxicity of gram-negative bacteria (Fahy et al. 2005).

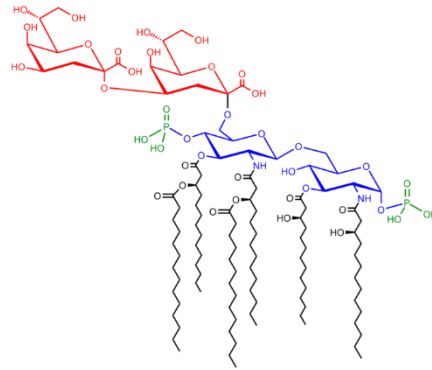


**Figure 19. Structure of Kdo2-Lipid A.** Glucosamine residues in blue, Kdo residues in red, acyl chains in black and phosphate groups in green. Molecule structure extracted with permission from Wikimedia Commons.

### 1.2.1.8 Polyketides

Polyketides (PKs) are lipid compounds that contain alternating carbonyl and methylene groups (**Figure 20**) (*IUPAC Compendium of Chemical Terminology* 2009). This diverse group of compounds is synthesized in bacteria, fungi, plants, and some marine animals (Staunton and Weissman 2001).

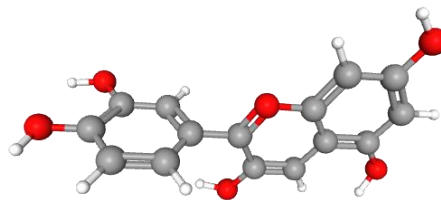


**Figure 20. Examples of a polyketide structure.** 3D structure of a Cyanidin molecule. Molecular structure extracted from PubChem (Kim.S et al. 2021), courtesy of the National Center for Biotechnology Information.

## 1.2.2 Lipid composition and physical properties of cellular membranes

Cellular membranes are assembled by spontaneous self-arrangement of the hydrophilic and the hydrophobic ends of the phospholipids. The polar ends face towards the watery environment, inside and outside of the cell, while the hydrophobic tails hide between the polar head rows (**Figure 21**). The hydrophobic character of the tails turns lipid bilayers into a non-permeable membrane for water-soluble molecules such as ions and other types of biomolecules.

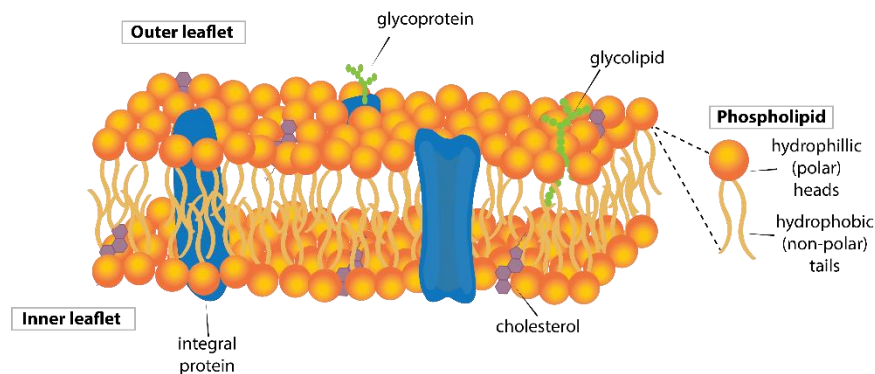


**Figure 21. Schematic representation of a eukaryotic plasma membrane.** The cellular plasma membrane is mainly composed of phospholipids. The amphipathicity of phospholipids induces the spontaneous formation of bilayers in an aqueous environment. The hydrophobic tails of the phospholipids, which contain two fatty acid chains, avoid water contact facing the inner parts of the lipid bilayer. On the contrary, the hydrophilic head of the phospholipids faces the aqueous environment both inside and outside of the cell.

Among many other functions, cellular membrane lipids build a physicochemical barrier separating the conditions inside and outside of the cell and organelles. According to the conditions and requirement, the exact functions, as well as the chemical composition of the lipid bilayer, can vary (Harayama and Riezman 2018). Following this principle, the inner and outer monolayers of the cellular plasma membranes are also remarkably different. As previously mentioned, the outer leaflet is richer in SM, PC, and cholesterol, whereas the inner monolayer is enriched with PS, PI, and PE (Mouritsen 2005). This arrangement can be modified under certain circumstances, for example, the increase of intracellular calcium during apoptosis can stimulate scramblases and inhibit translocases, reshaping the presence of particular lipids on the outer membrane leaflet. This is recognized by phagocytes, which promote the elimination of apoptotic neural cells during development phases or inflammation processes (Piomelli et al. 2007).

Multiple physical properties of the cellular membranes are linked to particular lipid compositions (**Figure 22**). For example, fluidity can be promoted by lipids with short and unsaturated FAs and double bonds, and the bending that they cause, diminish the packing level of the membrane, reducing its density. The thickness of the membrane is also related to the length of the acyl-chains as well as the presence of sterols (Holthuis and Menon 2014).

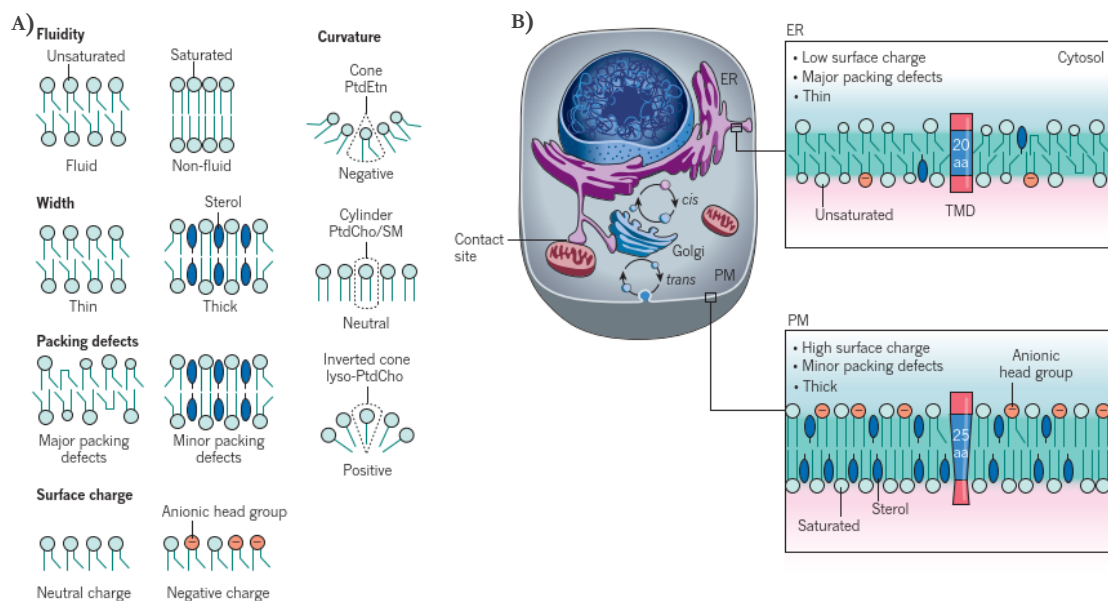


**Figure 22. Membrane lipid composition and physical properties.** **A)** Physical properties influenced by lipid composition. **B)** Main differences between endoplasmic reticulum (ER) membrane and cellular plasma membrane (PM). Figure extracted from Holthuis and Menon (2014), courtesy of Nature.

Likewise, the curvature of the membranes is directly influenced by lipids shape. Concerning the size of their acyl chain area, lipids with small polar heads (such as PEs, PAs or DAG) present a conical shape, promoting the spontaneous formation of negative curvatures (**Figure 23**). Lipids, in which the area of their hydrophobic tail and the area of their polar head are similar (e.g. PCs or SM), present a cylindrical shape and do not favor any curvature. On the contrary, lipids with a bulkier head than the tails (such as PI or lysophospholipids) will induce a positive curvature. These geometries are crucial to address processes like synaptic vesicle exocytosis (Piomelli et al. 2007).

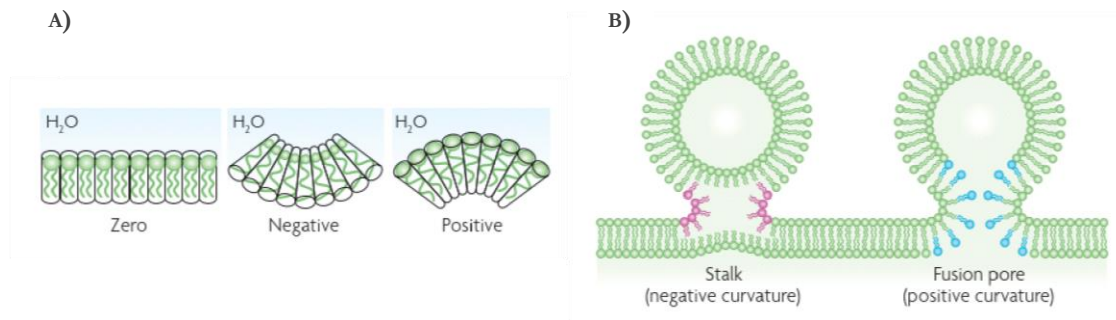


**Figure 23. Lipid geometry influences membrane curvature. A)** Cylindrical lipids do not induce curvature of the membranes, while conical lipids facilitate negative curvatures and inverted lipids a positive bending. **B)** Scheme of membrane fusion. On the left side, the negative curvature of the membrane (due to the presence of inverted cone-shaped lipids) facilitates the fusion of both outer layers of the adjacent membranes. On the right, the positive curvature produced by cone-shaped lipids enables the fusion pore formation. Figure adapted from Piomelli et al. (2007), courtesy of Nature.

Cholesterol plays a major role in biological membranes, adjusting its fluidity, thickness, compressibility, permeability, and curvature (Yang et al. 2016). Its small polar head causes close interactions with the phospholipids (especially with PCs, PSs and Pes), making cholesterol-rich regions more ordered and packed but remaining still fluid. At the same time, due to its small head, cholesterol induces spontaneous negative curvature of the membrane. In summary, the presence of cholesterol increases the compaction of the membrane, decreases its permeability (Tracey et al. 2018), and dramatically affects membrane fusion and fission (Yang et al. 2016).

### 1.2.3 Lipids in the nervous system

Traditionally, lipids were considered to play a passive role in brain functions and neuronal activity. However, numerous studies have proved that, among other functions, lipids can act as secondary messengers, modulators of ion channels, and are directly involved in neurotransmission processes (Piomelli et al. 2007).

First messengers are extracellular signaling molecules, such as hormones, growth factors, or neurotransmitters, which trigger the release of intracellular molecules as a response. These intracellular signals, known as second messengers, can induce processes like cellular proliferation, differentiation, migration, or depolarization. One of the most known processes involving lipids as second messengers is the cleavage of phosphatidylinositol bisphosphate (PIP<sub>2</sub>) by the phospholipase C in two molecules, inositol triphosphate (IP<sub>3</sub>) and DAG. The polar part, IP<sub>3</sub>, triggers the intracellular release of calcium that in combination with the DAG activates the enzyme protein kinase C (PKC), leading to the regulation of other proteins (Piomelli et al. 2007). In addition, the modulation of ion channels by the surrounding lipids has been widely discussed. Despite there is a huge heterogeneity in the structure of ion channels, all of them count with a transmembrane domain, which moves within the lipid bilayer adopting diverse conformations and status. Several hypothesis have been proposed to clarify how lipids modulate ion channels, but one of the most inquired theories is that the presence of charged lipids, can directly modulate voltage-gated channel activation (Kasimova et al. 2014; Poveda et al. 2014).

Furthermore, lipids have been strongly related to numerous neurodegenerative diseases such as Parkinson's disease (PD), Alzheimer's disease (AD), multiple sclerosis and other psychiatric conditions like as schizophrenia or bipolar disorder.



AD, the most common form of dementia, is characterized by the overproduction of the Amyloid- $\beta$  protein. The two subunits of this protein, A $\beta$ 40, and A $\beta$ 42, have been linked to the modulation of enzymes that regulate lipid production. A $\beta$ 40 inhibits an enzyme involved in cholesterol and lipids synthesis, while the second subunit enhances the ceramides production. These alterations in physiological lipid production have been linked with an acceleration of the neurodegenerative process (Shamim et al. 2018). Likewise, the local increment of certain lipids like cholesterol may increase the aggregation of Amyloid- $\beta$  (Ehehalt et al. 2003). In addition, a misbalance on lipid homeostasis has been proposed to be responsible for cellular damage in PD. A lipid droplet accumulation together with a rise in the TAG and cholesteryl ester (an ester of cholesterol) has been observed in the cells that overexpress  $\alpha$ -synuclein (a predominantly presynaptic protein linked to PD). Surprisingly they also observed that PLs were diminished in cells overexpressing  $\alpha$ -synuclein (Alza et al. 2021). Besides, in multiple sclerosis, an inflammatory autoimmune disease in which the immune system attacks the myelin sheaths in the central nervous system, the lipid metabolism may have direct and indirect effects on its progression. The lipids are suggested to be crucial on the regulation of the inflammatory response as well as for the re-myelination process while the disruptions of lipid homeostasis may affect the integrity of myelin and modulate neurodegeneration (Tetty and van der Mei, 2014).

Regarding psychiatric disorders, recent theories on the neurological alterations of schizophrenia have pointed the connection of this pathology with the alterations in phospholipid metabolism, particularly to an increased activity of phospholipase-A and a diminished activity of the systems which incorporate polyunsaturated fatty acids (PUFAs). Claiming that the complementation with essential fatty acids may alleviate symptoms of schizophrenia (Shamim et al. 2018).

Therefore, it is clear that many neurological and psychiatric disorders are related to misbalances of lipid homeostasis and numerous lipid biomarkers have been suggested as an early diagnosis tools, as well as an evolution marker for these pathologies (Calvano et al. 2019; Vaqas et al. 2015). However, the precise role of the involved lipid species in the onset and progression of neurodegenerative disorders remains mostly unclear (Alza et al. 2021; Shamim et al. 2018; Ehehalt et al. 2003). To obtain basic information in this direction, we first focused our investigation on determining the relation between the lipid organization on the plasma membranes of hippocampal neurons and the neuronal activity. To address it, we modulated neuronal activity relying on inhibitory or excitatory drugs, and used time of flight secondary ion mass spectrometry (ToF-SIMS) imaging to analyze our samples.

#### 1.2.4 Membrane lipid analysis with ToF-SIMS

ToF-SIMS has already been employed in the analysis of lipid distribution on tissues (Philipsen et al. 2018), single cells (Ren et al. 2019), and more specifically on neurons (Merrill et al. 2017; Passarelli and Winograd 2011).

As previously described in the general introduction of this thesis, time of flight secondary ion mass spectrometry (ToF-SIMS) is based on the principle that at equal charge and kinetic energy, the extracted secondary ions will travel at different velocities depending on their mass-to-charge ratio. To set all extracted secondary ions at the same kinetic energy level, the primary beam needs to be pulsed or bunched (Fletcher et al. 2008a) and secondary ions must be accelerated by an electric field before entering into the ToF sector (Boxer et al. 2009; Agüi-Gonzalez et al. 2019).

Within TOF-SIMS instruments, there are two main types: the ION-SIMS (Iontof GmbH, Germany) and the J105 3D chemical Imager (Ionoptika Ltd). The main difference between them lies in the primary beam. While the Iontof instrument applies a pulsed primary ion

beam, the J105 uses a continuous firing (**Figure 24**). This configuration of the J105 allows the separation of the spatial resolution capability from the mass resolution power and a higher mass resolution. On top of that, the J105 separates in two physical spaces the generation of the secondary ions and the mass spectrometry. With it, the mass resolution power is not affected by the sample topography. Thus, 2D and 3D images with subcellular resolution are achievable, while maintaining a high mass and lateral resolution and it was the instrument employed for our work.

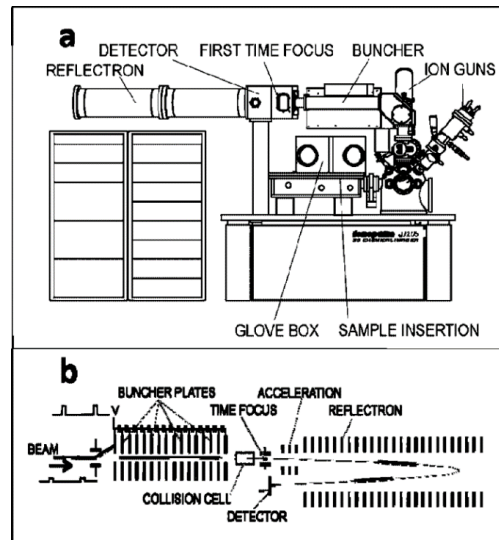


**Figure 24. Ionoptika J105 scheme.** **a)** The chemical imager J105 from Ionoptika, has a Time-of-Flight mass spectrometer and a glove box that permits to load frozen hydrated samples avoiding frosting. **b)** A part of the continuous secondary ion beam is bunched to the first time focus and accelerated in the reflectron, which makes that the path of the ions depends only on their mass to charge ratio and not on their energy. Figure adapted from Fletcher et al. (2008b), courtesy of Elsevier.

One of the main advantages of using ToF-SIMS on the analysis of lipid distribution of the cellular plasma membrane is that this technique admits experiments without specific targets. The lateral resolution of SIMS instruments will be ultimately limited by the diameter of the primary ion beam, which can be focused at  $\leq 200$  nm to image the chemical composition of cellular membranes (Lanekoff et al. 2011). Besides, the number of specific secondary ions sputtered at each voxel may be too low to reconstruct an image and this can limit the achievable lateral resolution. Thus, the useful lateral resolution is often larger than the beam diameter (Kraft and Klitzing 2014). Additionally what is more relevant regarding the analysis of cellular membranes with ToF-SIMS is that these instruments count with an exceptional depth resolution ( $< 10$ nm) (Fletcher 2015; Singh et al. 2020) that enable the reliable imaging of this thin structure.

In addition, to gather the most information out of the analyzed membranes, we need to maximize the detection of intact molecules and reduce their fragmentation. In this regard, the use of GCIB has been shown to enhance the signal levels for high mass molecules by reducing the fragmentation of the secondary ions in comparison to other polyatomic ion beams like  $C_{60}^+$  (Phan et al. 2017) and it was our choice for the analysis of plasma membrane lipids

### 1.3 INTRODUCTION AIM II: DUAL PROBES FOR BIOLOGICAL STUDIES

\*Work based on:

Kabatas S, **Agüi-Gonzalez P**, Saal K, Jähne S, Opazo F, Rizzoli SO and Phan NTN (2019a): Boron-Containing Probes for Non-optical High-Resolution Imaging of Biological Samples. *Angew Chemie Int Ed* **58**, 3438–43

Kabatas S, **Agüi-Gonzalez P**, Hinrichs R, Jähne S, Opazo F, Diederichsen U, Rizzoli SO and Phan NTN (2019b): Fluorinated Nanobodies for Targeted Molecular Imaging of Biological Samples Using Nanoscale Secondary Ion Mass Spectrometry. *J Anal At Spectrom* **34**, 1083–87

---

As described in the aim I of this thesis, it is possible to image specific molecules in a free-label fashion with SIMS techniques such as ToF-SIMS but only a limited range of masses can be covered. Thus, the direct measurement of large molecules, like peptides or proteins, is still not possible. This is unfortunate, since the spatial resolution of SIMS has greatly improved in the last years, enabling cell imaging and even reaching subcellular levels, which implies that excellent protein imaging could be achieved, if specific protein-labeling probes could be obtained. Such probes are especially needed since the contrast of SIMS images is not sufficient to detect organelles or protein complexes according to their morphology, as in electron microscopy (EM) (Weber et al. 2021; Gardiner et al. 2021). This restrains the direct identification of cellular organelles and forces the use of specific probes to point where particular organelles or even smaller targets, as proteins, are located. Thus, and despite the recent developments and the optimization of SIMS imaging methods to address biological studies, the main current drawback of SIMS is the identification of specific cellular structures and organelles as well as the difficulties to localize specific POIs.

In the last years, several probes have been developed to localize specific proteins with SIMS, conjugating antibodies with heavy metals such as lanthanides (Angelo et al. 2014) or gold (Wilson et al. 2012; Thiery-Lavenant et al. 2014). Unfortunately, some features of the antibodies such as their bivalency, polyclonality, and especially their large size may introduce some artifacts (Sograte-Idrissi et al. 2020). The common approach of labeling with primary and functionalized secondary antibodies gives a displacement error of  $\sim 30$  nm from the targeted molecules (Sograte-Idrissi et al. 2020). Furthermore, antibodies are bivalent probes (owning two epitope-binding domains) and secondary antibodies secreted by different B cell lineages (polyclonal antibodies) are often incubated simultaneously, this may cause the artificial aggregation of antibodies in live staining or low fixated samples (Maidorn et al. 2019; Sograte-Idrissi 2019). To avoid these drawbacks, smaller and monovalent probes such as aptamers (Opazo et al. 2012) or single-domain antibodies (sdAb), also known as nanobodies, can be used to remove some of the antibody inconveniences (Opazo et al. 2012; Maidorn et al. 2019).

The most common antibody found in nature is the immunoglobulin G, a protein of  $\sim 150$  kDa that consists of two identical heavy and two identical light chains covalently bound by disulfide bonds (**Figure 25A**). Antibodies recognize the epitope of the antigen by an interplay

between the variable domain of the heavy chain (V<sub>H</sub>) and the variable domain of the light chain (V<sub>L</sub>) (Schumacher et al. 2018). In the nineties, a special type of immunoglobulin was found in camelids, such as llamas or alpacas, and later also found in sharks. These particular immunoglobulins, called heavy chain antibodies (hcAbs) lack the light chain of IgGs as well as the constant domain 1 of the heavy chain (C<sub>H1</sub>) (**Figure 25B**). In this type of antibodies, the antigen binding capacity relies on its single variable domains (V<sub>HH</sub>). Thus, in an independent manner, this portion of the hcAbs can be used as an immunoaffinity tool. Due to their small size  $\sim 14$  kDa, recombinant VHHs are also referred as nanobodies (**Figure 25C**).

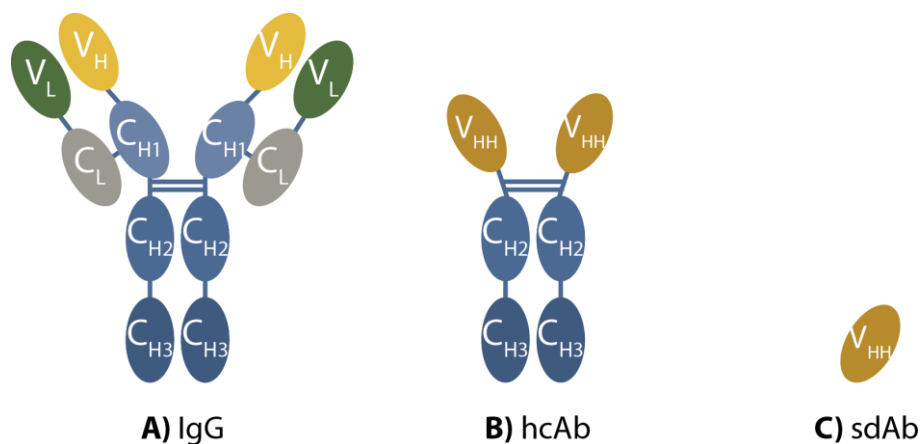


**Figure 25. Comparison of nanobodies and antibodies.** **A)** Conventional antibodies (IgG) are conformed by two heavy chains, which have three constant domains (C<sub>H1-3</sub>, Blue) and one variable domain (V<sub>H</sub>, light yellow) and two light chains, conformed each of them by one constant (C<sub>L</sub>, grey) and one variable domain (V<sub>L</sub>, green). **B)** Heavy-chain antibodies (hcAb) do not contain neither the light chain nor the C<sub>H1</sub> domain and bind their antigen epitopes through single variable domains, V<sub>HH</sub> (dark yellow). **C)** Single-domain antibodies (sdAb), also referred as Nanobodies (Nbs), consist of a single variable domain V<sub>HH</sub> (dark yellow) with the ability to recognize and bind the antigens.

Nanobodies own multiple advantages regarding specific labeling of POIs in biological samples. Among others, these monovalent single-domain antibodies, which are  $> 3$  times smaller than common antibodies (**Figure 25C**), offer a more accurate location of the targets together with a better penetration in cells and tissue facilitating the labeling of previously inaccessible epitopes (Maidorn et al. 2019). Furthermore, thanks to the simplicity of their post-translational modification, nanobodies can be expressed as recombinant proteins in bacteria, simplifying and reducing the cost of their production (Muyldermans 2013). The use of nanobodies also enables a direct premixing with a primary antibody or primary nanobody, decreasing the experimental time in comparison with the use of secondary antibodies, and also admitting experiments with different primary antibodies from the same species (Sograte-Idrissi et al. 2020).

According to the mentioned reasons, we developed several types of nanoprobe for the study of biological samples with SIMS. One of those probes is based on click chemistry reaction, aiming to label newly synthesized proteins while the others are nanobody-conjugated probes that aim to label specific POIs. Moreover, all these nanoprobe do not only enable de detection of proteins at a subcellular level with SIMS, but thanks to the fluorophore molecules that they carry, such proteins can also be localized with light microscopy.

### 1.3.1 Binding strategies

To label our targets, four main strategies were applied. The first approach relies on a click chemistry reaction (**Figure 26A**). In the presence of copper, a copper(I)-catalyzed azide-alkyne cycloaddition (CuAAC) reaction directly binds the nanoprobe to unnatural amino acids (UAAs) that carry an alkyne group. With the use of this clickable nanoprobe, by incubating

cells with UAAs, either unspecific labeling of all newly synthesized proteins or site-specific labeling that enables the detection of specific proteins of interest can be performed.

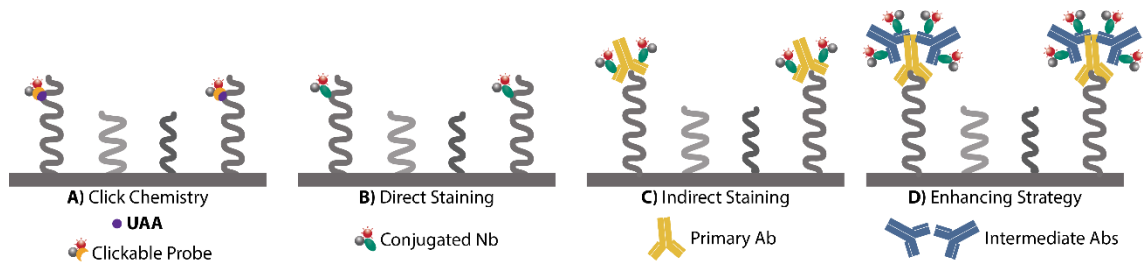


**Figure 26. Strategies to bind conjugated probes to cellular proteins. A)** Click chemistry reaction to bind conjugated probes to unnatural amino acids (UAA). **B)** Direct immunostaining with a conjugated nanobody binding the protein of interest (POI). **C)** A primary antibody binds the POI followed by a secondary conjugated nanobody that binds to the primary Ab. **D)** The nanobodies are added in a final step after first applying a primary antibody that binds the POI and intermediate antibodies that serve to amplify the signal.

For the non-specific labeling, a particular amino acid, such as methionine, is excluded from the incubation medium and replaced by its unnatural homolog (e. g. homopropargyl-L-glycine (HPG)). Since the UAAs will be later bond by click reaction to the SIMS-detectable probes, all newly synthesized proteins can be detected (**Figure 27A**). Alternatively, the unnatural amino acids can be incorporated only into specific proteins by expressing on the cells a modified version of such proteins that contains an amber stop codon (TAG) together with a pair of tRNA and aminoacyl-tRNA synthetase (tRNA/RS). This tRNA/RS pair will incorporate the UAA (e. g. propargyl-L-lysine (PRK)) at the specific site determined by the Amber stop codon. The nanoprobe will then bind the PRK by click reaction, labeling exclusively the POIs (**Figure 27B**).

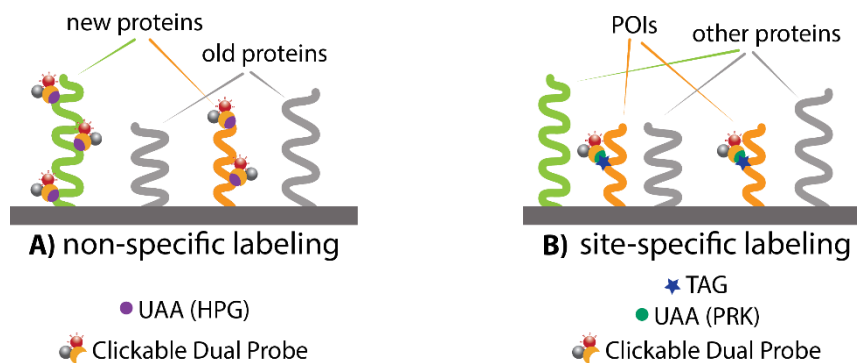


**Figure 27. Clickable nanoprobe binding strategies. A)** The removal of a particular amino acid from the culture medium and its replacement by an unnatural amino acid (HPG) enables the non-specific labelling of all newly synthesized proteins. **B)** Genetically encoded targets, where unnatural amino acids (PRK) are specifically incorporated allow the site-specific labeling of proteins of interest (POI).

Second, direct immunostaining with conjugated nanobodies that allows the labeling of specific POI (**Figure 26B**). Together with the click reaction approach, this modality produces the smallest displacement error from the targeted molecule but as drawbacks, a specific nanobody must be obtained for each target and the produced signal levels are the weakest of the four strategies. The third strategy follows indirect immunostaining, where a primary antibody binds the epitope of the POI while the conjugated nanobody binds the epitope of the primary antibody (**Figure 26C**). With this approach, a single type of nanobody, like an anti-mouse nanobody, can be applied to label multiple molecular targets. Nevertheless, the linkage distance from de POI is bigger than with the direct staining. However, since two nanobodies bind the two heavy chains of the antibodies, the signal can be up to 2 times stronger than the signal obtained with direct staining. Fourth, following an enhancement strategy, intermediate antibodies from different species that bind the previously attached ones are

introduced (**Figure 26D**). An example of this would be the following staining sequence: first applying a rabbit anti-Tom20 primary antibody, followed by an intermediate goat anti-rabbit antibody, and finally adding an anti-goat conjugated-nanobody. As with the indirect staining, the enhancing strategy allows the use of the same type of nanobodies to target different POIs and increases even further the signal intensity obtained with SIMS or/and microscopy but at the same time multiplies the linkage error.

### 1.3.2 Nanoprobes

As a consequence of its high resolution, NanoSIMS has lately increased the number of applications for biological studies. However, this and of course other SIMS techniques with a lower lateral resolution still depends on exogenous markers to enable the differentiation of diverse cellular structures and organelles in order to obtain reliable information and to understand the underlying molecular mechanisms of cellular processes. Apart from a high affinity and specificity, to localize specific biomolecules in SIMS, immunoaffinity probes must offer a good ionization ability as well as containing ions that are not naturally abundant on the analyzed sample. Ideally, the labeling method to localize specific targets must be reliable and straightforward, enabling also the detection with other techniques to explore other features, obtaining even additional information from the same experiments.

In our group, several conjugated probes that enable the labeling and localization of proteins with SIMS imaging and light microscopy have been successfully developed, and applied in the study of biological samples. As further described in the next sections of Aim II, first, a fluorinated nanobody, denominated “FluorLink” was developed and tested with NanoSIMS. Then, also to cover the positive ionization mode of SIMS, two boron-conjugated nanoprobe were developed; “BorEncode”, which binds its targets (UAAs) by click reaction, and “BorLink”, which contains a nanobody and binds its POIs by immunoaffinity.

## 1.4 INTRODUCTION AIM III: STUDY OF THE MYELIN TURNOVER COMBINING ELECTRON MICROSCOPY AND SECONDARY ION MASS SPECTROMETRY

\*Work based on:

Meschkat M, Steyer AM, Weil M-T, Kusch K, Jahn O, Piepkorn L, **Agüi-Gonzalez P**, Phan NTN, Ruhwedel T, Sadowski B et al. (2022): White Matter Integrity in Mice Requires Continuous Myelin Synthesis at the Inner Tongue. *Nat Commun* **13**, 1163

### 1.4.1 Imaging techniques correlation

To analyze biological samples, especially when addressing complex questions, the combination of different approaches can offer a broader view providing further valuable information. With this purpose, several studies have already combined SIMS with other imaging techniques. For example, ToF-SIMS and atomic force microscopy were merged by

Eachambadi and colleagues to resolve the electrically conductive structures in cable bacteria (Eachambadi et al. 2021) as well as NanoSIMS imaging has been correlated with transmission electron microscopy (TEM) to study the dopamine distribution across neuroendocrine vesicles (Lovrić et al. 2016) or the accumulation of amiodarone within the lysosomes of macrophages at the lungs (Jiang et al. 2017).

SIMS extracts the chemical composition of the analyzed surfaces and can generate images with a lateral resolution comparable to light microscopy. In biology, the addition of rare isotopes and non-native elements can also be introduced to study metabolic processes, as well as to unravel the turnover of concrete biomolecules with SIMS. However, the approach that currently achieves the best spatial resolution to discern subcellular structures by morphology relies on the use of electron microscopy (EM). With this technique, electron-dense elements are visualized reaching a nanometer to sub-nanometer precision (Gardiner et al. 2021). Despite, specific immune-EM approaches are available, these methods still present some technical difficulties and require extensive optimization (Rostaing et al. 2004; Morpew 2007; Möbius and Posthuma 2019). Therefore, in the vast majority of the studies, EM identifies specific components only based on their morphology. By combining both methods, EM and SIMS, we can obtain the spatial resolution that allows us to clearly identify organelles and other cellular elements by morphology while addressing the chemical composition and metabolic fate of their biomolecules. In the work detailed below, we combined these two approaches to study the renewing mechanism of myelin sheaths.

#### 1.4.2 Myelin

Myelin is an insulating layer that wraps axons improving their electrical transmission efficiency. Myelin isolation reduces the capacitance of the axonal membrane allowing electrical impulses to transmit faster and efficiently along the nerve cells. Myelination presents some differences between the central nervous system (CNS) and the peripheral nervous system (PNS). In the CNS, the oligodendrocytes are the responsible glial cells to produce the myelin sheaths, emitting multiple plasma membrane prolongations that surround axon segments of up to 40 neurons (**Figure 28A**). Alternatively, in the PNS, Schwann cells surround axons, individually wrapping themselves around a single axon (**Figure 28B**). In both cases, myelin does not form a single sheath that covers the whole axon, but myelin leaves gaps between the wrapped sections, called nodes of Ranvier (**Figure 28**). These non-myelinated sections are the places where ions are exchanged across the axon membrane, regenerating the action potential between regions of the axon that are insulated by myelin (the internodes). This enables the propagation of the action potentials along the axons jumping from node to node, increasing the conduction velocity of the action potentials.

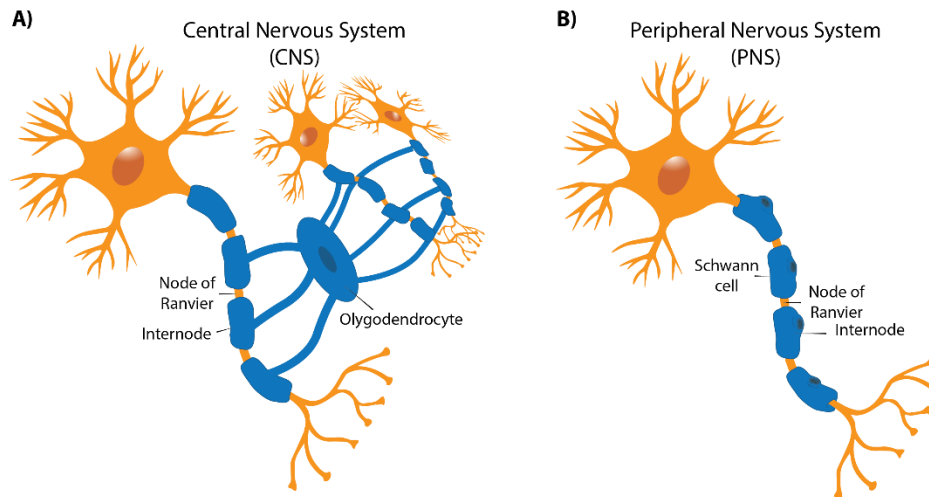


**Figure 28. Myelination in the peripheral and central nervous systems.** **A)** In the CNS, the oligodendrocytes are the cells that extend plasma membrane structures to support axons from multiple neurons. **B)** In the PNS, several Schwann cells surround a single axon leaving gaps known as nodes of Ranvier

In both scenarios, CNS and PNS, the structure wraps itself around the axon forming a mesaxon, where both edges get in contact (**Figure 29B**). After this, one of the prolongations slides under the other and continues to grow wrapping itself around the axon (Snaidero et al. 2014). This leading edge is called the internal mesaxon (**Figure 29C**). Likewise, the membrane also extends laterally along the axon in a series of layers forming the neurilemma. To reach the typical tighten roll structure, the compaction process commences in the outer layers while the inner tongue is still being extended around the axon. Myelin Basic Protein (MBP) is the key component of the compaction process, and it is crucial that compaction does not interfere with the still ongoing wrapping process. Despite compaction regulation mechanisms are not totally uncovered, once MBP is bound to two myelin sheath layers, it rapidly polymerizes and compacts the membrane (Aggarwal et al. 2013).

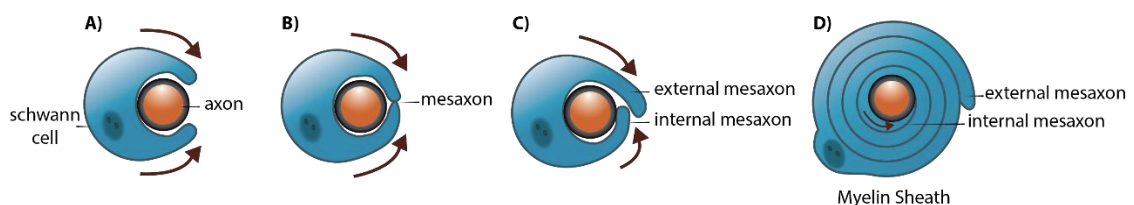


**Figure 29. Myelin sheaths formation stages.** **A)** The axon lies in an invagination of the Schwann cell. **B-C)** The prolongation called the mesaxon, elongates in a spiral fashion wrapping the axon. **D)** Finally, the cytoplasmic surfaces condense into a compact myelin sheath.

### 1.4.3 Myelin turnover

Previous studies have shown that myelin proteins have an exceptionally long lifetime (Fornasiero et al. 2018; Toyama et al. 2013), with a half-life that ranges from 55 to 133 days (Fornasiero et al. 2018). As already mentioned, to study the metabolic turnover of cellular proteins with SIMS, the addition of stable isotope-labeled amino acids (SILAC) in the diet of cells and animals is a common approach. The rare stable isotopes, typically  $^{13}\text{C}$  or  $^{15}\text{N}$ , are metabolically and physiologically incorporated in the newly synthesized proteins, which can then be identified and visualized by SIMS (Dörrbaum et al. 2018; Heo et al. 2018). In collaboration with the group of Dr. Möbius and employing a model of mice that produces myelin but fails to maintain the physiological compaction of the myelin sheaths, we combined 3D electron microscopy and NanoSIMS to study the metabolic turnover of myelin and its relationship with the alteration of its functions. Combining these two techniques, we



were able to visualize the distribution of newly synthesized proteins into mature myelin sheaths and observe that different myelin and axonal structures present different turnover rates.

Likewise, previous works suggested that individual myelin sheath are renewed by the oligodendrocytes in a continuous but very slow process (Toyama et al. 2013; Fornasiero et al. 2018). In this study, working with a tamoxifen inducible MBP null allele, we checked the integrity of myelinated tracts after avoiding the physiological compaction of the newly formed myelin membranes in the CNS of adult mice. Employing an inducible gene knockout (iKO) mouse, in which a targeted gene can be inactivated at a specific time point and only at specific tissues, provided spatial and temporal control over the gene activity. In such mice, oligodendrocytes continued expressing myelin genes, but failed to keep compacting the myelin sheaths (Meschkat et al. 2020). Imaging the spinal cord of the  $^{13}\text{C}$ -lysine pulse-fed mice with NanoSIMS, we directly observed the integration of newly synthesized proteins into the myelin sheath of adult mice.

## 1.5 INTRODUCTION AIM IV: CORRELATIVE FLUORESCENCE MICROSCOPY, TRANSMISSION ELECTRON MICROSCOPY AND SECONDARY ION MASS SPECTROMETRY (CLEM-SIMS)

\*Work based on:

Lange F\*, **Agüi-Gonzalez P\***, Riedel D, Phan NTN, Jakobs S and Rizzoli SO (2021): Correlative Fluorescence Microscopy, Transmission Electron Microscopy and Secondary Ion Mass Spectrometry (CLEM-SIMS) for Cellular Imaging. PLoS One 16, e0240768

### 1.5.1 Imaging techniques correlation

Despite the multiples advantages of combining EM and SIMS, this tandem still has some limitations, for instance, covering a crucial point in the study of biological samples, the localization and visualization of specific targets. The most common approach to map the distribution of particular targets, like proteins, in biological samples relies on light microscopy. Nonetheless, light microscopy still misses relevant information about cellular morphology and offers a limited capacity to uncover metabolic details.

As already addressed in Aim II, without specific probes SIMS also remains unable to distinguish, organelles and other sub-cellular elements. Different alternatives have been tested for SIMS (Kabatas et al. 2019b; 2019b; Thiery-Lavenant et al. 2014), but the use of such probes is still very limited since none of them is currently commercially available. Thus, combining SIMS with either EM (Arrojo e Drigo et al. 2019; Toyama et al. 2019; Lovrić et al. 2016) or light microscopy (Saka et al. 2014; Truckenbrodt et al. 2018; Senyo et al. 2013) has been a more prevalent choice. Still, the correlation of images from the three techniques

(EM, light microscopy, and SIMS) could provide a wider view unraveling information that combining only two of them would be dismissed.

For example, in the work of Truckenbrodt and colleagues (Truckenbrodt et al. 2018), the concatenation of fluorescence microscopy and NanoSIMS suggests that after their synthesis, synaptic vesicles are only functional for a few days while older vesicles seem to be excluded from the releasing neurotransmitter process. However, fluorescence and SIMS could not provide information regarding the morphology or the identity of the cellular elements surrounding the identified vesicles by light microscopy. It is also possible that aged vesicles are isolated in other cellular compartments (Rizzoli and Betz 2005) or fused to synaptic endosomes, inducing morphological and functional changes (Rizzoli 2014). In contrast, thanks to the synergy of the three techniques, these hypotheses could be tested by CLEM-SIMS.

As well, other studies that combine EM with SIMS could also benefit from the inclusion of fluorescence microscopy. For example, the works of Arrojo e Drigo and Toyama in which they described the mosaicism found in several organs where both old and new cells coexist (Arrojo e Drigo et al. 2019, Toyama et al. 2019), could have been expanded by targeting fluorescently specific markers that reveal the key differences between both groups of cells.

Thus, correlative light and electron microscopy (CLEM), sums the advantages of both approached, granting the analysis of specific targets in the context of particular cell structures (Sims and Hardin 2007), while adding SIMS would also provide the chemical composition of cells and tissues and hints about their metabolic fates.

As shown in the previous Aim, to maintain their physiological capabilities, cells and tissues are constantly replacing their old components to avoid the progressive accumulation of old or damaged material. Despite it is possible to visualize with fluorescence microscopy some recently incorporated cellular proteins, by employing pulses of non-canonical amino acids (Dieterich et al. 2010), this approach only reveals the newly-synthesized proteins. On the contrary, SIMS also provides information about the general abundance, offering an integral overview of the metabolic turnover for different types of biomolecules (Truckenbrodt et al. 2018; Frisz et al. 2013).

### 1.5.2 CLEM-SIMS

Being aware of the strengths and limitations of each of these three techniques and to overcome the individual constraints, we developed a workflow that allows a straightforward correlation of light and electron microscopy together with nanoscale secondary ion mass spectrometry (CLEM-SIMS). After optimizing the multiple steps, we generated a suitable and straightforward CLEM-SIMS protocol that, as a proof of concept, allowed us to determine the location of specific proteins (fluorescence microscopy) together with the visualization of cellular structures (TEM) while also obtaining information related to the chemical composition of the cells (NanoSIMS) in cultured cells (**Figure 30**).

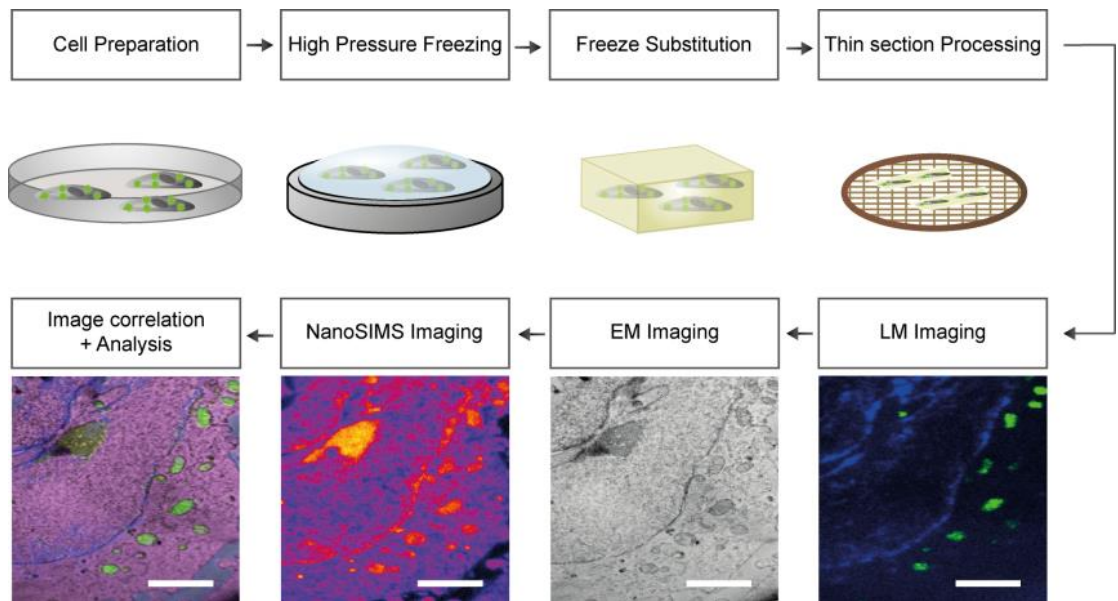


**Figure 30. Workflow overview for CLEM-SIMS imaging.** Following conventional protocols, cells are cultured and stained. Then, the cells are physically fixed by high pressure freezing, previous to their freeze substitution procedure. After this, when the sample is already embedded in resin, the blocks can be sectioned. The slides must be placed on conductive and referenced grids. Thanks to the grid and the intrinsic landmarks of the cells, the fluorescent microscopy imaging can be carried, followed by TEM and NanoSIMS imaging of the exact same areas. The images from the three modalities are then processed for registration and the data analyzed. Scale bars:  $3\mu\text{m}$ . Figure extracted from Lange et al. (2021), courtesy of PlosOne.

## 2. MATERIAL AND METHODS

### 2.1 MATERIAL AND METHODS AIM I

#### 2.1.1 Hippocampal neurons culture

To obtain well developed hippocampal neurons while minimizing the interference of the glial cells we followed the protocol of Kaech & Banker (2006). The three parts of the protocol that will be chronologically described (**Figure 31**), enabled the culture of hippocampal neurons maintaining a physical distance from the astrocytic monolayer. All solutions and products used for this preparation are summarized on (**Table S1**).

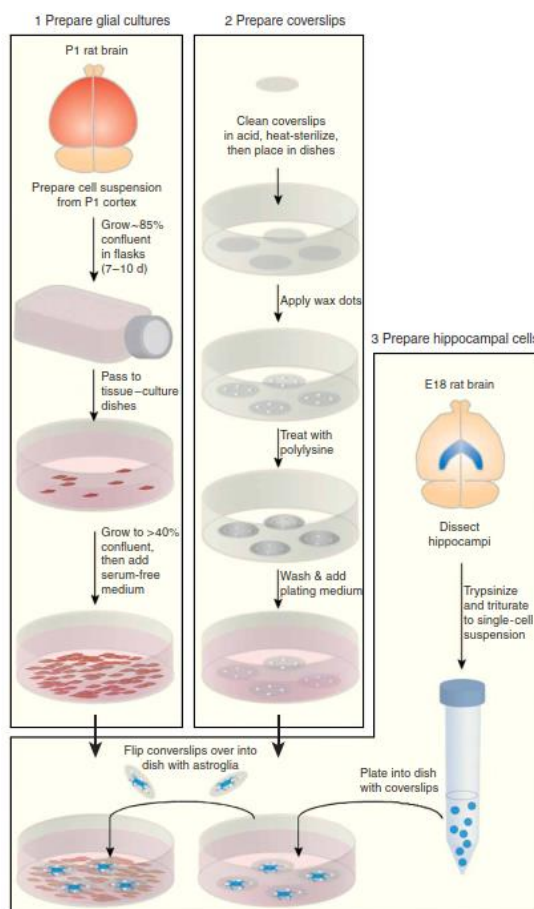


**Figure 31. Banker culture workflow.** Schematic representation of the three parts of the workflow for hippocampal neurons culture; glia, coverslips and hippocampal neurons preparation. Figure extracted from Kaech and Banker (2006), courtesy of Nature.

##### 2.1.1.1 Glia preparation:

The preparation of cortical glial cells must commence two weeks before starting with the hippocampal culture (**Figure 31.1**). For this purpose, the brains of newborn 6-7 (P0) rats were extracted from the skull and immediately submerged in Hanks' Balanced Salt Solution (HBSS). Under the microscope, the cerebral hemispheres were cleaned from the meninges. Once the 12-14 hemispheres were ready, still submerged in HBSS, they were finely cut in approximately equal size pieces of ~ 1 x 1mm with a sterile scalpel. The brain pieces were

transferred into a centrifuge tube with a total volume of 10ml of HBSS + 10mM HEPES (4-(2-hydroxyethyl)-1-piperazineethanesulfonic acid). There they were gently washed by repeatedly inverting the tube, letting the pieces sit at the bottom of the tube, removing the supernatant, and re-suspending in fresh solution. Repeating this step 3-4 time, helps to remove the very small tissue pieces that remained floating on the solution and that may be toxic for the cells. After the last washing, most of the supernatant was removed and the pellet was transferred to a new tube containing dissociation buffer (12 mL HBSS, 1.5 mL 2.5 % trypsin, 1.5 mL 1 % DNase). To let the enzymatic solution act, the centrifugation tube was placed in a rotator at 37 °C for 15 minutes. Then, the dissociation buffer was discarded and the dissociated tissue washed 3 - 4 times with preheated glia medium. Vigorously pipetting against the bottom of the tube, the dissociated tissue was homogenized, and then filtered through a 100 µm cell strainer. The filtered solution was then centrifuged at 860 rpm for 10 minutes, carefully removing the supernatant afterwards. The pellet of cells was then re-suspended in 9 ml of glial medium, distributing it into three flasks and completing with glia medium to reach a total volume of 20 ml. The flasks were then placed in the incubator at 37 °C and 5 % CO<sub>2</sub>. After 1 day, the medium was exchanged to remove dead cells and debris. The cortical astroglial cells were then fed every three days with fresh glia medium and shacked once per week in the presence of 10 mM HEPES to detach and remove the microglia. Each of these preparations generates enough glial cells for several preparations of hippocampal neurons.

Five days before the neurons were seeded, the astrocytes were transferred from the flask onto 12 well plates, adding 3ml of trypsin + EDTA to detach the cells. Once the cells were visibly detached, the enzymatic solution was neutralized adding glial medium. Then the solution was centrifuged at 800 rpm for 10 minutes and the pellet re-suspended in the glial medium. ~ 10.000 astroglial cells were seeded per well. One day before seeding the neurons, once the astrocytes were already attached to the well, the glial medium was replaced by N2 medium.

#### 2.1.1.2 Coverslips preparation:

Before seeding the hippocampal neurons, sterilized ITO glass coverslips were coated overnight with 1 mg/ml Poly-L-lysine adding 4 drops of paraffin on the edges to set up the later “sandwich” arrangement (**Figure 31.2**). After coating, the ITO coverslips were washed with sterile distilled water and then submerged in plating medium.

#### 2.1.1.3 Preparation of hippocampal cells:

Hippocampal neurons were then procured from embryonic rats (E18) (**Figure 31.3**). The hippocampi were isolated under the microscope and then washed with HBSS, then incubated for 1 h in an enzymatic solution that contains: 10 ml Duplecco's Modified Eagle Medium (DMEM), 50 mM EDTA, 100 mM CaCl<sub>2</sub>, 2 mg of cysteine, and 25 U/ml of papain. Then bubbled with Carbogen for 10 min and filtered. After this, the cells were washed with HBSS and incubated in inactivating solution (10 ml FCS-DMEM, 2 mg albumin, and 2 mg of trypsin inhibitor) for 15 min.

The neurons were then plated (~ 30.000 cells/cm<sup>2</sup>) on the ITO glasses and let to seed for 1-4 h at 37 °C and 5 % CO<sub>2</sub>. When the cells were already attached to the glass, the medium was exchanged to Neurobasal-A medium supplement with B27 (1:50), and GlutaMAX (1:100). To limit the proliferation of the glial cells, after 3 days, 5-fluoro-2'-deoxyuridine was added. Neurons were kept in the cell incubator at 37 °C and 5 % CO<sub>2</sub> for 14 days before their use.

## 2.1.2 Fixation methods

### 2.1.2.1 Chemical fixation

Before fixing, the culture medium of the neurons was removed and the coverslips were rinsed with 0.1 M of Hendry phosphate buffer (HPB) pH 7.4. Then the cells were fixed at room temperature for 30 minutes in a solution of glutaraldehyde 4 % in 0.1 M HPB. The fixation solution was removed and the coverslips washed twice for 5 minutes in triple distilled water and fixed with 0.4 % osmium tetroxide ( $\text{OsO}_4$ ) for 15 minutes at room temperature. The fixed samples were then washed 3 times for 5 minutes in triple distilled water and let air dry before imaging.

### 2.1.2.2 Frozen-hydrating

The frozen-hydrated samples were first washed for 5 min with 0.1 M HPB (pH 7.4) and rinsed 4 - 5 times (total rinsing time  $\sim$  15 - 20 sec) with 150 mM ammonium formate (pH 7.4). Rapidly, the cells were plunge frozen by submerging them in liquid propane and immediately transferred and stored in liquid nitrogen. The samples remained immersed in liquid nitrogen until they were inserted into the precooled ToF-SIMS instrument.

### 2.1.2.3 Freeze-drying

Like previously described for the frozen-hydrating samples, the cells were first washed for 5 min with 0.1 M HPB (pH 7.4) and rinsed 4 - 5 times (total rinsing time  $\sim$  15 - 20 seconds) with ammonium formate 150 mM (pH 7.4). Immediately after, the cells were immersed in liquid propane and dried overnight, setting a final pressure of 0.05 mbar in the lyophilizer (Christ 2-4 LDPlus, Christ Martin, Germany). The samples were then shortly reserved in a glass desiccator until their transference into the mass spectrometer where they were analyzed at RT.

## 2.1.3 ToF-SIMS imaging

For the ToF-SIMS imaging, a J105 3D Chemical Analyzer (Ionoptika Ltd., UK) was employed, applying a 40 keV  $(\text{CO}_2)_{2500}^+$  gas cluster ion beam (GCIB) primary ion source. To avoid the potential interference of the ice layer formed on top of certain samples or possible surface contamination, the first layer was eroded applying a primary current of  $4 \times 10^{13}$  ion/cm<sup>2</sup> on an area of 800 x 800  $\mu\text{m}$  and 128 x 128 pixels. The actual imaging was executed, for both secondary ion modes, under the static limit. A primary ion current of 12 pA was applied to areas of 750 x 750  $\mu\text{m}$  setting images of 256 x 256 pixels, with an estimated primary ion dose density of  $2 \times 10^{13}$  ion/cm<sup>2</sup>. To adjust the mass range to the masses where numerous lipids and their fragments are found, the detection mass range of the instrument was set from 80 to 1000 Da.

For the analysis of chemical fixated and frozen-dry samples, we kept the mass spectrometer at room temperature. On the contrary, to work with the frozen-hydrated samples, before inserting the samples, both the preparation and the analysis chambers were cooled down to  $\leq 200$  K and  $\leq 90$  K, respectively. Keeping the temperature of the analysis chamber during the entire measurement.

## 2.1.4 Mass spectra calibration

To calibrate the spectral mass/time axis we localized characteristic peaks along the spectra. For positive mode the selected peaks were In ( $m/z$  114.90), PC headgroup ( $m/z$  184.07),

In<sub>2</sub>O (m/z 245.80), DAG (m/z 599.47) and PC (m/z 760.58). For the negative mode: InO<sub>2</sub> (m/z 146.89), FA (18:0) (m/z 283.26), PE (37:0) (m/z 760.58) and TG (54:2) (m/z 885.79).

### 2.1.5 Data analysis

The data that we got from the J105 was exported using the Ionoptika Image Analyzer software (Ionopika Ltd., Southampton, U.K.). Due to the enormous size, the mass spectra data was binned down to 0.05 Da, resulting in spectra of > 10k peaks with a mass accuracy of ~ 62 ppm at m/z 800. To clean the spectra of the substrate interferences, the most abundant peaks known to come from the ITO glass were removed. The intensity of the remaining peaks was then normalized to the total ion counts of each image. Further processing of the data was achieved with Matlab (R2017a, The Mathworks, Inc., Natick, MA).

To determine how the lipid composition varies across two different cellular regions (cell body and neurites) of the neuronal plasma membranes, and to analyze how the application of drug treatments affects their lipid composition, we combined independent component analysis (ICA) and cross-correlation coefficient difference (CCD) analysis. Afterwards, the masses that showed to contribute significantly to the differences between cells incubated with drugs and the control group were tentatively identified using literature references as well as Lipid Maps and LipidBlast databases (Sud et al. 2007; Kind et al. 2013). To confirm the statistical correlation between lipid subgroups variations and neuronal activity, a Kruskal–Wallis test was combined with the Tukey–Kramer post-hoc test, applying a correction alpha of 0.05 for individual subgroups of lipids.

## 2.2 MATERIAL AND METHODS AIM II

### 2.2.1 Sample preparation for FluorLink

#### 2.2.1.1 Cell culture and transfection

HEK293 cells were cultured in DMEM medium with a 10 % FCS, 100 U/mL penicillin and streptomycin, and 4 mM L-glutamine. For the experiment, the cells were seeded on PLL-coated coverslips and incubated in DMEM, without antibiotics, at 37 °C with 5 % CO<sub>2</sub>. For transfection with TOM70-mCherry and TOM70-GFP the cells were treated as instructed by the manufacturer of Lipofectamine® 2000.

#### 2.2.1.2 Immunostaining

Before immunostaining, cells were fixed with 4 % PFA in PBS for 30–40 min at RT, quenched with 100 mM glycine in PBS, washed briefly with PBS, and permeabilized and blocked with 2.5 % BSA and 0.1 % Triton X-100 in PBS for 15 min. The following POIs were the targets of FluorLink in the presented work; TOM70-GFP (transfected), TOM70-mCherry (transfected), PMP70 (endogenous), Lamin-B2 (endogenous), and  $\alpha$ -Tubulin (endogenous).

**Direct immunostaining approach targeting fluorescent proteins (FP):** The fixed, blocked and permeabilized cells were incubated with both FluorLink-nanobodies anti-FP (#1 and #2) for 1 h at RT in 1.25 % BSA and 0.05 % Triton X-100 in PBS and washed with PBS for 3×5 min. The following FluorLink-nanobodies were used for staining: FluorLink-nanobody anti-GFP #1 and #2 (40 – 50 nM each) and FluorLink-nanobody anti-mCherry #1 and #2 (40 – 50 nM each).

**Indirect immunostaining approach targeting POI:** The fixed, blocked and permeabilized cells were incubated with the primary antibody for 1 h at RT; anti-PMP70 (1:100), mouse anti-Lamin-B2 (1:100) or mouse anti- $\alpha$ -Tubulin (1:100). After the primary antibody staining, the cells were washed with permeabilization/blocking solution (3×5 min) and sequentially stained with the intermediate antibodies for 1 h at RT; goat anti-rabbit IgG-Alexa488 (1:50), mouse anti-goat (1:50). Afterwards the cells were washed with permeabilization/blocking solution (3×5 min) and incubated with FluorLink-nanobody anti-mouse IgG (25–50 nM) in 1:1-diluted blocking/permeabilization solution for 1 h at RT followed by final wash with PBS (2×5 min). The cell nuclei were then labeled using 4  $\mu$ M Hoechst in PBS for 5 min. This was followed by washing with PBS, high-salt PBS and PBS (5–10 min each) and mounting in Mowiol for pre-embedding fluorescence imaging.

## 2.2.2 Sample preparation for BorEncode

### 2.2.2.1 Cell culture and labelling of all newly synthesized proteins

To label proteins via click chemistry with BorEncode, baby hamster kidney (BHK) cells were grown in DMEM, with 10 % tryptose phosphate, 5 % fetal bovine serum, 2 mM L-glutamine, 60 U/mL penicillin and 60 U/mL streptomycin and passaged every 3–4 days. In order to label a large number of newly synthesized proteins with BorEncode, cells were grown on 18 mm glass coverslips (~ 50.000 cells per coverslip). The culture medium was replaced by methionine free DMEM, supplemented with 2 mM L-glutamine, 500  $\mu$ M L-cysteine, 60 U/mL penicillin and 60 U/mL streptomycin 1 h before starting the experiment. Click-iT® L-homopropargyl glycine (HPG) was added to cells in a final concentration of 50  $\mu$ M. Cells were incubated for 88 h at 37 °C and 5 % CO<sub>2</sub>, thereby incorporating HPG into all newly synthesized protein. The cells were then washed with cold PBS and fixed with 4 % PFA in PBS for 30 min at RT.

### 2.2.2.2 Selective incorporation of UAAs into proteins of interest

BHK fibroblasts were cultured on glass coverslips (~ 20.000 cells per coverslip) in antibiotic free culture medium. 24 h after seeding, the UAA propargyl-L-lysine (PRK) was added to the culture medium in a final concentration of 250  $\mu$ M. Furthermore, cells were transfected with two DNA vectors using Lipofectamine® 2000 reagent following the manufacturer's instructions. Briefly, the DNA encoding the protein of interest (POI), which contains the Amber stop codon, and the vector for the expression of the tRNA/RSWT were equilibrated together in Opti-MEM for 5 min at RT. Lipofectamine was equilibrated separately in Opti-MEM, then added to the DNA constructs, mixed and incubated for 20 min at RT. Afterwards the DNA/Lipofectamine mixture was added to the cells and incubated for 18–24 h at 37 °C and 5 % CO<sub>2</sub> to allow protein expression with incorporation of the PRK. Medium was exchanged to normal BHK culture medium ~ 4 h before fixation. Cells were briefly washed with cold PBS and fixed with 4 % PFA in PBS for 30 min at RT.

### 2.2.2.3 Click reaction

The PFA was quenched applying ammonium chloride (100 mM) in PBS for 20 min at RT before they were permeabilized with 0.1 % Triton-X 100 in PBS. Blocking of unspecific



epitopes was performed by incubating samples in 5 % BSA, 5 % tryptone/peptone (Carl Roth GmbH, Karlsruhe, Germany) and 0.1 % Triton-X 100 in PBS. Directly before reaction, cells were washed with 3 % BSA in PBS and incubated in freshly prepared click solution in a dark humidified chamber for 30 min at RT. Following the manufacturer's instructions, the click solution was composed of milliQ-H<sub>2</sub>O and Click-iT® Cell Reaction Buffer Kit and 10 µM BorEncode. After the click reaction, the cells were washed with 5 % tryptone/peptone in PBS for 15 min.

## 2.2.3 Sample preparation for BorLink

### 2.2.3.1 Cells culture and transfection

COS-7 and HEK293 cells were cultured in DMEM containing 10 % FCS, 100 U/mL penicillin and streptomycin, and 4 mM L-glutamine. For the experiment, ~ 500.000 cells per PLL-coated coverslips coverslip were seeded and incubated in DMEM without antibiotics for 3 - 6 h at 37 °C and 5 % CO<sub>2</sub>. The cells were transfected following the instructions of the manufacturer using Lipofectamine® 2000 and the vector for the protein of interest, TOM70-GFP. The transfection was carried out by separately incubating the plasmids and the Lipofectamine® 2000 for 5 min in OptiMEM Gibco®, then mixing the two solutions and waiting for further 20 - 25 min before applying them to the cells. The cells were allowed to express the proteins of interest for 12 - 19 h at 37 °C.

### 2.2.3.2 Immunostaining

Fixation was performed using 4 % PFA in PBS. This was followed by quenching for 30 - 40 min in 100 mM glycine in PBS and a brief PBS wash before the samples were permeabilized and blocked with 2.5 % BSA and 0.1 % Triton X-100 in PBS for 15 min. BorLink-GFP-Nanobodies (~ 40 – 50 nM) 6 were diluted in blocking/permeabilizing solution/PBS (1 : 1), added to the cells and incubated for 1 h at RT. The cell samples were washed after the labeling step for 5 - 10 min with PBS (2×).

## 2.2.4 Plastic embedding and sectioning

All fixed and labeled cells were dehydrated applying an increasing amount of EtOH in ddH<sub>2</sub>O, first 30 % EtOH for 10 min, then 50 % EtOH for 10 min (x3 times). Then, immersed in a solution of 50 % LR-White in EtOH for 1 h. and in a 100 % LR-White solution for 1 h. Afterwards, the cells were covered with capsules (Beem Inc., West Chester, PA, USA) and embedded for 30 min in LR-White plus accelerator (London Resin Company Ltd) on a cold metal-plate. Eventually, the resin blocks were dried for 90 min at 60 °C and finally cut with an EM-UC6 ultramicrotome (Leica Microsystems, Wetzlar, Germany), in 200 nm sections which were subsequently placed onto silicon wafers (Siegert Wafer GmbH, Aachen).

## 2.2.5 SIMS imaging

### 2.2.5.1 FluorLink

NanoSIMS measurement was performed using a NanoSIMS 50L (Cameca, France) selecting in this case the 8 keV Cesium primary ion source to produce and detect negative secondary ions. To obtain the steady state of ionization before imaging, the surface was implanted with a primary current of ~ 110 pA. A primary current of ~ 2.5 pA was used during the imaging phase to produce secondary ions that were then focused through the ion optics and separated into different mass per charge (m/z). The collected ions were; <sup>19</sup>F<sup>-</sup> and <sup>12</sup>C<sup>14</sup>N<sup>-</sup> (referred on

the rest of the text as  $^{19}\text{F}$ , and  $^{12}\text{C}^{14}\text{N}$ ). The images were acquired with the raster size  $12 \times 12 \mu\text{m}$  to  $20 \times 20 \mu\text{m}$  with  $256 \times 256$  pixels, or  $37 \mu\text{m}$  with  $512 \times 512$  pixels.

### 2.2.5.2 BorEncode and BorLink

SIMS analysis was performed on a NanoSIMS 50L instrument (Cameca, France) selecting the positive ion polarity of the instrument and a Hyperion II dual polarity oxygen as primary ion source. To obtain the steady-state of the secondary ion yield, prior to each analysis, an implantation of O<sup>-</sup> ions was performed with a primary current of  $\sim 190 \text{ pA}$  (primary aperture D1:1) on a slightly larger area than the final imaged area. Sequentially, a primary current of  $\sim 30 \text{ pA}$  (D1:2 primary aperture) was applied, setting a mass resolution power adequate to separate potential isobaric interferences. The detectors were set to detect the following positive ions:  $^{11}\text{B}^+$ ,  $^{23}\text{Na}^+$ ,  $^{39}\text{K}^+$ , and  $^{40}\text{Ca}^{2+}$  (in the text respectively referred as  $^{11}\text{B}$ ,  $^{23}\text{Na}$ ,  $^{39}\text{K}$ , and  $^{40}\text{Ca}$ ). The images range from  $20 \times 20 \mu\text{m}$  to  $40 \times 40 \mu\text{m}$  with  $512 \times 512$  pixels per image and a dwell-time of  $6 \text{ ms/pixel}$ . 5 planes were acquired and accumulated to generate the final images.

### 2.2.6 Data analysis

All the SIMS images were initially exported and processed with the Open MIMS plugin from ImageJ (NIH, Bethesda, USA). Line profiles, drawn for the analysis of FluorLink probe, and all ratio measurements were also performed by this software. Self-written Matlab routines (the Mathworks Inc., Natick, MA) were used for further data analysis. To calculate the average signal intensity of  $^{11}\text{B}$  from the boron probes, circular regions of interest (ROI) were manually selected after being normalized to the background intensities. The background was determined selecting similar ROIs outside the cells. For BorLink, 150 ROIs were selected on transfected and 150 ROIs on non-transfected cells. For BorEncode, 60 ROIs were selected on +HPG cell samples, and 60 ROIs on -HPG samples. The difference of  $^{11}\text{B}$  signal levels between the transfected cells stained with BorLink and the non-transfected cells also incubated with BorLink, was determined as significant ( $p < 0.0001$ ) by a Wilcoxon rank sum test.

## 2.3 MATERIAL AND METHODS AIM III

### 2.3.1 Sample preparation: $^{13}\text{C}$ -labeling

Starting at the age of 28 weeks (18 weeks after the tamoxifen injection), the MBP iKO mice were respectively fed for 45 or 60 days with a  $^{13}\text{C}$ -lysine diet. The pulse-labelling period was then followed by one week of chase with a non-isotopically labeled control diet. Immediately after, their spinal cords were collected.

### 2.3.2 Sample sectioning and mounting

Epon-embedded sections were procured following the protocol described in (Weil et al. 2019). The  $\sim 150 \text{ nm}$  sections from the iKO mice spinal cords were placed on finder grids (FCF200F1-Cu, Science Services, Munich, Germany). The areas of interest were imaged with

TEM at the resolution of interest and mapped using a smaller magnification to facilitate their later localization with NanoSIMS (**Figure 32**).

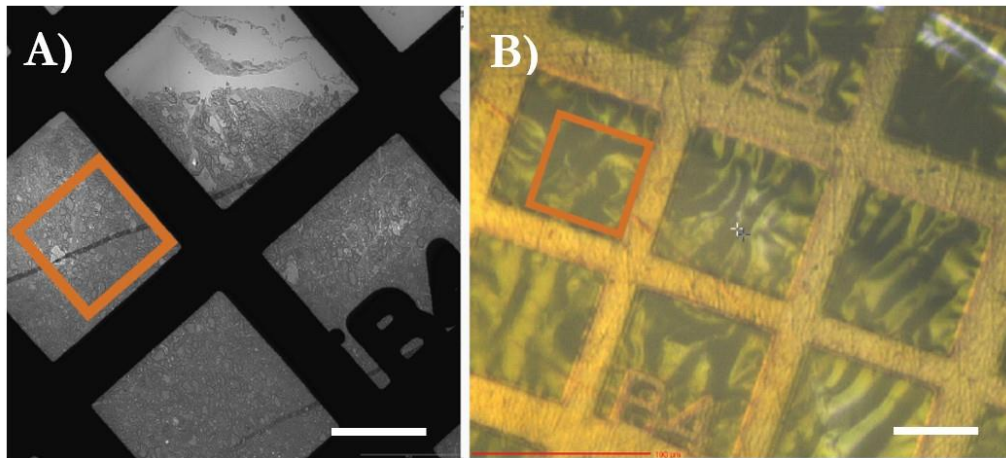


**Figure 32.** TEM low magnification overview of a finder grid used as a guide to locate the same area of interest with NanoSIMS CCD. **A)** TEM image with the ROI pointed with an orange square. **B)** CCD image of the same area. Despite both orientations can differ, the ROI can still be located thanks to the coordinates and the TEM reference image. Scale bars: 50  $\mu\text{m}$ .

### 2.3.3 NanoSIMS imaging

After TEM imaging was carried out, the same areas were imaged with NanoSIMS using a NanoSIMS 50L (CAMECA, Gennevilliers, France) using an 8 keV  $\text{Cs}^+$  primary ion source. The TEM grids were loaded into the NanoSIMS with the help of a sub-holder that accepts up to three TEM grids of 10 mm diameter (#45639345, Cameca, Gennevilliers, France). To determine the presence of  $^{12}\text{C}$  and  $^{13}\text{C}$ , the detectors were set to collect  $^{12}\text{C}^{14}\text{N}^-$  and  $^{13}\text{C}^{14}\text{N}^-$  ions. The mass resolving power was adjusted to avoid isobaric mass peaks interferences like  $^{12}\text{C}^{15}\text{N}^-$  on the  $^{13}\text{C}^{14}\text{N}^-$  peak, or  $^{12}\text{C}_2^2\text{H}^-$  on  $^{12}\text{C}^{13}\text{C}^-$  applying an entrance slit of 20 x 140  $\mu\text{m}$  (ES:3) and an aperture slit of 350 x 250  $\mu\text{m}$  (AS:1). To reach a stable secondary ion yield, areas slightly bigger than the final ROIs were pre-sputtered applying a primary ion current of 15 pA during 30 seconds (D1:1). Then, a primary ion current of 1.5 pA or 0.5 pA was applied for imaging, selecting respectively a primary aperture of D1:3 or D1:4. A dwell time of 5.07 ms /pixel was accumulated from two consecutive layers. Ion images of 256 x 256 pixels were taken for raster sizes ranging from 10 x 10  $\mu\text{m}$  to 20 x 20  $\mu\text{m}$  and 512 x 512 pixels when the raster size was bigger than 20 x 20  $\mu\text{m}$ . Image exportation and drift correction, if required, were performed by the OpenMIMS plugin (NRIMS, Cambridge, MA, USA) from ImageJ (Rueden et al. 2017).

### 2.3.4 Image registration

To determine the  $^{13}\text{C}$  enrichment within concrete morphological structures, the TEM images were scaled to match NanoSIMS data. The correlation of EM and NanoSIMS images was possible in an accurate manner thanks to the intrinsic landmarks of the tissue (e. g. the myelin folds) without requiring extrinsic fiducial markers such as fluorescent beads. The image registration was carried out by selecting multiple points, evenly spread across the entire image and carrying a 2D linear transformation until the localization error between the two types of images were reduce to the minimum using Adobe Photoshop CS6 (Adobe Inc., San José, CA, USA).

### 2.3.5 Isotopic enrichment calculation

To calculate the  $^{13}\text{C}$  enrichment across different areas of interest, we employed self-written Matlab scripts (R2016b, the Mathworks Inc., Natick, Massachusetts, MA, USA). A TEM expert manually drew multiple ROIs on the electron images, including all the analyzed morphological structures. Within each ROI, the isotopic ratio  $^{13}\text{C}^{14}\text{N}/^{12}\text{C}^{14}\text{N}$  was calculated for every pixel (in SIMS, the values are equivalent to the amount of detected ions) and then those values were averaged across all pixels in the ROI and presented as a data point. The standard natural ratio for  $^{13}\text{C}/^{12}\text{C}$  (0.0112) was set as 0 % and the enrichment of particular regions was presented as the percentage over this threshold. The ion maps were pseudo-colored using the Fiji LUT Fire and Physics. In the EM images, ROIs are indicated by numbers denoting the corresponding biological structures that were included in the graphs. To statistically determine the different levels of  $^{13}\text{C}$  enrichment between structures, a two-tailed unpaired t-test was applied.

## 2.4 MATERIAL AND METHODS AIM IV

### 2.4.1 Sample preparation for high-accuracy CLEM

The resin sections were cut with a 35° DiATOME ultra knife with a thickness of ~ 160 nm and placed on carbon-coated Formvar finder grids (Ted Pella 01910-F; Electron Microscopy Sciences, Hatfield, PA, USA). For light microscopy, the areas of interest were taken using a 100x oil immersion objective. To help with the identification of the cells, the DAPI channel was employed to image the uranyl acetate autofluorescence. Then, the respective channels of interest were imaged to reveal the labeled proteins. The grids were then washed, dried, and stored until continuing with the TEM imaging.

To identify the same areas of interest with TEM, overview images with a magnification of 600x were taken first. Then, zooming in, images with a magnification of 3500x of were taken in a tile scan of 10 x 10 images. Overview TEM images of individual cells were obtained by merging the corresponding images. To correlate the light microscopy data with the electron microscopy images, a plug-in from Icy, eC-CLEM (Paul-Gilloteaux et al. 2017), was employed.

### 2.4.2 NanoSIMS imaging

NanoSIMS imaging was performed by a NanoSIMS 50L (CAMECA, Gennevilliers, France) using an 8 kV  $\text{Cs}^+$  primary ion source. The TEM grids were loaded on the NanoSIMS, by placing them on a sub-holder (#45639345, Cameca, Gennevilliers, France). The ion detectors were set to collect  $^{12}\text{C}_2^-$ ,  $^{12}\text{C}^{13}\text{C}^-$ ,  $^{12}\text{C}^{14}\text{N}^-$ ,  $^{12}\text{C}^{15}\text{N}^-$ ,  $^{31}\text{P}^-$  and  $^{32}\text{S}^-$ . The mass resolving power of the instrument was adjusted to avoid the interferences from isobaric mass peaks like  $^{13}\text{C}^{14}\text{N}^-$  from  $^{12}\text{C}^{15}\text{N}^-$ , or  $^{12}\text{C}^{13}\text{C}^-$  from  $^{12}\text{C}_2\text{H}^-$ . Areas slightly bigger than the finally analyzed regions were first pre-sputtered applying an ion current of 15 pA for 30 seconds (D1:1). Afterwards, to image the mito-mCitrine transfected cells, a current of 1.5 pA (D1:3) and a current of 0.5 pA (D1:4) to image the MitoTracker Deep Red FM cells. A dwell time of 5.07 ms /pixel was accumulated and later summed from two consecutive layers of 512 x 512 pixels. The image sizes ranged from 10 x 10  $\mu\text{m}$  to 28 x 28  $\mu\text{m}$ . The exportation and drift correction of the NanoSIMS images were carried by the plugin from Fiji, OpenMIMS (NRIMS, Cambridge, MA, USA).

### 2.4.3 Image registration

To proceed with the high-accuracy CLEM, first the light microscopy data was up-scaled to match the electron micrograph. Then, to proceed with the ion abundance analysis, the electron micrographs together with the fluorescent images were downscaled to match the NanoSIMS data. The accurate correlation of the images obtained with the different techniques was guided by characteristic features and intrinsic landmarks of the cells, not requiring extrinsic fiducial markers. Selecting multiple landmarks across the entire field of view and having a target point as a reference, the image registration was optimized until a minimal localization error was achieved between the correlative images using Adobe Photoshop CS6 (Adobe Inc., San José, CA, USA).

### 2.4.4 Calculation of isotopic enrichment

To analyze the isotopic distribution across different cell structures, we employed self-written Matlab scripts. With them, a minimum of 30 circular ROIs of the same diameter were manually selected on each of these structures. To normalize the ion counts, we normalized the values of the other ions on each pixel by calculating the ratio with the signal of  $^{12}\text{C}$  (e. g.  $^{12}\text{C}^{14}\text{N}/^{12}\text{C}$ ). Then, those values were averaged across all pixels in the ROI and presented as a single data point.

### 3. RESULTS

---

#### 3.1 RESULTS AIM I

The interest in neuronal plasma membrane lipids has remarkably increased in the last decades while exploring the association of such lipids with physiological and pathological processes. Lipid diversity has been related to high cognitive abilities and it has been observed that it is influenced by age, neuronal stress, and neuronal maturation (Lauwers et al. 2016; Mencarelli and Martinez-Martinez 2013). Likewise, it has been proved that membrane lipids go far beyond composing a physical barrier between neurons and their environment. The studies on this field have shown that lipids are highly dynamic biomolecules, involved in an extensive amount of cellular processes such as ion-channel regulation, synaptic exo-, and endocytosis, or synaptic plasticity (Mencarelli and Martinez-Martinez 2013; Merrill et al. 2017; Puchkov and Haucke 2013). Moreover, lipids homeostasis alteration has been linked to neurodegenerative processes such as Alzheimer or Parkinson (González de San Román et al. 2017), neuropsychiatric afflictions like depression or bipolar disorder (Merrill et al. 2017; Bozzatello et al. 2016), and genetic diseases such as Gaucher's or Faber's (Mencarelli and Martinez-Martinez 2013; Rohrbough and Broadie 2005).

Despite the proven importance of these biomolecules regarding the correct functioning of neurons and brain, the current understanding of the lipid composition and organization in the neuronal plasma membranes as well as the mechanisms that regulate them in relation to the neuronal activity remains sparse.

To visualize the spatial distribution of the cellular plasma membrane lipids, many probes and detection methods have been tested; being the most spread the use of antibodies and fluorescent-labeled lipids analogs (Voelker 1990; Rheenen, van et al. 2005). The main advantage of the affinity approach is the wide range of species that can be detected and the relative simplicity of the analysis. However, among other limitations, antibodies are not able to cross the plasma membrane, meaning that only lipids with an extracellular epitope can be labeled. On top of that, the size of the probes, considering the addition of a primary and a functionalized secondary antibody, limits the number of molecules within an particular volume that can be labeled (Maidorn et al. 2019). Being even more limiting the fact that if lipids are bound to proteins, they will not be so accessible for immunolabeling (Gorman and Kraft 2020). Since it is possible to avoid these problems, fluorescent-lipids analogs have increased their popularity. Nevertheless, they are not exempt from troubles. Even though their structural resemblance, the relatively large size of the fluorophore, and the different chemical properties of the labeled compounds can disturb the natural arrangement of the lipids and their interaction with other components of the plasma membrane (Wilson et al. 2012; Devaux et al. 2008; Maier et al. 2013). To avoid the already mentioned issues, the simplest solution is to detect unmodified lipids by just using stable isotopes in combination with SIMS. Stable isotope labeled lipids are lipids that include on their structure a rare stable isotope such as  $^{15}\text{N}$ ,  $^{13}\text{C}$ ,  $^{18}\text{O}$ , or  $^2\text{H}$ . Such lipids behave exactly like their natural homologs but still, thanks to their mass difference, they can be detected by SIMS. Nonetheless, this approach also presents some limitations. The use of rare-isotopes lipids analogs constrains the experiment to particular targets, since this method only enables the simultaneous detection of a small number of lipids (Kraft 2017; He et al. 2017). Furthermore, once the

exogenous lipids are incorporated into cells or tissue, going through their physiological metabolic processes, the rare isotopes may spread across all their metabolites.

Due to the already mentioned problems, the study of the lipid composition of neuronal plasma membranes through unlabeled experiments using time of flight secondary mass spectrometry (ToF-SIMS) appears to be an optimal solution. Even if the spatial resolution of ToF-SIMS, is not as good as for other SIMS instruments (Nuñez et al. 2018), it enables the simultaneous identification and localization of a wide range of masses without the addition of exogenous lipids (Agüi-Gonzalez et al. 2019; Philipson et al. 2018). ToF-SIMS also counts with a mass range that commonly reaches up to 2000 Da, offering a very low detection limit that ranges from ppm to ppb, and a pretty high spatial resolution ( $\sim < 300$  nm) (Agüi-Gonzalez et al. 2019). Besides, this approach has been already tested for the study of lipid distribution on tissues (Philipson et al. 2018), single cells (Ren et al. 2019), and more concretely on neurons (Merrill et al. 2017; Passarelli et al. 2013).

Apart from the technical limitations, the main gap to understand the role of concrete lipids in relation to the neuronal functions is the fact that most of the available studies are based on the analysis of gross brain areas. Among other reasons, the intrinsic heterogeneity of the brain tissue and the variance of neurons and glia ratio (Christensen 2007) hinder the extrapolation of the abundance of particular lipids species to the level of single neurons. Following the protocol of Kaeck and Banker (2006), hippocampal neurons were cultured on ITO slides, keeping a physical distance between the neurons and the astrocytic monolayer, allowing the correct development of the neurons on a conductive surface while reducing the interference of glial cells during the analysis. This ensures that the results were obtained from the analysis of neuronal plasma membranes and no from a mixture of cell types. Moreover, these low-density cultured neurons are arranged in such a way that it is possible to distinguish both morphologically and biochemically different areas of the cells (Goslin 1998).

### 3.1.1 Sample preparation

To compare the results of the three preparation methods, chemical fixation, frozen hydrating, and freeze-drying, we took into account the cell morphology, the preservation of the lipids distribution, and their signal intensity in the ToF-SIMS analysis (**Figure 33**). After this comparison, we found out that the chemical fixation (4 % of glutaraldehyde followed by 0.4 % of OsO<sub>4</sub>) properly preserved the morphology of the neurons, without showing signs of lipid delocalization. Nevertheless, possibly due to the crosslinking of the molecules of the membrane caused by the fixatives, the signal obtained from higher masses ( $> 500$  Da), was considerably diminished, fading significantly the lipid signature of the neuronal plasma membranes (**Figure 33A**).

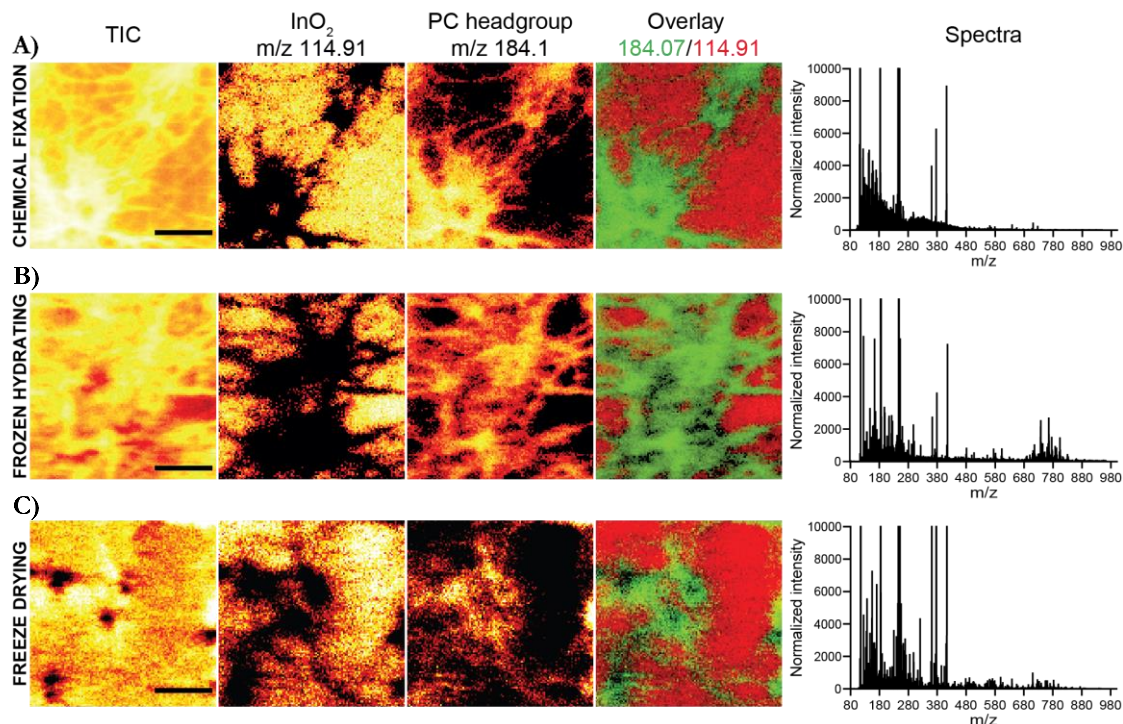


**Figure 33.** Comparison of sample preparation methods for ToF-SIMS imaging of hippocampal neurons. **A-C)** From left to right: Total Ion Count (TIC) image, ion images of InO<sub>2</sub> at m/z 114.91, PC headgroup at m/z 184.07, overlay of InO<sub>2</sub> (red) and PC headgroup (green), and spectra obtained from Chemically fixed **A)**, Frozen-hydrated **B)**, and Freeze-dried samples **C)**. Scale bars: 100  $\mu$ m. Figure extracted from Agüi-Gonzalez et al. (2021a), courtesy of the American Chemical Society.

Likewise, both frozen hydrating and freeze-drying methods (**Figure 33B and Error! Reference source not found.33C)** accurately preserved the cell morphology not showing a visible delocalization of lipids and offering stronger signal from the higher mass molecules than the chemical fixation method. Although we could observe higher high mass signals on the frozen samples, the sample handling was particularly challenging, bringing a lower reproducibility degree. Despite, freeze-drying preparation can induce certain degree of shrinkage and molecular rearrangement during the dehydration phase, this method has been widely used for biological sample analysis due to the simplicity of the preparation and its high reproducibility (Sjövall et al. 2006; Yoon and Lee 2018). Therefore, according to the good initial results and reproducibility, the freeze-drying method was applied for further experiments.

### 3.1.2 Neighborhood cross-correlation coefficients (NBCC) and independent component analysis (ICA) to uncover the lipid organization across different plasma membrane regions.

Since we aimed to separately analyze the lipid distribution on the plasma membrane of the cell body and the neurites, we had first to determine the pixels that belonged to each of these categories. In addition, we also had to distinguish the pixels corresponding to the substrate.

Thus, to provide a solid starting point that allows us to distinguish the cell body, neurites, and background; we selected three spectral datasets where the three areas were easily recognizable by just checking their total ion images. To give a preliminary assignation to each pixel, we calculated their neighborhood cross-correlation coefficients (NBCC). As expected, the highest NBCC values were localized on the cell bodies and the neurites had higher NBCC values than the pixels in the background. To achieve a more accurate assignation, a Gaussian mixture model (GMM) was applied. Then, based on the probability maps, three different



masks were applied determining the areas of the image covered by the cell bodies, the neurites, and the substrate (**Figure 34**).

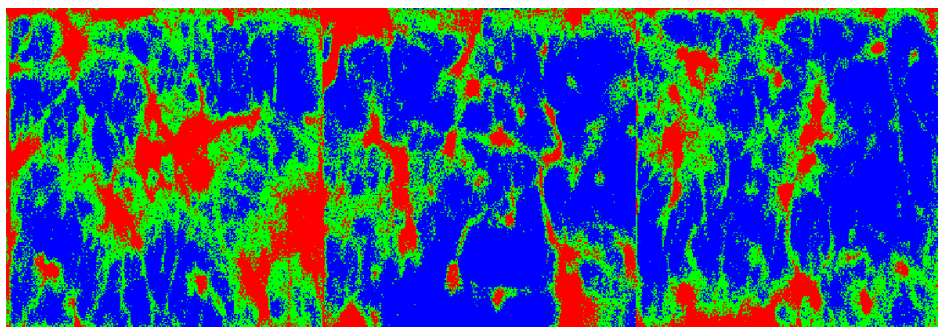


**Figure 34. Representative images of the masks after applying a Gaussian mixture model.** The different areas on three ions images assigned to the cell body (displayed in red), neurites (displayed in green), and background (displayed in blue).

Then, to determine the differences in the lipid composition between particular regions of the neuronal plasma membranes, we grouped all the pixels that belonged to one of these three categories, and an ICA was performed. The number of ICs required to ensure the coverage of more than 95 % of the total data, was calculated by previously running a principal component analysis (PCA), giving a total of 151 ICs for the positive ion mode datasets and 97 ICs for the negative ion mode. Each of these independent components (ICs) comprehend a group of masses, which showed some relationship regarding their spatial distribution. The co-localization of masses across the pixels of our images could be caused by two main reasons. First, with SIMS we detect the characteristic fragments of a concrete molecule. Second, some independent chemical species have the tendency of staying close to each other. Thus, ICA would be a useful tool to observe the typical fragments obtained from particular chemical species as well as to uncover the relation between different lipid species.

By the combination of all the ICs that we obtained within each of the three categories, the rest of the data ( $n = 9$ ) was unmixed and their corresponding images were used to further refinement of the masks that we applied (**Figure 35**).

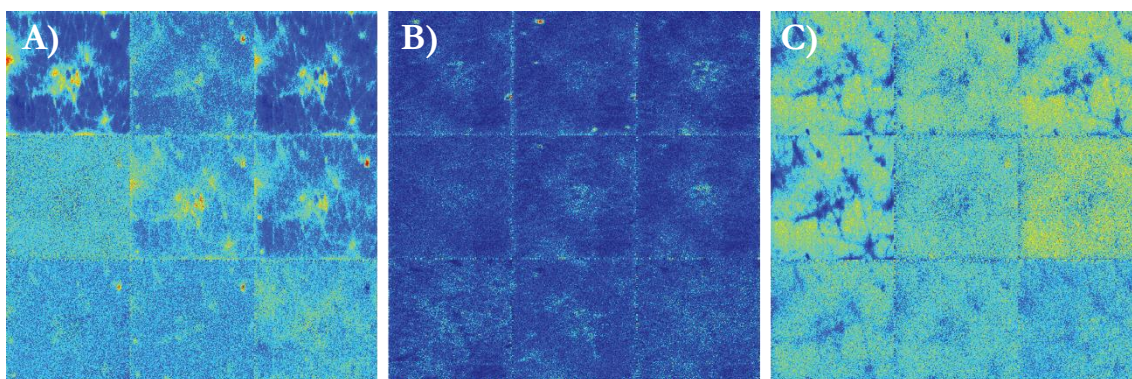


**Figure 35. Representative example of the first 9 ICs of each category.** **A)** First 9 ICs of the cell body, **B)** first 9 ICs of the neurites, and **C)** first 9 ICs of the background.

The results of this processing prove that there are clear differences between the molecular composition of the cell bodies and the neurite on the plasma membrane of hippocampal neurons. Even in the cases of masses or ICs that were present in both areas, the abundances on each region were different (**Figure 35**). Likewise, it was clear that the distribution and composition of ICs on the cell body and neurites were unequivocally different from those

related to the background. Yet, there are few cases where the neurites and the background shared some regions and masses. Despite the good lateral resolution achieved by the J105, the focus size of the primary ion beam is still limited. This together with the thinness of the neurites and the overlapping between these two categories can explain the co-ionization and detection of ions that would be simultaneously emitted and detected from both the substrate and the neurites.

In future studies, the incorporation of SIMS-compatible probes to label specific proteins of interest such as the Au-anti-vGlut-nanobody (**Figure 36**) could determine with precision the nature of the neurites of the cells, as well as the identity of the neurons themselves (e. g. glutamatergic, GABAergic), as demonstrated in (Agüi-Gonzalez et al. 2021b). This type of analysis would assist the verification of the ICA results.

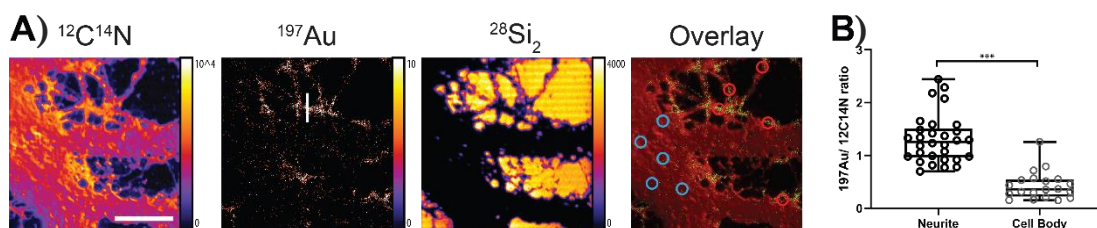


**Figure 36. NanoSIMS imaging of vGlut in rat hippocampal neurons employing Au anti-vGlut1 nanobody.** **A)** NanoSIMS images of hippocampal neurons including cell body and neurites. From left to right: ion images of  $^{12}\text{C}^{14}\text{N}$ ,  $^{197}\text{Au}$ ,  $^{28}\text{Si}_2$ , and overlay of  $^{197}\text{Au}$  (green) and  $^{12}\text{C}^{14}\text{N}$  (red). On the overlay image, representative ROIs were selected on the cell body (blue circles) and the neurite areas (red circles). Scale bar: 10  $\mu\text{m}$ . **B)** Plot of the normalized Au signal intensity ( $^{197}\text{Au}/^{12}\text{C}^{14}\text{N}$ ) to compare labeling levels between the neurites and the cell body. Confirmed by a Kolmogorov-Smirnov test ( $P < 0.0001$ ) we detected higher Au labeling in the neurites compared to the cell body ( $n = 30$  for neurites,  $n = 20$  for cell bodies). Figure adapted from Agüi-Gonzalez et al. (2021b), courtesy of MDPI.

### 3.1.3 Independent components content

Analyzing the mass peak composition of individual ICs, we obtained further details about the lipid species and fragments that distributed differently between the neurites and the cell body. For example, in the positive mode, when checking the second IC with more weight within the cell body (**Table 1, IC Index No.37**), we observed several peaks that are possibly related to each other. The peaks at  $m/z$  184.07 and 224.10, identified respectively as  $\text{C}_5\text{H}_{15}\text{NO}_4\text{P}$  and  $\text{C}_8\text{H}_{19}\text{NO}_4\text{P}$ , are commonly described as PC fragments. In the same line, the peak at  $m/z$  440.28 can be a fragment of PCs or PE with a fatty acid tail of C12:0 for the PCs and C15:0 for PEs. Withal, the peak at  $m/z$  478.35 could also be a fragment of PCs or PEs respectively containing a fatty acid tail of C16:0 or C19:0. This shows that a single IC contains the signature fragments of certain PCs and PEs, which possibly present certain structural and functional relationship at the plasma membrane of the cell body. Furthermore, also in the ion positive mode, the mass peaks found in the third IC of the neurites area (**Table 1, IC Index No. 3**); a PC fragment at  $m/z$  86.10,  $\text{PA}(15:0) + \text{Na}^+$  at  $m/z$  433.23,  $\text{DG}(34:1)$  at  $m/z$  577.54, and sphingomyelin  $\text{SM}(37:1)$  and  $\text{SM}(44:1)$  at  $m/z$  562.58 and 660.64 respectively, show the spatial relation between fragments belonging to different lipid groups. Likewise, in the negative ion mode, the sixth IC of the neurites (**Table 1, IC Index No.6**), possibly reveals the connection between fatty acids like  $\text{FA}(14:0)$ ,  $\text{FA}(16:0)$ ,  $\text{FA}(18:2)$ ,  $\text{FA}(18:1)$ ,  $\text{FA}(18:0)$ ,  $\text{FA}(20:0)$ , respectively found at  $m/z$  227.24, 255.22, 279.23, 281.28, 283.23, 311.30, and triacylglycerols,  $\text{TG}(50:0)$  and  $\text{TG}(52:0)$  found at  $m/z$  833.79 and 861.81. Those fatty acids may not just tend to appear close to TGs but could actually be fragments of them. ICA, therefore, may be a useful tool to clarify the possible relationships of particular subgroups of lipids and their fragments.

**Table 1. Peak composition of the main ICs at the plasma membrane of the cell body and neurites.**

Positive SIMS mode											
Neurites											
IC 2	86.10	508.69	554.67	166.10	636.59	512.69					
IC 3	298.08	86.10	433.23	378.47	577.54	562.58	496.36	660.64			
IC 4	378.47	710.60	418.55	432.40	512.41	470.51	654.58				
IC 5	86.10	478.35	528.70	510.74	142.04	496.36					
IC 6	508.69	507.67	427.18	184.07	530.70	496.36					
IC 7	440.28	582.78	636.59	385.34	124.04						
IC 9	86.10	622.61	561.74	492.39	504.82	580.81	456.82				
IC 10	86.10	508.69	510.74	428.43	511.66						
IC 11	462.75	514.74	478.35	496.36	124.04						
Cell Body											
IC 36	184.07	86.10	433.23	577.54							
IC 37	440.28	184.07	337.25	224.10	649.62	478.35					
IC 39	86.10	509.61	166.04								
IC 40	414.81	732.58									
IC 41	124.04	654.65	552.50	492.39	142.04	385.34	184.07	446.31	606.66		
IC 43	404.80	184.07	508.69	339.27	367.31	580.63					
Negative SIMS mode											
Neurites											
IC 1	223.06	140.05	340.39								
IC 2	241.10	408.32	523.49	199.20							
IC 3	452.45	534.68	394.02	496.37	126.06						
IC 5	199.20	255.22	313.14	460.39	277.24						
IC 6	283.00	255.22	311.30	256.27	861.81	833.79	227.22	325.38	408.32	279.23	281.28
IC 7	180.08	299.02	126.06	406.45	241.07	227.22	444.38	126.06			
IC 8	166.10	313.06	320.17	507.67	255.22	337.25	446.20	502.88	470.51		
IC 9	241.10	227.22	283.23	303.27	140.05	301.14	464.30	255.40	180.08	413.38	
IC 10	241.10	140.05	277.24	460.39	544.37						
Cell Body											
IC 49	281.28	241.03	316.04								

Table adapted from Agüi-Gonzalez et al. (2021a), courtesy of the American Chemical Society.

### 3.1.4 Study of the neuronal membrane lipid composition after drug treatment by cross-correlation coefficient difference analysis.

To study how the changes on the neuronal activity can affect the lipid organization of the plasma membranes of the hippocampal neurons, we induced opposite effects by treating our cells with two types of drugs, Tetrodotoxin (TTX) and Bicuculline (BIC). We separated our batch of samples in three treatment groups TTX, BIC and control. To prepare the control group, one third of the samples was handled in the exact same manner than the treated samples (TTX and BIC), but no drugs were applied on them. Moreover, to ensure the reproducibility of our experiments and obtain robust statistical results, we worked with at least nine independent samples within each treatment group, which were split and treated at three different time points (total  $n = \geq 27$ ).

The first group ( $n = 9$ ) was treated for 72 hours with tetrodotoxin (TTX), a strong neurotoxin that blocks the firing action potential of the neurons by binding to the voltage-gated sodium channels and blocking the passage of sodium (Lago et al. 2015). The second group ( $n = 9$ ) was incubated with a competitive antagonist of GABA-A receptors, bicuculline (BIC), that

enhances the neuronal activity (Johnston 2013). The third group (n = 9) was treated with no drug but incubated during those 72 hours in regular culture medium. Except from this fact, the three groups we handled in the exact same manner.

Once the experimental part concluded, we analyzed the differences on the molecular composition of the neuronal plasma membranes between treatment groups by applying CCD analysis. This analytic method compares individually pairs of spectra before and after removing single peak, determining the contribution magnitude of that concrete peak over the difference between these two spectra. If the peak is removed and the spectra gets more similar, the CCD value increases positively, meaning that this particular peak is causing a difference between the two spectra. On the contrary, if the spectra increase their differences when the peak is removed, the CCD value decreases, meaning that it was bringing similarity to the compared spectra (**Figure 37A**). Thus, the bigger the CCD, the higher is the contribution of a concrete mass peak to the difference between the spectra.

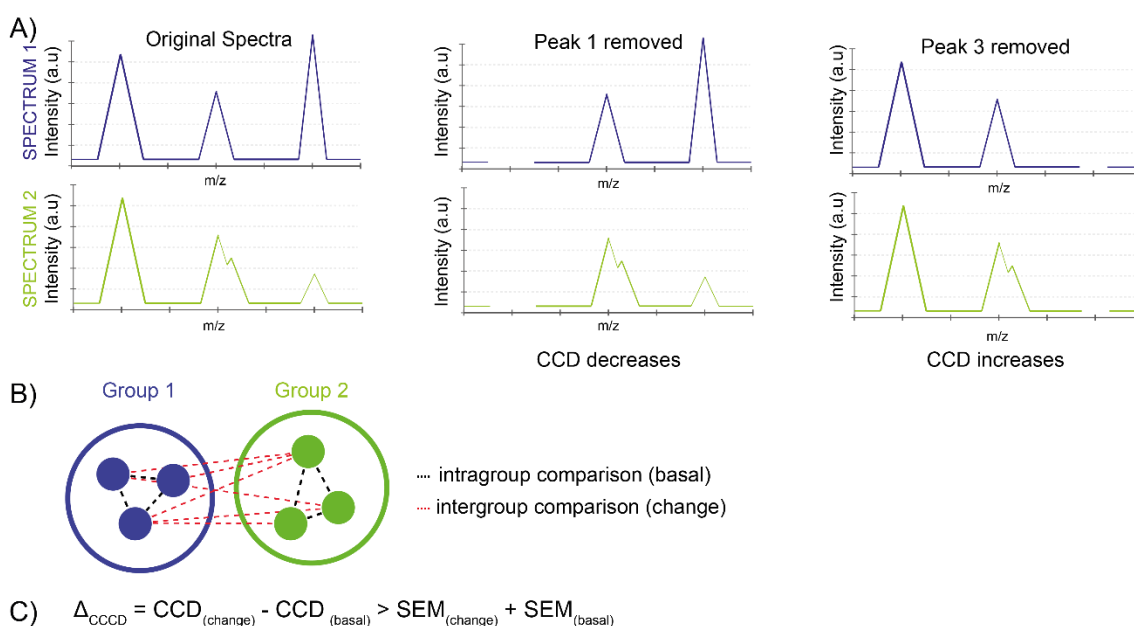


**Figure 37. Cross-correlation coefficient differences analysis. A)** To carry the CCD analysis, each pair of spectra is compared when including and excluding a particular mass peak. With this, the contribution of that specific peak to the spectral differences is calculated. In this example, the CCD of the pair decreases when peak 1 is excluded and increases when peak 3 is excluded. **B)** To determine the mass peaks that contribute to the differences between treatment groups, the comparison of the CCD is calculated within samples of the same group (basal) and between treatment and control samples (change). **C)** The mass peaks are considered as significant only when the criterion on C is applicable. Figure extracted from Agüi-Gonzalez et al. (2021a), courtesy of the American Chemical Society.

To carry out this analysis, first, we obtained the intragroup CCDs for all mass peaks by combining all possible pairs of spectra within a particular treatment group. In this manner, we defined the intragroup degree of difference that was termed as *basal* (**Figure 37B**). Then, we obtained the intergroup CCDs by comparing each spectrum from the control group with each one of the treated samples, naming this difference as a *change* (**Figure 37B**). Afterwards, for each mass peak, the CCD mean of all the pairs and its standard deviation of the mean (SEM) were calculated. Then, we only considered as significant the peaks where the difference between the change CCD and the basal CCD was bigger than the sum of their SEMs (**Figure 37C**), which corresponds to a sigma difference and a confidence interval  $> 0.681$ . This analysis was separately done for the cell body and neurites identified on the images, and separately for the positive and negative ion mode spectra.

By analyzing our data through a CCD analysis, we ensured a more reliable comparison than the one offered by most commonly used statistical test. The main advantage of the CCD, regarding SIMS spectra analysis, is that this method does not depend on the normalization of the data, which would often add a certain bias, affecting more drastically to peaks with low amplitude. In this manner, we compared the variations caused by the drug treatments over each peak of the spectra, circumventing the distortion of the data caused by its normalization, preserving the independence from the signal amplitudes by only taking into account the shape of spectra (**Figure 37A**). Unlike other comparison methods such as the t-test, which simplifies the differences between two spectra to the comparison of individual or a particular group of peaks but neglecting the rest of the data, the CCD analysis compares two entire spectra when only one peak is missing. Thus, CCD can analyze the information where most of the signals and noises are represented. Particularly, CCD analysis provides the balanced level of total noise of the entire spectra, which is typically not easy to normalize.

### **3.1.5 Drug treatments induce particular lipids subclasses changes on hippocampal neuronal plasma membranes.**

Once the CCD values and their significance were obtained for all the peaks in both positive and negative modes as well as for the two analyzed areas of the cell, cell body and neurites, we proceeded with the identification of the significant peaks. To define reliable tentative assignments, we set a threshold of 100 ppm for the maximum mass difference between the detected masses and the theoretical masses found in the literature or databases. A total of 74 significant peaks were assigned to a particular lipid species or fragment, with a smaller delta mass ( $< 100$  ppm), from which 38 peaks were detected in positive mode and 36 peaks in negative mode (**Table 2**).

Table 2. Tentative peak assignment in positive and negative SIMS mode.

<b>Positive SIMS mode</b>				
<b>Tentative Assignment</b>	<b>Molecular Formula</b>	<b>Detected mass</b>	<b>Theoretical mass</b>	<b>Delta</b>
<b>Ceramides</b>				
Cer(36:1;O2)	C36H72NO3	566.59	566.55	68.50
Cer(36:1;O3)	C36H72NO4	582.59	582.55	70.20
Cer(36:0;O3)+Na	C36H73NO4Na	606.55	606.54	2.14
CerP(d34:1)+Na	C34H68NO6PNa	640.47	640.47	9.10
CerP(34:0;O2)+K	C34H70NO6PK	658.49	658.46	42.89
GalCer(32:1)+K	C38H73NO8K	710.51	710.50	10.84
<b>Phosphatidic Acid</b>				
PA(12:0)+K	C15H31O7PK	393.16	393.14	31.95
PA(36:2)+Na	C39H73O8PNa	723.48	723.49	22.18
PA(39:1)+K	C42H81O8PK	783.54	783.53	12.02
PA(41:2)+K	C44H83O8PK	809.56	809.55	15.77
PA(44:8)+Na	C47H77O8PNa	823.53	823.53	8.08
<b>Phosphatidylcholine</b>				
PC fragment	C5H13PNO3	166.06	166.06	0.41
PC head group	C5H15PNO4	184.07	184.07	0.73
PC fragment	C8H19NPO4	224.12	224.11	43.89
PC(28:2)	C36H70NO8P	674.49	674.48	16.23
PC(28:1)	C36H72NO8P	676.49	676.49	3.39
PC(30:0)	C38 H76 N O8 P	706.51	706.53	28.31
PC(32:1)+Na	C40H78NO8PNa	754.52	754.54	20.21
PC(34:2)+Na	C42H80NO8PNa	780.58	780.55	36
PC(34:1)+Na	C42H82NO8PNa	782.58	782.57	18.48
<b>Phosphatidylglycerol</b>				
PG(28:0;O)+Na	C34H69O9PNa	675.47	675.46	16.78
PG(25:1;O)+K	C31H59O11PK	677.34	677.34	4.71
PG(31:1;O)	C37H74O9P	693.5	693.51	8.68
PG(30:0)	C36H72O10P	695.46	695.49	32.04
PG(41:6)	C47H81O10PK	875.54	875.52	22.37
<b>Phosphatidylserine</b>				
PS(36:6)+K	C42H70NO10PK	818.46	818.44	27.59
PS(40:6)+K	C46H78NO10PK	874.5	874.5	0.02
PS(43:6)+Na	C49H84NO10PNa	900.55	900.57	22.23
<b>Diacylglycerol</b>				
DG(31:3)+Na	C34H60O5Na	571.44	571.43	12.56
DG(33:3)	C36H65O5	577.5	577.48	23.94
DG(35:6)	C38H63O5	599.47	599.47	4.13
DG(37:7)	C40H65O5	625.48	625.48	0.28
DG(37:6)	C40H67O5	627.51	627.5	22.59
DG(40:1)	C43H83O5	679.64	679.62	23.52
DG(43:6)+K	C46H78O5K	749.55	749.55	1.87

**Negative SIMS mode**

<b>Tentative Assingment</b>	<b>Molecular Formula</b>	<b>Detected mass</b>	<b>Theoretical mass</b>	<b>Delta</b>
<b>Ceramides</b>				
Cer(36:1)	C36H70NO3	564.56	564.54	40.85
Cer(38:1;O)	C38H74NO2	576.58	576.57	17.51
Cer(36:0;O3)	C36H72NO4	582.56	582.55	31.4
Cer(39:2;O2)	C39H74NO3	604.57	604.57	1.57
Cer(40:1;O2)	C40H78NO3	620.57	620.6	49.84
GlcCer(36:2;O2)	C42H78NO8	724.56	724.57	15.57
<b>Fatty Acids</b>				
FA(16:1)	C16H29O2	253.21	253.22	7.71
FA(20:5)	C20H31O2	303.22	303.23	33.02
FA(38:3)	C38H69O2	557.55	557.53	30.75
<b>Phosphatidic Acid</b>				
PA(34:4;O)	C37H66O7P	653.51	653.45	90.62
PA(34:3;O)	C37H68O7P	655.49	655.47	27.23
PA (34:0;O)	C37H74O7P	661.52	661.52	5.28
PA(35:3;O)	C38H70O7P	669.49	669.49	3.2
PA(35:2)	C38H70O8P	685.5	685.48	28.38
PA(36:1)	C39H74O8P	701.53	701.51	24.49
PA(36:0)	C39H76O8P	703.54	703.53	20.12
PA(38:5;O)	C41H72O7P	707.52	707.5	23.8
PA(38:3;O)	C41H76O7P	711.54	711.53	5.23
PA(38:5)	C41H70O8P	721.49	721.48	17.1
PA(38:4)	C41H72O8P	723.51	723.5	22.88
PA(39:1)	C42H76O8P	739.52	739.53	10.69
PA(39:2)	C42H78O8P	741.54	741.54	5.46
<b>Phosphatidylethanolamine</b>				
PE-Cer(32:1;O2)	C34H68N2O6P	631.52	631.48	64.49
<b>Phosphatidylinositol</b>				
PI-Cer(46:0;O3)	C52H103NO12P	964.7	964.72	24.46
<b>Phosphatidylserine</b>				
PS(39:2)	C45H83NO10P	828.55	828.58	36.63
PS(43:4)	C49H88NO10P	880.61	880.61	7.12
<b>Triacylglycerol</b>				
TG(37:1)	C40H73O6	649.54	649.54	5.07
TG(37:0)	C40H75O6	651.54	651.56	30.49
TG(53:8)	C56H91O6	859.64	859.68	44.19
TG(53:7)	C56H93O6	861.71	861.7	10.35
TG(53:6)	C56H95O6	863.71	863.71	2.64
TG(54:3)	C57H103O6	883.78	883.78	3.73
TG(54:2)	C57H105O6	885.79	885.79	2.27
TG(54:1)	C57H107O6	887.8	887.81	12.01
TG(55:7)	C58H97O6	889.7	889.73	27.57
TG(60:11)	C63H99O6	951.72	951.74	26.69

Table adapted from Agüi-Gonzalez et al. (2021a), courtesy of the American Chemical Society.

From 552 peaks that showed to be significant in the comparison between the control and the TTX groups, we could tentatively identify 51 lipid species or fragments. From the positive ion mode analysis, 14 identified peaks were significant on the cell body area (**Figure A1**) and 16 peaks on the neurite area (**Figure A2**). On the negative ion mode, 24 significant peaks were assigned on the cell body (**Figure A3**) and 16 significant peaks from the neurite area (**Figure A4**).

On the other hand, from the total of 277 peaks that showed to be significant in the comparison between the control and the BIC treated groups, we could tentatively identify 41 lipid species or fragments. In the positive ion mode, 20 significant peaks were identified on the cell body area (**Figure A5**) and 8 peaks on the neurite area (**Figure A6**) of the neuronal plasma membranes when comparing the control with the group of cells treated with BIC. On the negative mode, 16 significant peaks were assigned on the cell body (**Figure A7**) and 8 peaks on the neurite area (**Figure A8**).

These results showed that after treatments with drugs that induced opposite effects on the neuronal activity, TTX and BIC, significant modifications appeared on the lipids that constitute the plasma membranes on hippocampal neurons, proving that it may exist a relevant connection between the membrane lipid distribution and the neuronal activity. All peaks identified as lipid species that were significantly affected by any of the drug treatments, in positive and negative ion mode are summarized in (**Table 3**).



Table 3. Lipids and fragments significantly affected after drug treatments.

Compound	$\Delta$ CCD	SEM(change+basal)	Compound	$\Delta$ CCD	SEM(change+basal)
<b>Positive_TTX_Cell Body</b>			<b>Positive_BIC_Cell Body</b>		
AA Phe	4,71E-08	7,55E-09	AA Phe	3,45E-08	6,12E-09
AA Trp	1,92E-07	3,69E-08	AA Trp	1,61E-07	3,28E-08
PC fragment 166	1,24E-07	1,92E-08	PC fragment 166	1,75E-07	2,21E-08
PC fragment 184	2,22E-05	6,27E-06	PC fragment 184	3,38E-05	6,82E-06
PC fragment 224	1,60E-08	2,98E-09	PC fragment 224	3,93E-08	4,44E-09
PA(12:0)+K	3,33E-09	5,63E-10	DG (31:3)+Na	1,72E-09	6,57E-10
Cer (36:1)	1,67E-08	2,07E-09	DG (33:3)	1,79E-09	6,62E-10
DG (34:1)+H-OH	1,89E-09	6,74E-10	DG (35:6)	3,65E-09	8,26E-10
Cer (36:1,O <sub>3</sub> )	3,28E-09	6,99E-10	DG (37:7)	7,39E-05	1,94E-05
Cer (36:0,O <sub>3</sub> )+Na	8,26E-09	1,46E-09	DG (37:6)	5,61E-05	1,02E-05
CerP (34:0,O <sub>2</sub> )+K	5,36E-04	7,55E-05	PG (30:1)	1,48E-05	4,23E-06
PC (28:2)	4,98E-05	9,81E-06	PG (30:0)	1,08E-04	4,23E-05
PG (28:0,O)+Na	2,17E-05	7,51E-06	PC (30:0)	7,69E-05	1,63E-05
PC (28:1)	2,04E-04	3,42E-05	PA (36:2)+Na	1,52E-04	3,07E-05
DG (40:1)	5,81E-05	1,13E-05	DG (43:6)+K	1,34E-05	4,45E-06
GalCer (32:1)+K	1,40E-02	1,56E-03	PC (32:1)+Na	3,61E-04	8,60E-05
<b>Positive_TTX_Neurites</b>			<b>Positive_BIC_Neurites</b>		
AA Phe	8,29E-09	2,15E-09	PC (34:2)+Na	3,68E-05	1,32E-05
PC fragment 184	3,45E-06	1,24E-06	PC (34:1)+Na	3,70E-04	9,23E-05
PC fragment 224	4,34E-09	1,57E-09	PA (39:1)+K	1,11E-04	2,11E-05
PA (12:0)+K	1,92E-09	4,25E-10	PA (41:2)+K	1,14E-05	3,66E-06
Cer (36:1)	1,02E-08	1,34E-09	PS (36:6)+K	1,52E-05	3,83E-06
Cer (36:1,O <sub>3</sub> )	1,75E-09	5,20E-10	PS (40:6)+K	6,19E-05	1,97E-05
Cer (36:0,O <sub>3</sub> )+Na	3,86E-09	9,66E-10	DG (37:7)	2,42E-05	5,43E-06
CerP(d34:1)+Na	5,34E-03	9,89E-04	DG (37:6)	8,72E-06	3,58E-06
CerP (34:0,O <sub>2</sub> )+K	3,69E-04	5,49E-05	PG (30:0)	5,95E-05	2,06E-05
PC (28:2)	1,80E-05	7,12E-06	PA (36:2)+Na	6,76E-05	1,98E-05
PG (28:0,O)+Na	2,24E-05	3,41E-06	PC (34:1)+Na	1,77E-04	4,73E-05
PC (28:1)	1,33E-04	1,88E-05	PA (39:1)+K	4,99E-05	9,86E-06
PG (25:1,O)+K	2,49E-05	5,10E-06	PS (40:6)+K	5,52E-05	1,17E-05
DG (40:1)	3,48E-05	6,29E-06	PS (41:6)	9,74E-06	3,10E-06
GalCer (32:1)+K	1,59E-02	1,76E-03			
PA (44:8)+Na	4,78E-05	1,13E-05			
PS (43:6)+Na	4,36E-05	1,10E-05			
Compound	$\Delta$ CCD	SEM(change+basal)	Compound	$\Delta$ CCD	SEM(change+basal)
<b>Negative_TTX_Cell Body</b>			<b>Negative_BIC_Cell Body</b>		
FA (38:3)	2,95E-07	9,46E-08	ST (C18-OH)	3,35E-05	1,18E-05
Cer (36:1)	1,38E-07	7,95E-08	PS (39:2)	3,33E-05	1,48E-05
Cer (38:1,O)	1,88E-07	9,70E-08	TG (53:6)	2,12E-05	5,12E-06
Cer (36:0,O <sub>3</sub> )	1,65E-07	8,99E-08	PS (43:4)	3,53E-05	1,13E-05
Cer (39:2,O <sub>2</sub> )	1,73E-07	9,54E-08	TG (54:2)	4,97E-04	2,00E-04
TG (37:0)	1,54E-05	4,27E-06	TG (54:1)	2,78E-04	4,92E-05
PA (34:4,O)	8,38E-06	1,99E-06	PI-Cer(46:0,O <sub>3</sub> )	6,21E-05	1,21E-05
PA (34:3,O)	2,65E-05	5,17E-06	<b>Negative_BIC_Cell Body</b>		
PA (34:0,O)	1,17E-05	3,63E-06	FA (16:1)	5,89E-06	2,52E-06
PA (35:3,O)	1,37E-05	4,67E-06	FA (20:5)	3,63E-06	1,03E-06
PA (35:2)	1,46E-05	5,38E-06	PE-Cer (32:1,O <sub>2</sub> )	7,51E-06	2,87E-06
PA (36:0)	7,90E-06	2,82E-06	TG (37:1)	1,17E-05	3,40E-06
PA (38:5,O)	1,50E-05	4,37E-06	PA (34:4,O)	7,37E-06	2,47E-06
PA (O-38:3)	1,63E-05	6,02E-06	PA (34:3,O)	1,03E-05	4,16E-06
PA (38:4)	2,30E-05	1,00E-05	PA (34:0,O)	9,73E-06	3,23E-06
GlcCer(36:2,O <sub>2</sub> )	2,87E-05	8,98E-06	PA (38:5)	1,23E-05	2,96E-06
TG (53:7)	7,26E-05	2,27E-05	PA (38:4)	6,16E-05	1,55E-05
PS (43:4)	3,46E-05	1,05E-05	TG (53:8)	3,23E-05	1,12E-05
TG (54:2)	6,01E-04	1,34E-04	TG (53:7)	1,12E-04	3,24E-05
TG (54:1)	2,58E-04	4,37E-05	TG (53:6)	2,99E-05	1,12E-05
TG (55:7)	3,12E-05	6,16E-06	TG (54:3)	1,10E-04	3,04E-05
TG (60:11)	5,84E-06	1,65E-06	TG (54:2)	2,11E-03	3,81E-04
PI-Cer(46:0,O <sub>3</sub> )	7,99E-05	1,80E-05	TG (54:1)	4,26E-04	6,95E-05
<b>Negative_TTX_Neurites</b>			TG (55:7)	4,58E-05	6,40E-06
FA (38:3)	2,69E-07	7,74E-08	<b>Negative_BIC_Neurites</b>		
Cer (36:1)	1,14E-07	6,63E-08	FA (16:1)	2,47E-06	9,38E-07
Cer (38:1,O)	1,24E-07	5,62E-08	FA (20:5)	1,51E-06	2,87E-07
Cer (36:0,O <sub>3</sub> )	1,11E-07	5,97E-08	FA (38:3)	9,65E-08	5,76E-08
Cer (40:1,O <sub>2</sub> )	1,01E-04	3,56E-05	TG (53:7)	4,52E-05	2,27E-05
TG (37:0)	1,10E-05	4,46E-06	TG (53:6)	2,28E-05	4,64E-06
PA (35:2)	5,75E-06	2,09E-06	TG (54:2)	1,11E-03	2,58E-04
GlcCer(36:2,O <sub>2</sub> )	2,05E-05	7,48E-06	TG (54:1)	2,30E-04	4,12E-05
PA (39:1)	1,04E-05	3,74E-06	PI-Cer (46:0,O <sub>3</sub> )	5,08E-05	1,08E-05

Lists of the tentatively identified lipid mass peaks and fragments that showed to be significantly affected by different drug treatments after the CCD analysis. The lipids are sorted by drug treatment, cell area and SIMS ion mode. Table adapted from Agüi-Gonzalez et al. (2021a), courtesy of the American Chemical Society.

### 3.1.6 Lipid distribution of hippocampal neuronal plasma membranes and its link to homeostatic plasticity.

The long incubations with TTX and BIC (72 h) were not expected to only modify acutely the activity of the hippocampal neurons but to further induce homeostatic plasticity modifications on them (Turrigiano et al. 1998). Thus, the changes that we observed in the lipid composition of the plasma membranes after these long incubations suggest that lipids may be part of the molecular mechanisms that contribute to homeostatic plasticity processes in hippocampal neurons.

Once we identified individual lipid species that were affected by this homeostatic process (Table 3), we wanted to go one level further, analyzing the relative abundance changes within particular lipid subcategories. These compositional changes were again analyzed dividing the neuronal plasma membrane into two areas, cell body, and neurites.

Only lipid subclasses that counted with a minimum of 3 assigned mass peaks ( $n \geq 3$ ) were included in our analysis. The included lipid subclasses were, Cer ( $n = 12$ ), FAs ( $n = 3$ ), PAs ( $n = 18$ ), PCs ( $n = 9$ ), PGs ( $n = 5$ ), PSs ( $n = 5$ ), and TGs ( $n = 11$ ). Lipid subcategories such as PEs or PIs were excluded due to the insufficient number of identified peaks.

First, we compared the average intensity of individual mass peaks between the treatments and control groups, determining if their intensity increased or decreased under a particular treatment, in both cell regions. Then we calculated the percentage of lipids within a concrete subclass that changed following the same trend (Table 4) (e. g. 83 % of the total of ceramides increased their presence in neurites and cell body in the cells treated with TTX).

**Table 4. Relative changes of lipid subclasses in the plasma membrane of hippocampal neurons after their incubation with TTX and BIC.**

LIPID SUBCLAS	TTX				LIPID SUBCLAS	BIC			
	Body ↑	Body ↓	Neur ↑	Neur ↓		Body ↑	Body ↓	Neur ↑	Neur ↓
Cer	83%	0%	83%	8%	Cer	0%	0%	0%	0%
FA	33%	0%	33%	0%	FA	67%	0%	100%	0%
PA	67%	0%	22%	0%	PA	44%	0%	11%	0%
PC	22%	33%	44%	0%	PC	33%	44%	11%	0%
PG	20%	0%	40%	0%	PG	40%	0%	40%	0%
PS	0%	20%	0%	60%	PS	40%	0%	20%	0%
TG	60%	0%	40%	0%	TG	80%	0%	40%	0%

The percentages represent the relative number of lipid compounds that were affected by the drug treatments following a particular trend. The arrows, ↑ and ↓, respectively indicate when the abundance of a lipid subclass was enhanced or decreased under drug treatments in comparison with its abundance in the control samples. These relative changes were separately analyzed in the two cell areas, cell body and neurites. Table adapted from Agüi-Gonzalez et al. (2021a), courtesy of the American Chemical Society..

From this analysis, we obtained two general conclusions, first, the variation patterns were certainly different from a random distribution, supporting that variations on the synaptic activity can induce changes on the lipid composition of the neuronal plasma membranes. Second, the analysis showed that diverse lipid subclasses were influenced in a particular manner by the drug treatments and that in most of these variations were different between the cell body and the neurites.

Furthermore, we noticed particular features for individual lipid subclasses (Figure 38). For ceramides, we found out that their abundance was highly increased in both areas, the cell body, and neurite when the neuronal activity was chronically inhibited by TTX. On the

contrary, none of the lipids from this lipid subclass was significantly modified when the neuronal activity was promoted by the incubation with BIC. Some FAs enhanced their presence in both areas, especially with BIC treatment, but no FA showed to decrease its abundance under any treatment. Likewise, no PA decreased its abundance under any treatments, but the relative abundance of many PAs was increased, especially by TTX. In the case of PCs, we observed that the relative changes were quite heterogeneous. With both drugs, the relative abundance of several species decreased in the cell body (33 % with TTX and 44 % with BIC) but some species also increased their abundance with TTX (22 %) and BIC (33 %) incubations. Yet, on the neurites, PCs were only enhanced by both drugs. PGs, as well as TGs, showed a clear trend to enhance their abundance in both areas and under both treatments, however, no lipid species from these categories decreased under any analyzed condition or area. On the contrary, PSs abundance showed an obvious reduction when the neurons were silenced by TTX while its relative abundance only increased when the cells were stimulated with BIC.

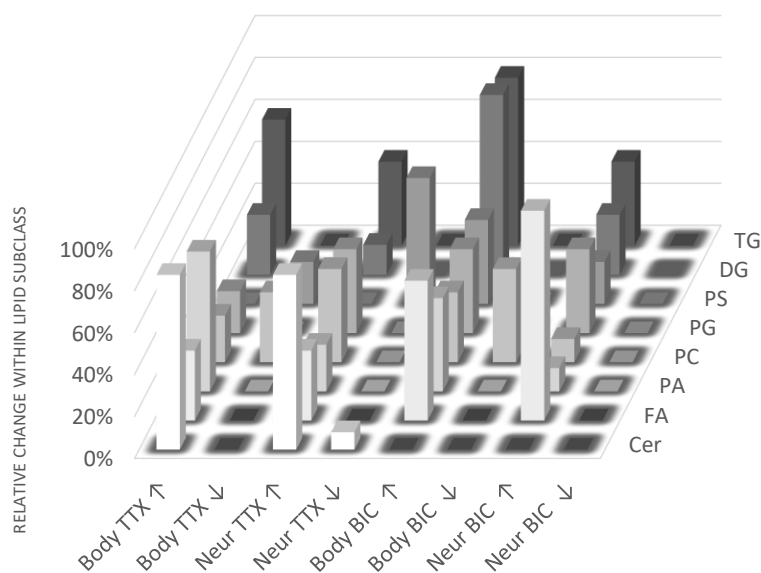


**Figure 38. 3D representation of the relative change trends of different membrane lipid subclasses following TTX or BIC treatments.** Lipid subclasses are distributed across the Y-axis. Their trends (increase  $\nearrow$  or decrease  $\searrow$ ) within the analyzed cell areas (cell body or neurites) and treatments (TTX or BIC) are displayed in the X-axis. The relative number of lipid species within a particular subclass that showed the same trend are indicated as percentages in the Z-axis. Figure adapted from Agüi-Gonzalez et al. (2021a), courtesy of the American Chemical Society.

Furthermore, to determine if there were statistically significant correlations between particular subclasses and the neuronal activity in the analyzed cellular regions, we run Kruskal–Wallis tests in combination to a Tukey–Kramer post-hoc, applying a corrected alpha value of 0.05. Due to the low number of peaks that we could identify, some observed trends could not be statistically confirmed. However, we could prove that several lipid categories had statistically significant trends in relation with the neuronal activity modulation.

Among those categories, after the treatment of the neurons with TTX, ceramides exhibited a significant enriched presence in both, the cell body and neurites. Despite the concentration of PAs was augmented in both areas and under the two drug treatments, their presence on the cells incubated with TTX was significantly higher on the cell body (~ 45 % more respect to the neurites).

Besides conforming the main building blocks in the sphingolipid pathway, ceramides represent by themselves a major type of secondary messengers in the brain (Spiegel and Milstien 1995). Previous studies also showed that ceramides modify their distribution across cellular membranes, being involved in the activation of target proteins, and signal molecules clustering. The concentration of ceramides in the cellular plasma membranes varies within a narrow range, presenting in comparison to other lipid classes a relative low concentration ( $\leq 4$  mol %) (Silva et al. 2007). Thus, small variations on its concentrations can strongly influence the structure and dynamics of the plasma membranes (Mencarelli and Martinez-Martinez 2013; Blitterswijk et al. 2003; Cremesti et al. 2002). An increase on the ceramide concentration has been directly related to an enhancement of action potentials and excitability in capsaicin-sensitive neurons (Zhang, Y. H. et al. 2002). In concordance with previous findings, our results showed that the chronic inhibition of hippocampal neurons by a long exposition to TTX triggers a dramatic increase of the membrane ceramides as part of the mechanism to overcome this inhibition. Contrastingly, the chronic enhancement of the neuronal activity by the incubation with BIC does not induce the accumulation of any of the identified ceramide species (**Table 4**).

On the other hand, PSs, the main anionic phospholipids in the inner leaflet of the plasma membrane, have already been associated with important signaling pathways in relation to membrane fusion and exocytosis (Kim, H.-Y. et al. 2014; Baudry et al. 1991; Murray et al. 2004). Due to its negative charge, PS is known to have a strong interaction with the GABA cationic species and it seems to be implicated in the internalization of this inhibitory neurotransmitter (Rolandi et al. 1990). Previous studies showed that the PS-GABA interaction is required to induce the effect of this neurotransmitter. This suggests that the levels of PS may vary according to the requirements at the synaptic membranes and according to the fluctuations on the GABA concentration. From our results, we found that the levels of PS decreased when the neuronal activity was chronically inhibited through the long incubations with TTX. On the contrary, the PS levels increased if the neuronal activity was stimulated by a GABA-antagonist (BIC) (**Table 4**). This results may confirm that the intake of GABA can be boosted to counterbalance the over excitation caused by BIC, while their levels remain low if the excitability of the neurons is already depressed by the chronic administration of TTX. Implying that PSs could play an important role in the neuronal activity regulation by modulating its presence on the plasma membrane of hippocampal neurons.

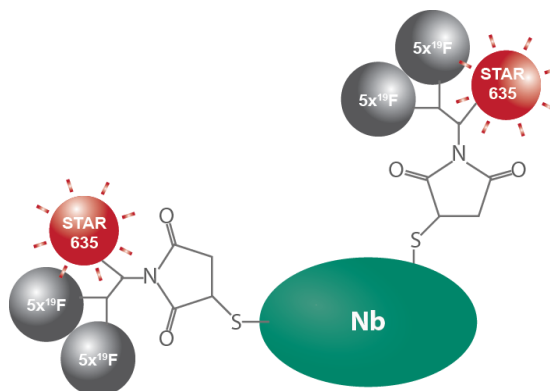
Additionally, in our analysis we found that PAs and TGs presence was significantly increased when incubating the neurons with both drugs. Since they are respectively known for being the precursors of glycerophospholipids and phospholipids (Tanguy et al. 2019; Tracey et al. 2018), this enhancement may be a response to the increased requirements of different lipid species to neutralize the changes induced in the neuronal activity.

## 3.2 RESULTS AIM II

### 3.2.1 Fluorinated nanobodies: FluorLink

With the conjugation of nanobodies with  $^{19}\text{F}$ -containing molecules (named FluorLink) in a site-specific manner, our group aimed to obtain immunoprobes that offer all the specifications cited above together with further advantages over previously developed probes (Angelo et al. 2014; Wilson et al. 2012). The conjugation of two FluorLink molecules with

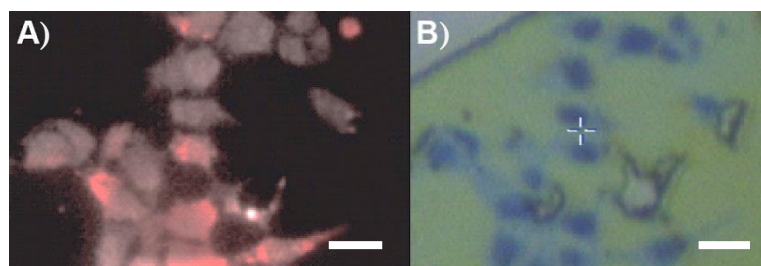
nanobodies that count with two ectopic cysteines (**Figure 39**) brings the presence of two Star-635 fluorophores and a total of 26 atoms of  $^{19}\text{F}$  per nanobody, producing enough signal to be detected in both techniques, fluorescence and SIMS imaging.



**Figure 39. Scheme of a FluorLink nanobody.** Two thiol-reactive FluorLink molecules, containing a Star-635 fluorophore and 13 x  $^{19}\text{F}$  atoms each, are conjugated to nanobodies that count with two ectopic cysteines. These nanoprobes can be used either in direct or indirect immunolabeling reactions.

To expand the applicability of this probe we tested FluorLink probes against two of the most commonly used targets in the detection of POIs in light microscopy; FluorLink nanobodies against fluorescent proteins and FluorLink nanobodies that specifically binds to mouse immunoglobulins.

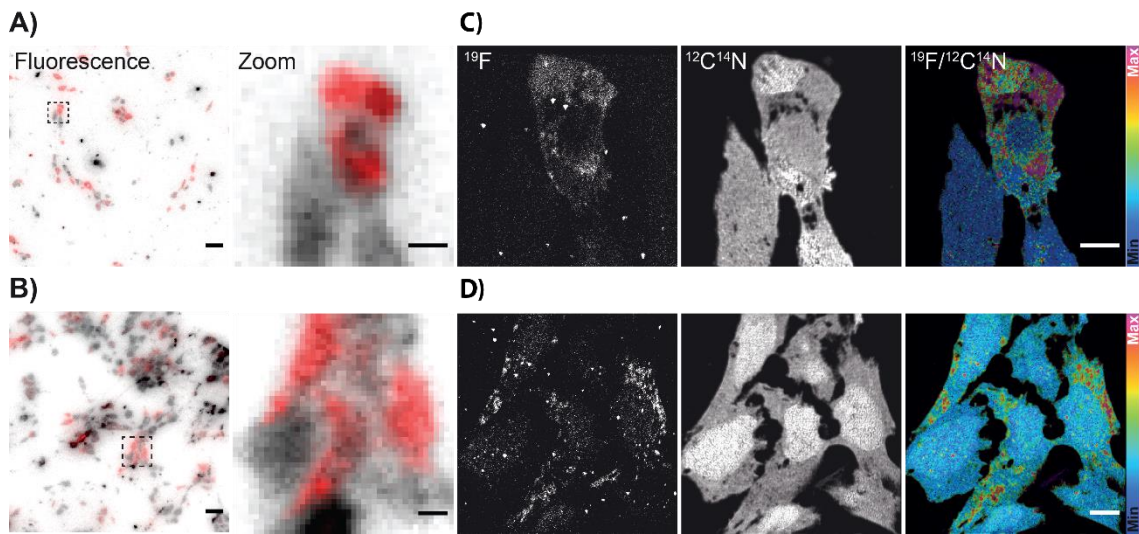
To test the FluorLink-nanobodies against fluorescent proteins, HEK293 cells were transfected with the mitochondrial protein TOM70 linked to GFP and another batch of cells was transfected with TOM70 linked to m-Cherry. Then, the cells were respectively stained with two FluorLink–nanobodies anti-GFP clones (which bind to different epitopes) and two clones of FluorLink–nanobodies anti-mCherry. To localize the transfected cells, images of the entire sample were first taken with light microscopy. The samples were then loaded into the NanoSIMS and the same areas of interest were re-localized thanks to the CCD-camera of the NanoSIMS (**Figure 40**) and sequentially ion imaged.



**Figure 40. Co-localization of ROIs using fluorescence and CCD camera images.** **A)** Fluorescence microscopy image were obtained before the NanoSIMS analysis (FluorLink-stained cells in red). The fluorescent signal detected on the red channel comes from the fluorophore Star-635. We can also observe in grey the non-transfected cells thanks to their autofluorescence. **B)** CCD image of the same area before starting with the ion imaging. Scale bars: 10  $\mu\text{m}$ .

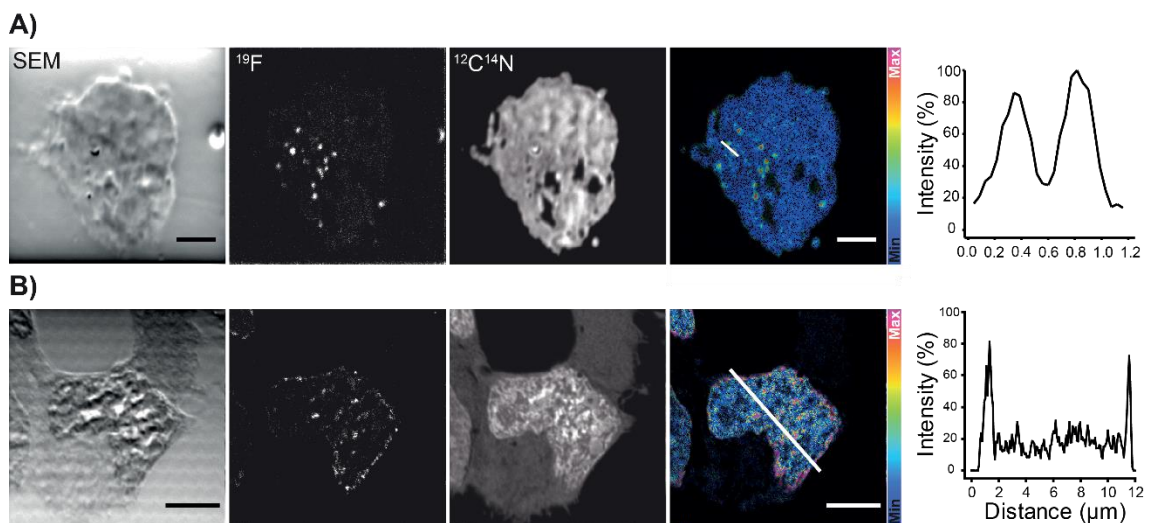
From the ion images, a significantly higher level of  $^{19}\text{F}$  signal was obtained from the cells strongly transfected with TOM70-GFP (**Figure 41A, red cells**) and TOM70-mCherry (**Figure 41C, red cells**) (respectively labeled with FluorLink–nanobodies anti-GFP and anti-mCherry), in comparison with the cells that did not express, or slightly express, fluorescent proteins (**grey cells in (Figure 41A and 41C)**). Furthermore, the signal of  $^{12}\text{C}^{14}\text{N}$  was homogeneously present across the entire cells, showing that no major topographical effect influenced the  $^{19}\text{F}$  signal. A good level of correlation was shown between the fluorescence and NanoSIMS images. In addition, for both, TOM70-GFP and TOM70-mCherry transfected cells, the  $^{19}\text{F}/^{12}\text{C}^{14}\text{N}$  ratio

image showed that the  $^{19}\text{F}$  label was circumscribed within the cytoplasm of transfected cells, forming tubular shapes that match the expected structure of labeled mitochondria (**Figure 41C-D**).



**Figure 41. Direct targeting of specific proteins for fluorescence microscopy and NanoSIMS with FluorLink-nanobody.** **A, C)** HEK293 cells were first transfected with TOM70-GFP and then labeled with anti-GFP FluorLink-nanobodies (clones #1 and #2). **B, D)** HEK293 cells transfected in this case with TOM70-mCherry were labeled afterwards with anti-mCherry FluorLink-nanobody (clones #1 and #2). **A, B)** The fluorescence microscopy images were obtained before their NanoSIMS analysis. The transfected cells are shown in red (signal emitted by the Star-635 fluorophore) while the non-transfected cells appear in grey (signal obtained from cell autofluorescence). On the first column, selected regions of interest are pointed with a dashed black line. On the second column, the zoomed-in images of those ROIs. **C, D)** NanoSIMS images of same areas. From left to right,  $^{19}\text{F}$  and  $^{12}\text{C}^{14}\text{N}$ , and ratio image of  $^{19}\text{F}/^{12}\text{C}^{14}\text{N}$ . Scale bars: 5  $\mu\text{m}$ . Figure adapted from Kabatas et al. (2019b) with permission from the Royal Society of Chemistry.

Having determined that the  $^{19}\text{F}$  signal was measurable in these samples, we proceeded to test the signal level and specificity of FluorLink immunoprobes against mouse antibodies, the targeted proteins were first labeled with primary antibodies followed by the incubation with the anti-mouse secondary nanobodies conjugated to FluorLink. For this, HEK293 cells were first incubated with a rabbit primary antibody against the peroxisomal protein PMP70 (**Figure 42A**) and another batch of HEK293 cells was incubated with a mouse primary antibody against the nuclear envelope protein, Lamin-B2 (**Figure 42B**).



**Figure 42. NanoSIMS imaging of indirectly labeled proteins with FluorLink.** HEK293 cells immunostained with a non-labeled mouse primary antibody together with a secondary nanobody anti-mouse conjugated to FluorLink. **A-B)** From left to right: SEM image of the cell, NanoSIMS images of  $^{19}\text{F}$  and  $^{12}\text{C}^{14}\text{N}$ ,  $^{19}\text{F}/^{12}\text{C}^{14}\text{N}$  ratio image, and line profile results over the  $^{19}\text{F}/^{12}\text{C}^{14}\text{N}$  images (pointed with red lines). **A)** An immunostaining against PMP70 was carried on HEK293 cells. The peroxisomes appeared as  $^{19}\text{F}$  bright dots and the line profile across two peroxisomes shows a significant signal-to-noise ratio of the  $^{19}\text{F}$  labeled structures. **B)** Immunostaining against lamin-B2 in HEK293 cell. Lamin-B2 was mainly identified at the edges of the nucleus, but interestingly also some spots appeared inside the nucleus. The line profile, which crosses the nucleus on the  $^{19}\text{F}/^{12}\text{C}^{14}\text{N}$  image (red line), shows that the  $^{19}\text{F}$  signal is mainly located along the nuclear envelope. Scale bars: 2  $\mu\text{m}$ . Figure adapted from Kabatas et al. (2019b) with permission from the Royal Society of Chemistry.

From the  $^{19}\text{F}$  NanoSIMS images, we observed the expected pattern for cells stained with the peroxisomal marker PMP70 of bright rounded shapes distributed across the cytoplasm (**Figure 42A**). Likewise, for the cells stained with anti-lamin-B2 primary mouse antibody, the signal of  $^{19}\text{F}$  showed a fine line that surrounds the nucleus of the cells, as well as some signal in the inside of the nucleus, exactly where most lamin-B2 molecules are expected to be localized (**Figure 42B**). In both cases, by observing the  $^{12}\text{C}^{14}\text{N}$  and the secondary electron microscopy (SEM) images, we could ensure that topographic artifacts were not causing the rise of  $^{19}\text{F}$  signal.

### 3.2.2 Boron containing-probes: BorEncode and BorLink

As already mentioned, several probes were earlier developed for the detection of specific proteins or cellular structures with SIMS (Wilson et al. 2012; Angelo et al. 2014). However, detectable probes in the positive ion mode, that enable the simultaneous detection of other positive ions such as cellular metal ions, were difficult to obtain. For this reason, two types of boron-containing dual probes were developed in our lab. In addition to facilitating the detection of POIs in positive SIMS ion mode, as in the case of FluorLink nanobodies, they enable the localization of POIs also under light microscopy. Both boron-conjugated probes, respectively called BorEncode and BorLink, contain a Star-635 and 20 atoms of boron ( $^{11}\text{B}$ ) (**Figure 43**). These two probes permit to follow different strategies to label newly synthesized proteins as well as to achieve the specific labeling of POIs.

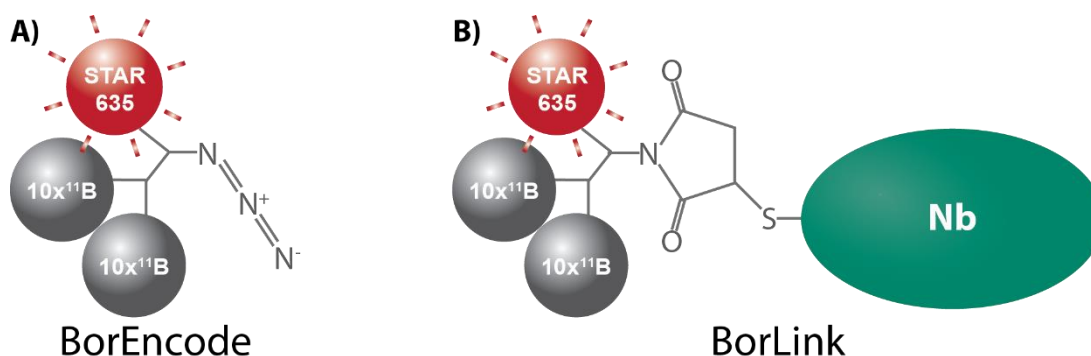


**Figure 43. Boron containing-probes.** Both, BorEncode **A)** and BorLink **B)**, contain hydrophobic aminobutyl-ortho-carboranes, bound to soluble short peptides carrying diverse functional groups, azide or maleimide, respectively, and a molecule of Star-635 fluorophore. BorEncode depends on a Copper (I)-catalyzed azide-alkyne cycloaddition (CuAAC) reaction to bind its target while BorLink counts with a nanobody that enables its binding to specific POIs.

BorEncode, is a conjugated probe based on the chemoselective reaction between UAAs and the carborate probe, reaction also referred as click chemistry (**Figure 43 ; strategy I**) (Wang et al. 2003). Through their physiological metabolism, the incubation of cells with UAAs that carry an alkyne group, will promote their incorporation in the newly synthesized proteins and will later enable their detection with our clickable probe. Then, with the application of

BorEncode probes, it becomes possible to visualize the distribution of these newly synthesized proteins with both SIMS and fluorescence microscopy.

First, to test BorEncode with the NanoSIMS, baby hamster kidney (BHK) cells were incubated with a medium that lacks methionine and contains the UAA homopropargyl-L-glycine (HPG) instead. In this manner, the UAA was included in all the newly synthesized. Then, the cells were fixed, permeabilized, and stained with BorEncode. The samples were embedded in LR-White resin and cut sections of 200 nm were placed on top of a silicon wafer to be first imaged with light microscopy and then with NanoSIMS.

To detect secondary ions with the NanoSIMS, the RF-plasma oxygen source was selected as the primary ion source. In addition to the detection of  $^{11}\text{B}$ , we also collected other elements as  $^{23}\text{Na}$  or  $^{40}\text{Ca}$  at a subcellular resolution to observe their distribution across the cell and have an internal reference for  $^{11}\text{B}$  level comparison among positive and negative control images (**Figure 44A**).

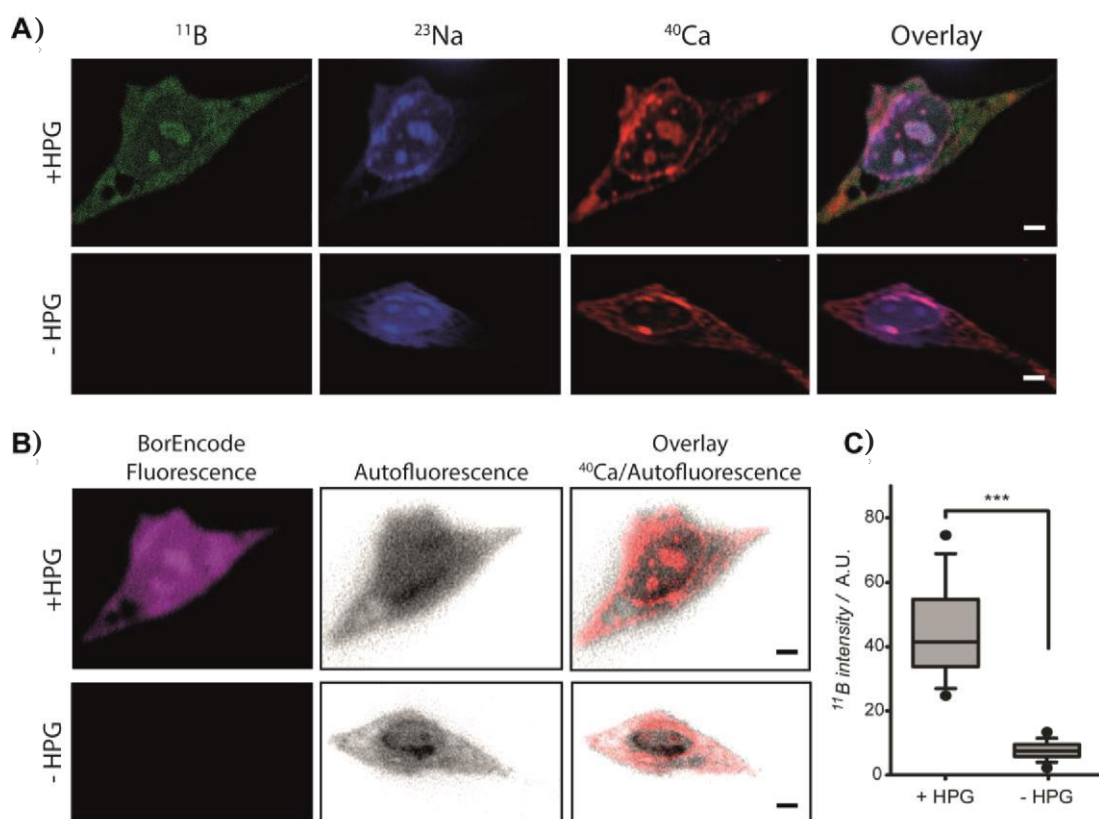


**Figure 44. Incorporation of HPG in BHK cells enables the labeling of all newly synthesized proteins with BorEncode.** **A)** On the upper row, NanoSIMS images of a representative labeled cells and a non-labeled cells on the lower row. From left to right,  $^{11}\text{B}$  (green)  $^{23}\text{Na}$  (blue) and  $^{40}\text{Ca}$  (red) and Overlay of the three ion images maintaining the colors. Scale bar: 5 mm. **B)** Fluorescence images of a labeled (upper row) and a non-labeled cell (lower row). From left to right, the fluorescence signal of the BorEncode (displayed in magenta), the autofluorescence signal from the cells (shown in gray), and an overlay image combining  $^{40}\text{Ca}$  (in red) and the autofluorescence signal (in gray) of the same cells. The fluorescence and  $^{11}\text{B}$  NanoSIMS images showed a good correlation. Scale bar = 5 mm. **C)** Plot of the  $^{11}\text{B}$  intensity normalized to the background intensities of the respective images. The detected levels of  $^{11}\text{B}$  were significantly higher in the labeled cells than in the negative controls. This difference was confirmed as highly significant ( $p < 0.0001$ ) by a Wilcoxon rank-sum test. Analyzed circular regions of interest (ROIs) = 120 per condition. The middle line in the boxes represents the median, the box edges the 25th percentiles, the error bars the 75th percentiles, and the dots the 90th percentile. Figure extracted from Kabatas et al. (2019a), courtesy of Angewandte Chemie.

From the cells incubated with HPG, where the BorEncode probe was selectively added,  $^{11}\text{B}$  was clearly visible across the cells showing an expected pattern for newly produced proteins.



On the contrary, on the batch of cells where the BorEncode probe was included but HPG was not present, the  $^{11}\text{B}$  signal was neglectable showing that the probe is highly specific (**Figure 44A**). This was also statistically confirmed when comparing the  $^{11}\text{B}$  intensity between the cells containing HPG and the negative controls that were not incubated with HPG (**Figure 44C**).

Thus, with the application of BorEncode on cells incubated with HPG, we were able to locate all newly produced proteins with both light microscopy and SIMS. However, BorEncode can also be employed to localize specific proteins of interest in the positive ion mode of SIMS. For this, the unnatural amino acids must be incorporated only into specific proteins, thus employing genetically encoded clickable UAAs.

A plasmid to encode syntaxin-1, a transmembrane protein, linked to a yellow fluorescent protein (YFP) was transfected to BHK cells. Employing an expanded genetic code system (Vreja et al. 2015; Kabatas et al. 2015), the cells incorporated the UAA propargyl-L-lysine (PRK) specifically at the Amber stop codon site, which was placed between syntaxin-1 and YFP. Afterwards, the BHK cells were chemically fixed and labeled with BorEncode through click reaction. The labeling of syntaxin1-YFP with BorEncode was confirmed before embedding with fluorescence images, where it was clear the overlapping of the YFP with the BorEncode signal. Unfortunately, after embedding and sectioning, the signal of YFP was lost. However, the Star-635 fluorophore carried by BorEncode was still detectable, which was employed to locate the click-labeled cells (**Figure 45B**, cells in magenta). The non-labeled cells were detected by their autofluorescence (**Figure 45B**, cells in grey). Both, the labeled and the non-transfected cells were then be located and imaged by NanoSIMS.

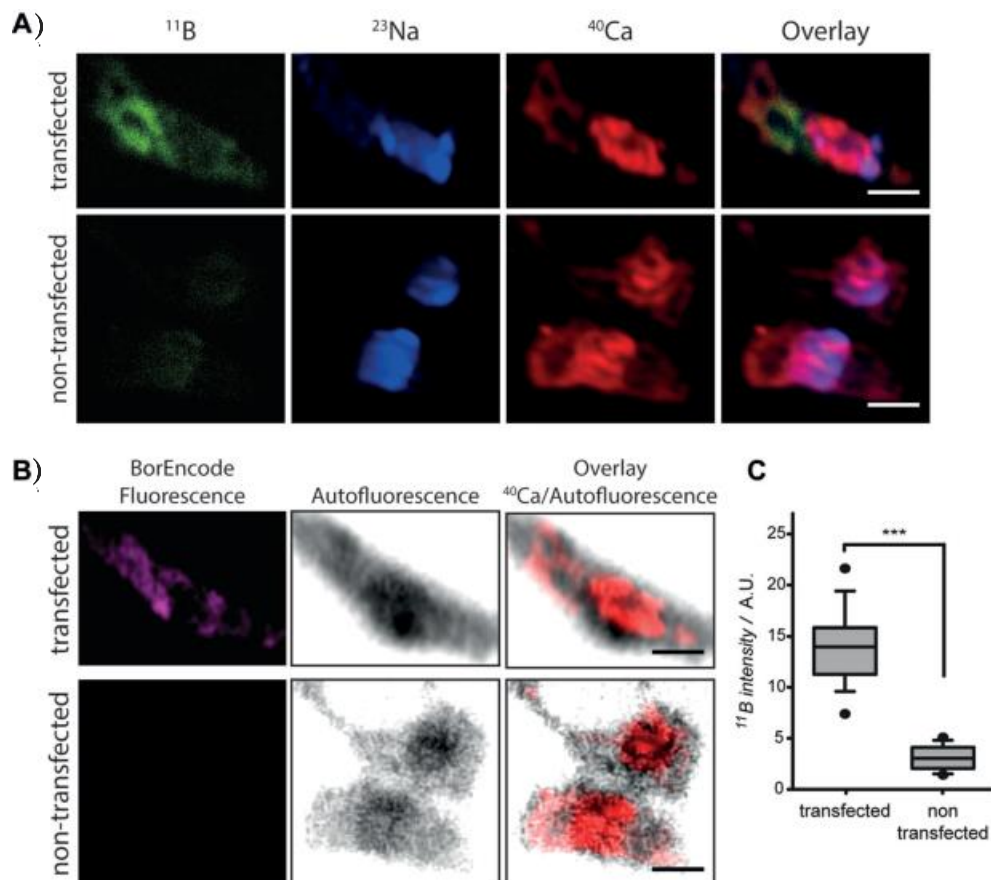


**Figure 45. Site-specific labeling with BorEncode of BHK cells expressing PRK-modified syntaxin-1.** **A)** NanoSIMS images of representative labeled (upper row) and non-labeled cells (lower row). From left to right,  $^{11}\text{B}$  (green)  $^{23}\text{Na}$  (blue) and  $^{40}\text{Ca}$  (red) and an overlay of the three ion images maintaining the colors. Scale bar = 5 mm. **B)** Fluorescence microscopy images of transfected (upper row) and non-transfected cells (lower row) of the same cells, obtained before the NanoSIMS imaging. Despite of the different pixel sizes and imaging depth of the two approaches, the fluorescence and  $^{11}\text{B}$  signals appear in good agreement in the transfected cells. Scale bar = 5 mm. **C)** Plot of the  $^{11}\text{B}$  signal intensity normalized to background (\*\*\* :  $p < 0.0001$ ). Number of ROIs, 60 for the transfected cells and 60 for the non-transfected. Figure adapted from Kabatas et al. (2019a), courtesy of Angewandte Chemie.

From this experiment, we could observe that  $^{11}\text{B}$  was in good agreement with the fluorescence image, in which high intensity was obtained only from the transfected cells. As expected, the  $^{11}\text{B}$  signal obtained from cells expressing syntaxin1-YFP was lower than the HPG-cells, were all newly produced proteins were labeled (**Figure 44**), but still sufficient to reveal the location of the POI in the cellular context of other naturally present metal ions such as  $^{23}\text{Na}$  and  $^{40}\text{Ca}$  (**Figure 45**). Beside the positive results obtained with BorEncode, we also developed and test BorLink. In this case, the binding approach to label the POIs is based on a nanobody conjugated to the boron-dual probe (**Figure 43B**). BorLink represents a good alternative for specific protein labeling since this probe contains a nanobody that selectively binds its target epitope. Like in the case of BorEncode, BorLink counts with a Star-635 fluorescence molecule that enables its detection via light microscopy as well as two groups of 10 atoms of  $^{11}\text{B}$  (20 atoms per probe). Furthermore, two commercially available clones of nanobodies against GFP were employed to label simultaneously two different epitopes, increasing the number of boron atoms per POI.

To test the application of BorLink, cells derived from monkey kidneys (COS-7) were transfected with a plasmid that encoded the mitochondrial protein TOM70 together with a green fluorescent protein (GFP). After 18 hours, the cells were fixed and immunostained with two types of BorLink-antiGFP-Nbs (targeting two different epitopes of GFP).

By adding both nanobodies, up to 40 atoms of boron can point at each GFP protein. Like in the case of YFP, after embedding and sectioning the fluorescence of GFP was lost. The remaining fluorescence signal from the Star-635 fluorophore was enough to distinguish the labeled cells (**Figure 46**, cells in red), from the cells that were only visible by autofluorescence (**Figure 46**, cells in grey). As for the BorEncode specific labeling, once the embedded section has been imaged with light microscopy and the location of the positive and non-labeled cells and is known, we load the samples in the NanoSIMS and with the help of the CCD camera, we localize the same areas.

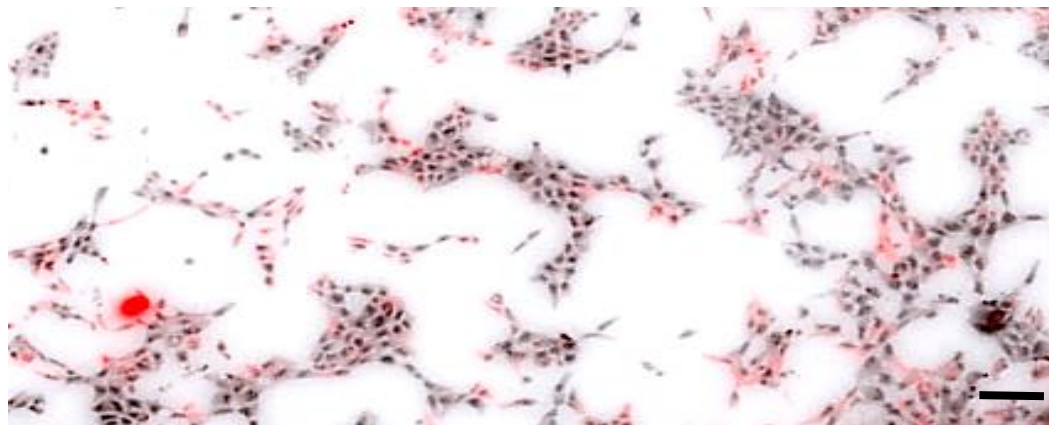


**Figure 46. Large-scale light microscopy image of COS-7 cells immunostained with BorLink-antiGFP-Nbs.** The light microscope images of the entire sections are later used as a reference to locate the positive cells with NanoSIMS. The autofluorescence signal of the cells is displayed in grey and the Start-635 signal from BorLink is displayed in red. Scale bar: 50  $\mu\text{m}$ .

For BorLink, we also selected the NanoSIMS positive ion mode to detect  $^{11}\text{B}$ , and  $^{23}\text{Na}$ , and  $^{40}\text{Ca}$  at a subcellular resolution to observe their natural distribution. This additional ions also serve us to have an internal reference for  $^{11}\text{B}$  level comparison between transfected and non-transfected cells (**Figure 47A**). Running a Wilcoxon rank sum test we statistically confirmed that the difference of signal level obtained from transfected cells stained with BorLink and the non-transfected cells also incubated with BorLink, was significant ( $p < 0.0001$ ) (**Figure 47C**).

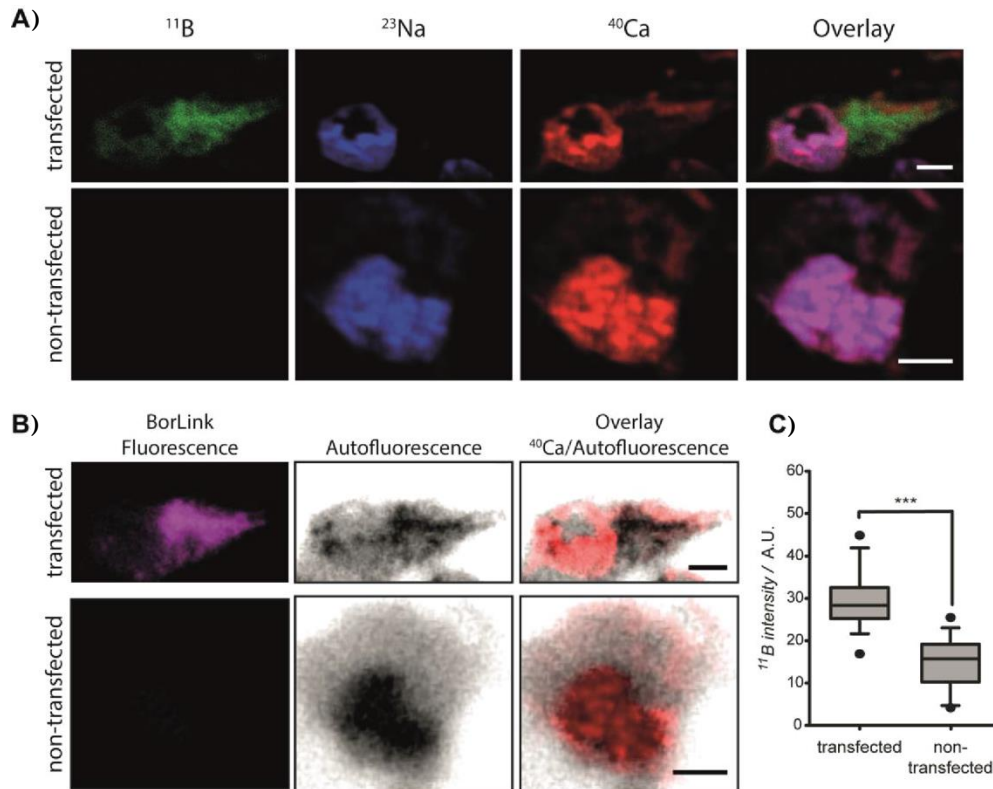


**Figure 47. COS-7 cells expressing TOM70-GFP labeled with anti-GFP BorLink nanobodies. A)** NanoSIMS images of transfected and non-transfected cells. From left to right,  $^{11}\text{B}$  (green),  $^{23}\text{Na}$  (blue) and  $^{40}\text{Ca}$  (red), and an overlay image of  $^{11}\text{B}$ ,  $^{23}\text{Na}$ , and  $^{40}\text{Ca}$  (maintaining same colors). Scale bars: 5 mm. **B)** Epifluorescence images of transfected and non-transfected cells obtained before the NanoSIMS analysis. Despite the different pixel sizes and imaging depth of the two procedures are different, the fluorescence and NanoSIMS images can be perfectly overlaid, showing that the fluorescence and  $^{11}\text{B}$  signals are in agreement in the transfected cells. Scale bars: 5 mm. **C)** Plot of the  $^{11}\text{B}$  signal intensity normalized to the background level of each image, to compare transfected and non-transfected cells (\*\*\*) :  $p < 0.0001$ ). Analyzed ROIs: 150. Figure extracted from Kabatas et al. (2019a), courtesy of Angewandte Chemie.

With this, we confirmed that the labeling of newly synthesized proteins, as well as the labeling of specific POIs with our dual nanoprobe, enabled the localization of their distribution, offering high specificity and sufficient sensitivity for their localization with SIMS and fluorescence microscopy. At the same time, we proved that the use of this type of probes represents a straightforward method to combine fluorescence and NanoSIMS images, showing a great agreement between the images from both techniques. Furthermore, these tools can be combined with other elements for the study of metabolic turnover with NanoSIMS as well as with other SIMS imaging techniques such as ToF-SIMS, where it could be combined with the imaging of other small species present in the same sample such as metabolites, peptides, sugars, or lipids.

### 3.3 RESULTS AIM III

The analyzed sections were obtained from the spinal cord of a MBP inducible knockout mouse. Starting at the age of 28 weeks, when most developmental myelination has been achieved, iKO mice were fed with a  $^{13}\text{C}$ -lysine diet for 45 or 60 days, followed by one week of chase with a non-isotopically labeled diet. Then, the animals were respectively sacrificed at 26 and 28 post tamoxifen injection (pti) weeks and the tissue samples were then collected for imaging.

The spinal cord samples were prepared following a standard TEM protocol but cutting the slices with a more compatible thickness for NanoSIMS. Thinner slices commonly used for TEM are too fragile to be imaged by directly applying the primary ion beam, therefore and after multiple tests, sections of 150 nm were used.

The samples were first mapped with TEM to identify morphological changes in the compact myelin structures induced by the lack of MBP. The most evident difference to the control mice was a tubular-vesicular enlargement of the inner tongue in the iKO spinal cord (**Figure 48A**). Afterwards, the same areas of interest were localized with the CCD detector of the NanoSIMS, thanks to the coordinates of the finder grids, and then analyzed with NanoSIMS. Regarding ion imaging, to work with these thin samples it is important to do not apply a high current for long periods, especially on small raster sizes, since the impact of the ion beam induces a rise of temperature that can critically damage the sample, and it may end up collapsing. Thus, 15 pA for only 30 seconds were applied to achieve a stable yield of the secondary ions before starting with the imaging. Then, the ion images from the  $^{12}\text{C}^{14}\text{N}^-$  (**Figure 48-Ac and 48-Bc**) and  $^{13}\text{C}^{14}\text{N}^-$  (**Figure 48-Ad and 48-Bd**) ion channels were taken from two consecutive layers. To obtain a higher signal-to-noise ratio, which becomes especially relevant for elements with lower abundance like  $^{13}\text{C}$ , the two layers are summed on expenses to loss some spatial resolution.

To analyze the  $^{13}\text{C}$  enrichment, we calculated the  $^{13}\text{C}^{14}\text{N}^-/^{12}\text{C}^{14}\text{N}^-$  ratio across the morphological regions of interest: axon, compact myelin, inner tongue, inner tongue tabulation, myelin debris, and myelinoid bodies. To proceed with the analysis, each TEM image was first aligned with its corresponding NanoSIMS ion maps and scaled to match the NanoSIMS data. Then, the ROIs were manually drawn on the TEM images, selecting them across the different morphological structures that were included in the analysis. Determining in this manner the local  $^{13}\text{C}$  enrichment, we observed and statistically confirmed, that after the tamoxifen induction of the knockout, the inner tongue structures that were unusually enlarged also presented a higher level of  $^{13}\text{C}$  than the myelin sheaths that were normally compacted (**Figure 48C**).

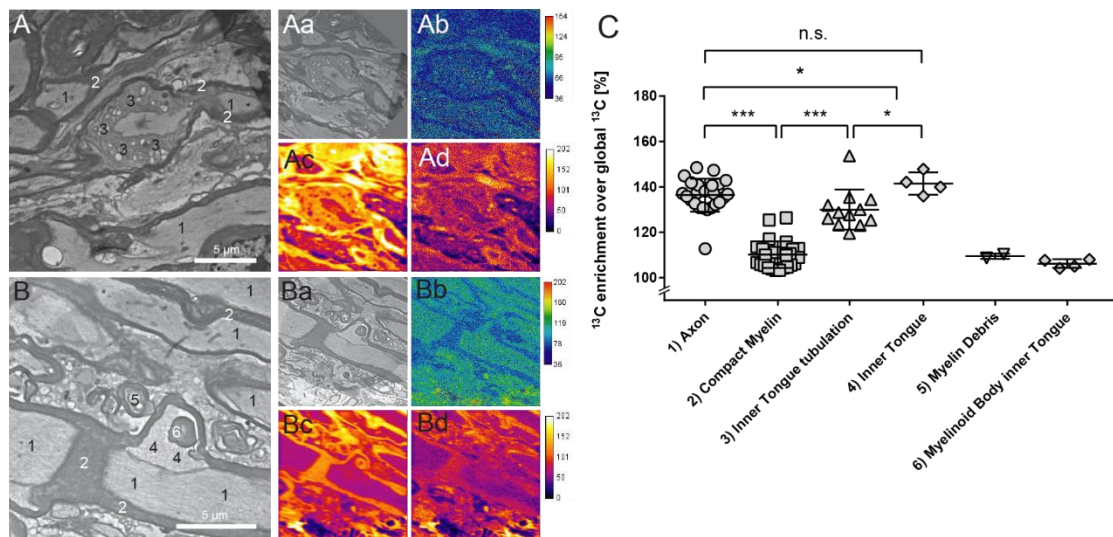


**Figure 48. Myelin turnover analysis with  $^{13}\text{C}$ -lysine feeding and NanoSIMS imaging in MBP iKO.** TEM image of longitudinal sections from the spinal cord of an iKO mouse fed for 45 days with SILAC diet (containing  $^{13}\text{C}$ -Lysine) and sacrificed (at 26 weeks pti) after 1 week of chase with non  $^{13}\text{C}$ -enriched diet. **A)** A tubular-vesicular enlargement of the inner tongue while on **B)** a myelinoid body is visible at the inner tongue on the TEM images. (Aa and Ba) Aligned to NanoSIMS TEM image, (Ab and Bb)  $^{13}\text{C}^{14}\text{N}/^{12}\text{C}^{14}\text{N}$  ratio, (Ac and Bc)  $^{12}\text{C}$  image, and (Ad and Bd)  $^{13}\text{C}$  image. Scale bars: 5  $\mu\text{m}$ . **C)**  $^{13}\text{C}$  enrichment of ROI. To define the ROIS, the TEM images were first aligned to their corresponding NanoSIMS images, then the ROIS were manually drawn over the stack of images guided by the morphological structures observed on the TEM image. The  $^{13}\text{C}$ -enrichment was calculated from the  $^{13}\text{C}^{14}\text{N}/^{12}\text{C}^{14}\text{N}$  ratio of every pixel in the ROI and then averaged. Every data point corresponds to the average value of the sampled ROI. Statistical analysis: two-tailed unpaired t-test; \* :  $p < 0.05$ , \*\* :  $p < 0.01$ , \*\*\* :  $p < 0.001$ . Figure extracted from Meschkat et al. (2022), courtesy of Nature.

Besides, we analyzed the  $^{13}\text{C}$  enrichment in different morphological structures from an iKO mouse that was pulse-labeled for 60 days and sacrificed after 1 week of chase with a non-labeled control diet at 28 weeks pti. Similar results to the 45 days pulse labeling were obtained and statistically confirmed (**Figure 49**).

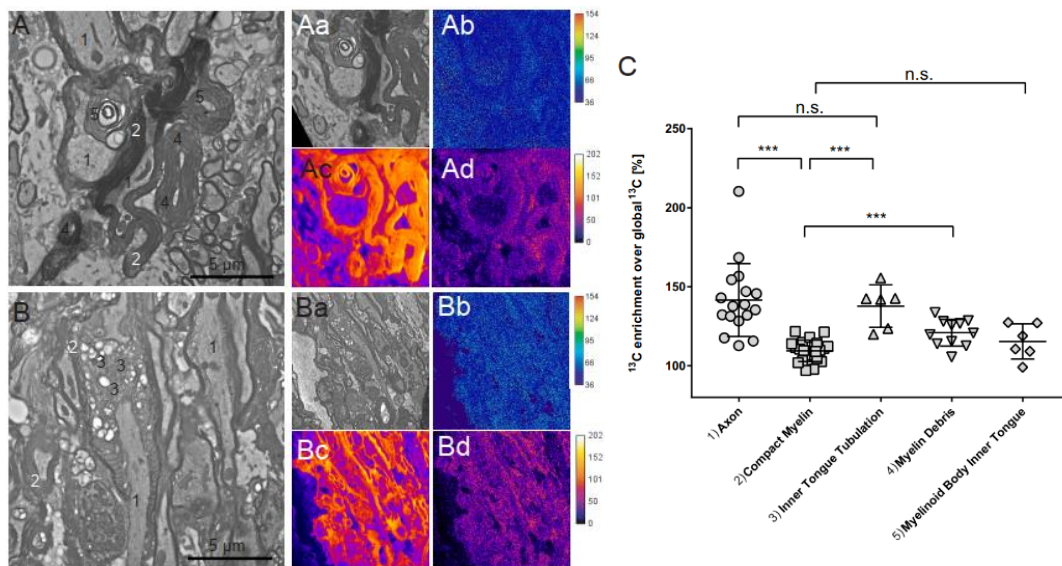


**Figure 49. TEM and NanoSIMS imaging of *MBP* iKO spinal cord after 60 d  $^{13}\text{C}$ -lysine diet feeding.** TEM image of a longitudinal spinal cord section from an iKO mouse fed for 60 d with SILAC diet ( $^{13}\text{C}$ -Lys) and sacrificed after 1 week of chase with non  $^{13}\text{C}$ -enriched diet at 28 weeks pti. Structures were analyzed by manually selecting small ROI on the isotope map and calculating the  $^{13}\text{C}^{14}\text{N}/^{12}\text{C}^{14}\text{N}$  isotopic ratio of every pixel in the ROI. **A)** Myelin outfolding, myelinoid bodies in the inner tongue and myelin debris. **B)** TEM image of a paranode with juxtapanodal myelin tubulation. **(Aa and Ba)** Aligned TEM image, **(Ab and Bb)** ratio of  $^{13}\text{C}/^{12}\text{C}$ , **(Ac and Bc)**  $^{12}\text{C}$  NanoSIMS image, **(Ad and Bd)**  $^{13}\text{C}$  NanoSIMS image. **C)**  $^{13}\text{C}$  enrichment of the sampled ROI. Each data point corresponds to the average value of the sampled ROI drawn manually on the analyzed structure. The numbers on the TEM image correspond to the sampled structures in C. The results were statistically confirmed by a two-tailed unpaired t-test; \* :  $p < 0.05$ , \*\* :  $p < 0.01$ , \*\*\* :  $p < 0.001$ . Scale bars: 5  $\mu\text{m}$ .

Therefore, correlating 3D TEM and NanoSIMS, we could visualize that newly formed non-compacted membranes appeared most prominently at the inner tongue at the juxtapanodes. The presence of myelinoid bodies indicated degradation of existing myelin at the abaxonal side and the inner tongue of the sheath. This, together with other results from the same study that are not included here but in the manuscript (Meschkat et al. 2020), revealed that there was myelin thinning and shortening at the internodes, with about 50 % myelin lost after 20 weeks, which ultimately led to axonal pathology and neurological disease.

## 3.4 RESULTS AIM IV

### 3.4.1 Sample preparation

After testing different conditions to improve the lateral resolution achieved with the three techniques, we found that we were not able to achieve satisfactory SIMS imaging with samples cut thinner than  $\sim 90$  nm, regardless of the chosen resin, or the grid coating. Oppositely, much thicker samples become a problem for TEM imaging. Thus, we employed sections of  $\sim 160$  nm. These samples, still relatively thick for TEM, required a grid thin coating that ensured a good conductivity. This can be achieved through the application of a thin carbon layer (Lovrić et al. 2017). We found that copper grids incorporating a support film of 10 nm Formvar and 1 nm Carbon coating offered a suitable conductivity while also improved the stability of the samples.

### 3.4.2 NanoSIMS imaging

The samples, previously imaged by light microscopy and TEM, were loaded on the NanoSIMS and first inspected with its in-built optical camera (CCD camera). In this manner, we could roughly localize the areas of the samples that were previously imaged by the two other techniques, guided by the marks inscribed on the finder grids. Once a particular area of interest was found with the camera, we could switch to SIMS mode. Additionally, the secondary electron detector was employed to fine-tune the exact imaging position, since it enabled the visualization of the grid bars, as well as showing the characteristic shapes and arrangement of the cells.

A relatively low current was applied for a short time to implant the area, enhancing the signal obtained, visualizing better the cells, and reaching a stable secondary ion yield. These relatively thin samples cannot be hit by high currents, as they can be damaged and collapse, especially when trying to image areas  $< 20 \times 20 \mu\text{m}$ , or implanting for longer time. Therefore, we applied an ion current of 15 pA for  $\sim 30$  seconds that was sufficient to reach a stable

secondary ion yield and a current of 0.5 - 1.5 pA during imaging that allowed us to detect all the desired ions at an acceptable level (Figure 50).

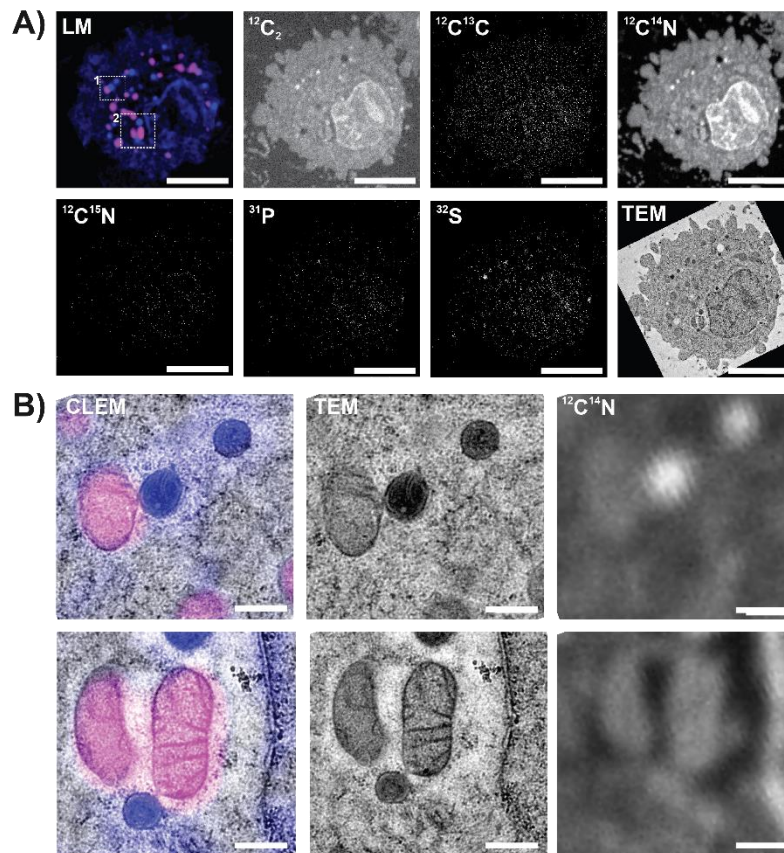


**Figure 50. Detailed views of CLEM-SIMS. A)** Displayed in blue, we can observe the fluorescence emitted by the uranyl acetate, and in magenta, the MitoTracker fluorescence. Then, the different isotopes detected by NanoSIMS are shown with their respective ion images ( $^{12}\text{C}_2$ ,  $^{12}\text{C}^{13}\text{C}$ ,  $^{12}\text{C}^{14}\text{N}$ ,  $^{12}\text{C}^{15}\text{N}$ ,  $^{31}\text{P}$ , and  $^{32}\text{S}$ ). The low abundance of  $^{13}\text{C}$  and  $^{15}\text{N}$  is caused by the lack of exogenous isotopically labeled components in this experiment. The last image corresponds to the TEM image of the same cell. Scale bars: 2  $\mu\text{m}$ . **B)** Higher zoom views of the regions marked by white squares in the fluorescence microscopy image of panel a). From left to right: CLEM images, TEM, and NanoSIMS image of  $^{12}\text{C}^{14}\text{N}$ . Scale bars: 500 nm. Figure extracted from Lange et al. (2021), courtesy of PlosOne.

### 3.4.3 CLEM-SIMS image and data analysis

As a proof of concept, and to prove what can be done in future experiments, we combined CLEM-SIMS to analyze the isotopic composition of diverse cellular components along with a more specific analysis of the mitochondria. For the first analysis, we selected from several cells the fluorescent-labeled mitochondria together with other cellular components such as cellular granules, which are presumably similar to dense-core vesicles (Kim, T. et al. 2006), euchromatin and heterochromatin, and regions that apparently did not belong to specific organelles, and we therefore considered as cytosol (Figure 51B-D). To normalize the signal levels obtained from each isotope, we normalized all signals by calculating their ratio with the ubiquitous  $^{12}\text{C}$  signal. With this, we could detect significant differences between the mentioned cellular components. For example, the heterochromatin showed higher levels of  $^{31}\text{P}$  and  $^{32}\text{S}$  than the euchromatin. This is an expected result due to the higher levels of nucleic acids in heterochromatin, which implies also a higher concentration of phosphorus. The same trend was statistically determined in the comparison between the mitochondria and granules against the cytosol. The dense granules and the heterochromatin also showed a high

$^{14}\text{N}$  enrichment (**Figure 51B**), suggesting that these components are particularly protein-rich when compared to other cellular constituents.

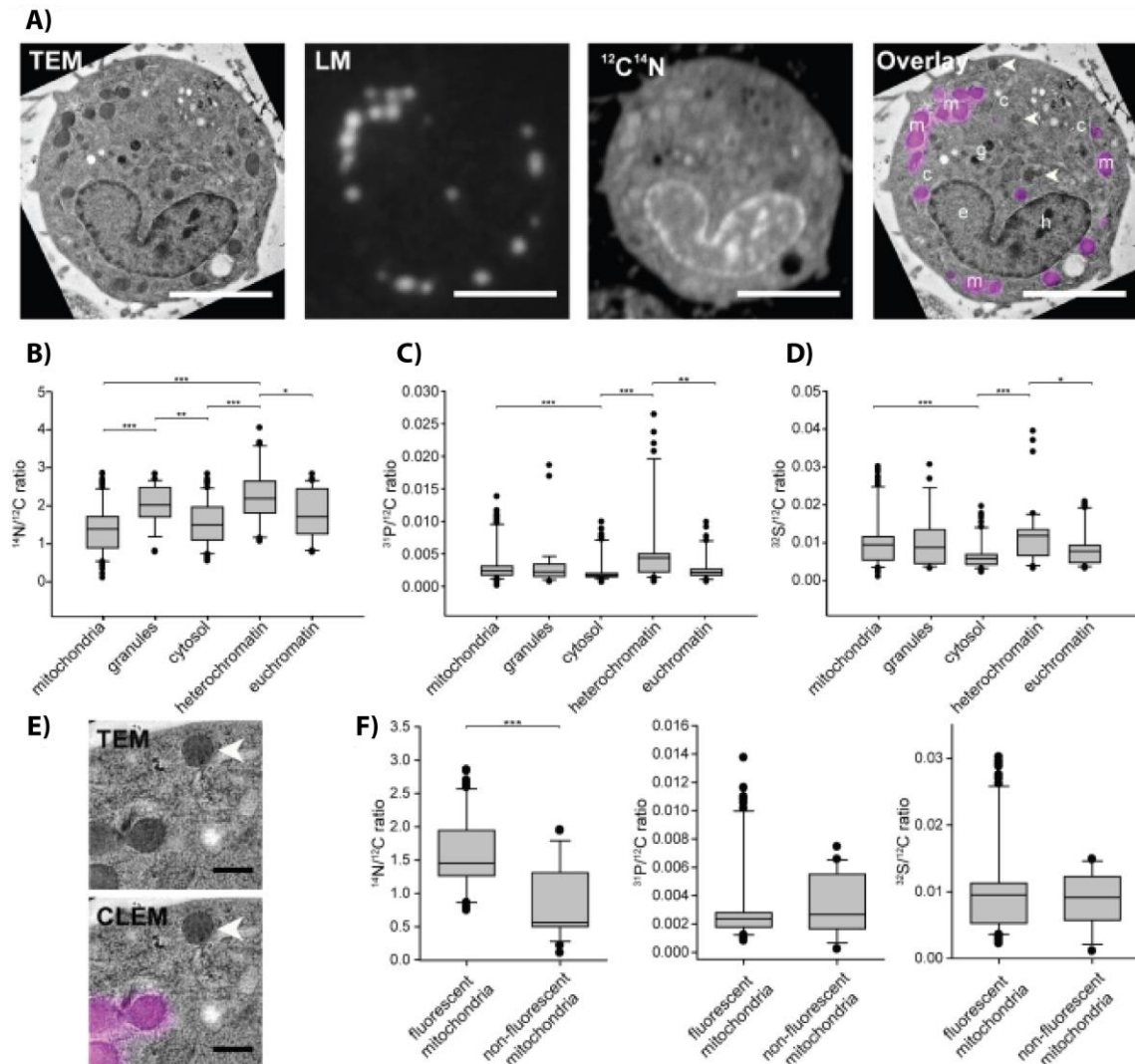


**Figure 51. Analysis of CLEM-SIMS data determines isotopic distribution differences between cellular compartments in cultured HeLa cells.** **A)** CLEM-SIMS images of a HeLa cell labeled with MitoTracker. From left to right: TEM, MitoTracker signal obtained with light microscopy, NanoSIMS ( $^{12}\text{C}^{14}\text{N}$ ) image, and CLEM (with MitoTracker signal displayed in magenta). On the overlay, the letters refer to mitochondria (m), granules (g), cytosol (c) heterochromatin (h) and euchromatin (e). The white arrowheads point to several mitochondria that did not get labeled with MitoTracker, but were visible in the TEM image. Scale bars:  $5\mu\text{m}$ . **B-D)** Comparison charts of the isotopic levels between multiple cellular compartments. The ROIs were selected on the already aligned TEM image and to normalize the intensities, the signal of the different isotopes was divided by  $^{12}\text{C}$  (present both in the cells as in the plastic resin). To statistically confirm the results, a Kruskal-Wallis tests, followed by Tukey post-hoc tests were applied; (\* :  $p < 0.05$  ; \*\* :  $p < 0.01$  ; \*\*\* :  $p < 0.001$ ). **B)**  $^{14}\text{N}/^{12}\text{C}$  analysis. **C)**  $^{31}\text{P}/^{12}\text{C}$  analysis. **D)**  $^{32}\text{S}/^{12}\text{C}$  analysis. **E)** Zoom-in view of a cell area containing several mitochondria (delimited with a green dashed line on panel A). Not all mitochondria was labeled with MitoTracker (magenta), the unlabeled ones are pointed with a white arrowheads. Scale bars:  $500\text{nm}$ . **F)** Isotopic analysis to compare the labeled and non-labeled mitochondria. For this analysis, 85 fluorescent mitochondria and 24 non-labeled ones were selected. The differences were statistically tested by Mann-Whitney tests; (\*\*\*) :  $p < 0.001$ ). Figure adapted from Lange et al. (2021), courtesy of PlosOne.

To carry the second analysis, we employed MitoTracker (organelles displayed in magenta in **Figure 51**), a commercially available fluorescent dye that labels mitochondria in live cells based on the mitochondrial membrane potential. Interestingly, along with the numerous labeled mitochondria, there were some that despite being clearly visible by TEM and not showing obvious morphology problems, were not visible in light microscopy (white arrowheads in



**Figure 51A and 51E**). Since MitoTracker requires an intact mitochondrion (Chazotte 2011), it is possible that the mitochondria missing the fluorescence label are dysfunctional ones.

The resolutions obtained with fluorescence microscopy (**Figure 52A**) and EM (**Figure 52B**) was similar to the typical performance of these techniques. To measure the NanoSIMS lateral resolution, we applied the most common calculation for SIMS, which measures the distance across which the signal intensity drops from 84 % to 16 % of its maximum (Gorman and Kraft 2020), obtaining an average resolution of  $\sim 160$  nm (**Figure 52C**). The NanoSIMS lateral resolution was better than the resolution of fluorescence microscopy but worse than the resolution that we have obtained on similar samples placed on silicon wafers ( $\sim 80$ -110 nm) (Saka et al. 2014; Agüi-Gonzalez et al. 2021b). This declining is caused by the particular NanoSIMS settings that must be adapted to work with these considerably fragile samples.

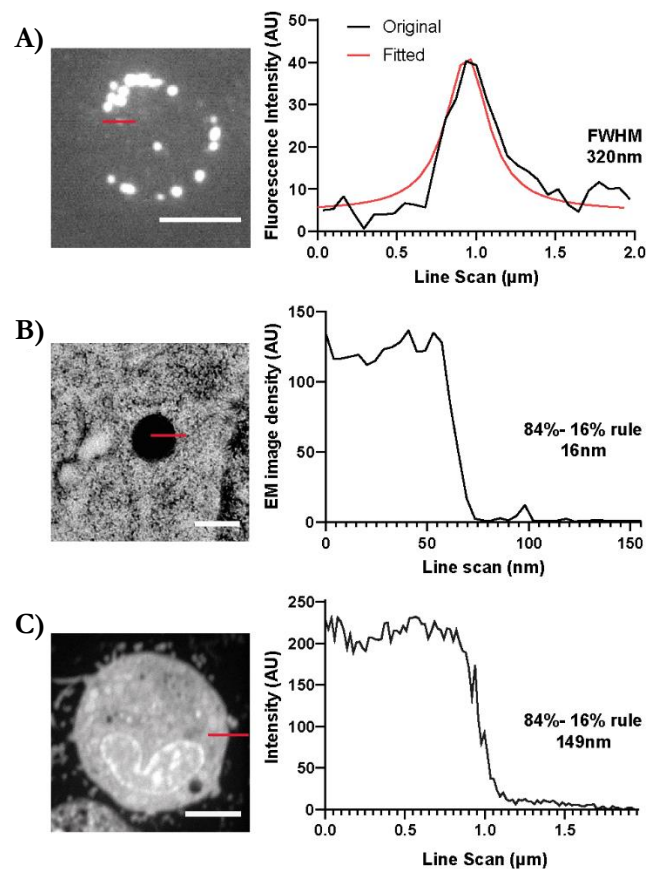


**Figure 52. CLEM-SIMS lateral resolutions.** **A)** Lateral resolution analysis of the light microscopy imaging. Intensity profiles were drawn crossing areas with high MitoTracker signal. From 10 measurements, we obtained an average resolution of  $321 \pm 36$  nm. The full width at half maximum (FWHM) was determined from Gaussian curves fitted on the spots. Scale bar: 5  $\mu$ m. **B)** Lateral resolution analysis for TEM images. Like for SIMS, we calculated the distance in which the maximum intensity of the signal drops from 84 % to 16 %, resolving from 10 measurements an average resolution of  $22 \pm 6$  nm. Scale bar: 500 nm. **C)** Lateral resolution analysis for NanoSIMS images. Applying the 84 %-16 % resolution method on the  $^{12}\text{C}^{14}\text{N}$  images on 7 measurements, we obtained an average resolution of  $164 \pm 27$  nm. Scale bar: 5  $\mu$ m. Figure adapted from Lange et al. (2021), courtesy of PlosOne.

---

## 4. DISCUSSION

---

### 4.1 GENERAL DISCUSSION

Secondary ion mass spectrometry has traditionally been a technique practically reserved for geology and material science. Nonetheless, during the last decades numerous research teams have incorporated SIMS into many other fields. The evolution of these instruments and the continuous optimization of the methods have progressively facilitated the application of SIMS in the study of biological samples. The arrival of new primary ion sources together with the improvement of the spatial and mass resolution have allowed mass spectrometry to become a competitive imaging alternative able to reveal cellular and subcellular information. The capabilities of these instruments and their compatibility with other imaging techniques such as light microscopy, TEM or AFM, make SIMS a very promising tool that will keep gaining relevance in biology.

There is not a unique SIMS imaging instrument valid for all types of analysis, thus, depending on the experimental questions, it is crucial to determine beforehand the type of analysis that must be performed and the instrument features that are more relevant for our study. In this regard, ToF-SIMS is a very versatile tool able to carry out exploratory investigations to examine hypotheses that are not necessarily based on specific targets. For example, the study of the lipid composition of the neuronal plasma membrane and its variations linked to the neuronal activity or the study of the lipid accumulation in the heart after myocardial infarction. Likewise, if we already know the specific molecules involved in these processes ToF-SIMS can typically show the distribution of molecules up to 2.5 kDa, and, thanks to its mass accuracy and MS/MS capabilities to ensure a reliable mass peak identification. Alternatively, NanoSIMS is an ideal approach to image surfaces with a higher lateral resolution when only a few monoatomic or very small molecules are the targets of the study. Also, compared to the high dimensionality of ToF-SIMS data, NanoSIMS output implies a much elementary data analysis. Nonetheless, NanoSIMS can still provide more details at a subcellular level thanks to its coaxial configuration, which reduces the focus size of the primary ion beam, as well as reducing aberrations and increasing the transmission efficiency of the instrument ( $\sim 80\%$ ). However, to ensure homogeneous NanoSIMS images, only small areas of  $< 300\ \mu\text{m}$  can be analyzed, and multiple tiles must be concatenated when trying to image bigger areas. Thus, ToF-SIMS represents a better option to image larger areas when the required lateral resolution is not a limitation.

Independently of the chosen instrument, applying imaging mass spectrometry in the study of biological samples still presents numerous limitations and challenges, including; 1) the impossibility of live-cell imaging and difficulties regarding sample preparation, 2) the need of improving the spatial resolution of SIMS to match the level of other imaging techniques, 3) the mass range limits and the accurate identification of secondary ion species, 4) the time cost of SIMS imaging and the high dimensionality of the data. Thus, it is also crucial to keep in mind that we can circumscribe such limitations by combining SIMS with other techniques.

Fluorescence imaging, which can conveniently accomplish live imaging with a spatial resolution beyond the light diffraction limit, represents with no doubt the most common tool for high-precision imaging in biology. Nevertheless, light microscopy cannot provide all the information that SIMS can offer and always requires the use of light-emitting probes,

either immunoaffinity or genetically encoded labels that facilitate the localization of particular analytes. On the contrary, SIMS allows the analysis of unlabeled samples, which represents a big advantage since some biomolecules such as lipids, present abnormal behavior when labeling them with fluorophores or when employing fluorescent analogs. Therefore, SIMS represents a more suitable approach for the study of certain biomolecules such as lipids in physiological conditions. Still, given its own nature and the high vacuum conditions, SIMS is not compatible with live-cell imaging, however, it can reveal the chemical composition of solid biological samples, determining the distribution of different types of biomolecules across tissues, cells and even subcellular structures. Additionally, SIMS can trace the metabolic fate of certain analytes. On the one hand, the addition of exogenous biomolecules that contain rare stable isotopes enable the study of their metabolic turnover. On the other hand, it is possible to directly study the pharmacokinetics of certain drugs, providing information about their distribution among different tissues, cell types and cellular compartments.

Regarding fixation methods employed in SIMS, when analyzing biological specimens, the ultimate aim is to preserve intact their original morphology, as well as the distribution and innate arrangement of their molecules. Several fixation methods, such as freeze-hydrated, freeze-drying, high-pressure freezing, chemical fixation, or plastic embedding, are employed in SIMS providing reliable results. Nonetheless, all these methods carry certain risks and drawbacks regarding the maintenance of the native state of the samples. For example, to avoid molecular rearrangement and possible ultrastructure damage caused by ice crystal formation, applying high-pressure freezing would be a safer alternative to freeze samples. However, the samples must then be quickly transferred from the liquid nitrogen storage into the imaging device, which is in the end not so trivial, or to proceed with freeze-substitution if we want to analyze such samples on instruments that do not incorporate a cold stage. In the case of freeze-drying samples, the water removal may induce a certain degree of shrinkage, and, also like in the case of freeze substitution, small water-soluble molecules may be dragged by the extracted water. Currently, only ToF-SIMS is compatible with the analysis of frozen-hydrated samples. This ensures less shrinkage, and regardless of the risks of ice crystal formation, it has shown to induce fewer changes in the biomolecular arrangement. The main handicaps are the sample handling itself and that frozen-hydrated samples are not compatible with some other imaging methods like TEM. Oppositely, the use of chemical fixatives, which have been employed on SIMS imaging correlation, is often not compatible with ToF-SIMS due to the generation of chemical interferences but perfectly compatible with NanoSIMS. The problem is that some molecules can be still washed away after chemical fixation since not all chemical fixatives are capable to equally stabilize every type of molecule. The final consequence is that, independently of the fixation method, we can clearly determine what remains, but we cannot identify what is missing, in the same manner that we cannot ascertain how the addition of fixatives are interfering with our results. Thus, further optimization and new alternatives for sample preparation, as well as a deeper analysis and identification of losses must be accomplished, bringing a better understanding of SIMS results in biology and determining the precise effects of the sample preparation.

Despite SIMS can achieve a depth resolution of only a few nanometers, their current lateral resolution (axis X and Y) cannot match TEM or compete with super-resolution microscopy, which can record single fluorophores and provide absolute quantification of the targets. Nevertheless, the resolution of NanoSIMS also goes beyond the light diffraction limit and can achieve  $< 50$  nm in both negative and positive secondary ion modes. The problem is that further optimization of SIMS lateral resolution has to deal with several encounters. Among others, the abundance of particular species within small analyzed volumes together with their ionization probability, especially for biological high-resolution images, where the number of secondary ions can be too low for being detected. The yield of secondary ions is

mainly affected by the features of the primary ion source but also by the properties of the targeted analytes and their chemical and topographical environment. Thus, the heterogeneity of biological samples may induce big variation on the secondary ion yield and only relative quantifications can be granted.

The fragment reduction induced by the new primary ion sources is accompanied by a contraction of the secondary ion yield, however, alternative approaches like laser secondary neutral mass spectrometry (laser-SNMS) can compensate the low emission of secondary ions. Further improvements, not only regarding the yield of ionized secondary species but also to increase the transmission power and sensitivity of the instruments are required to minimize the gap between available molecules and detected ions to keep increasing the lateral resolution of SIMS.

The mass limit of ToF-SIMS, detecting molecules up to 2 kDa, capacitates it for the detection of small protein fragments, lipids, and even small proteins but does not permit the detection of proteins which are often much heavier. NanoSIMS mass range is far more limited, detecting only single atoms or small molecules. For both approaches, the mass restrictions can be bypassed with the use of SIMS-compatible probes which carry non-common elements that can be distinguished from the biological material. In this manner, it is possible to locate specific biomolecules that otherwise could not be detected.

Another relevant point is the mass accuracy of SIMS instruments and the correct identification of the secondary ion species. For instruments that collect the entire spectrum at each pixel, such as ToF-SIMS, the use of cluster primary ion beams can produce secondary ions up to thousands of Da offering a lower level of ion fragmentation. Especially at the high mass range, the ability to resolve the identity of isobaric interferences still represents a huge challenge for SIMS. The use of tandem mass spectrometry (MS/MS or MS<sup>n</sup>), which breaks the initial secondary ions (precursor ions) into smaller components (product ions), facilitates the identification of high mass peaks when the mass resolution of the regular ToF instruments is not enough. Also, when employing traditional ToF-SIMS configurations, either high lateral resolution or high mass resolving power has to be chosen. Delayed extraction, which decouples the impact of the primary ion beam from the extraction of secondary ions can enhance the mass resolution power while maintaining the spatial resolution. Those, among other options based for example on computational analysis, may be quite helpful to determine with higher confidence the identity of the visualized species.

Due to the time cost of SIMS biological studies (considering the sample preparation, imaging, and data analysis), the sample size accepted for this image modality tends to be lower than the approved for other imaging modalities such as light microscopy. The time consumed on preparing samples, including cell culture, immunostainings or fixation, as well as the time required to optimize the instruments and running images with SIMS, have still a large margin to keep improving.

Furthermore, since some modalities such as ToF-SIMS do not require prior molecular targets, a huge number of secondary ion species are collected in a single experiment. The large amount of data and its high dimensionality make it a perfect candidate for semi-automated or automated computational analysis. The implementation of computerized analysis could considerably reduce the time spent on this task and also help to uncover hidden mass associations, even when combining data from multiple imaging modalities. This speed-up, together with a time reduction on the previous steps, could help to increase the sample size in SIMS studies, bringing more solid and reliable results.

## 4.2 DISCUSSION AIM I

In conclusion, the lipid composition of the plasma membranes of hippocampal neurons seems to reflect the variations of the basal neuronal activity. After long incubation times with TTX and BIC, significant modifications on the lipid profile were observed, principally ceramides, PSs, PAs, and TGs. This suggests that the membrane lipids organization can be modified to fit to, or even to mediate, neuronal and synaptic activity. In addition to further physiological investigations, this shows that mass spectrometry imaging can be also used to understand better the lipid alterations behind several neurodegenerative diseases as well as psychiatric conditions.

## 4.3 DISCUSSION AIM II

These novel dual probes enable the labeling of all newly synthesized proteins (BorEncode) as well as the labeling of specific POIs (possible with BorEncode, BorLink and FluorLink), enabling the visualization and analysis of their distribution with both imaging techniques, SIMS and fluorescence microscopy, at a high spatial imaging and precision of labeling. Due to the lack of detectable probes for the positive ion mode of SIMS, the development of Boron conjugated probes provide a high affinity and specificity alternative for fluorescence and SIMS imaging that can be crucial for the study of other positive ions such as  $\text{Na}^+$ ,  $\text{K}^+$ ,  $\text{Mg}^{2+}$ , or  $\text{Ca}^{2+}$ . Moreover, these probes are not only useful for the analysis with NanoSIMS but also can be employed in investigations carried by other SIMS techniques that allow the simultaneous imaging of specific POIs together with other small molecules such as metabolites, sugars or lipids that are naturally present in biological samples. Thus, these new SIMS compatible probes can be very useful to investigate cellular and molecular processes where multiple types of molecules are involved.

Additionally, in order to increase the detectability of low abundance proteins, the nanobody-conjugated probes allow the amplification of the signal through intermediate steps of staining with sequential addition of secondary antibodies or nanobodies. From our experiments, this enhancing strategy has shown high selectivity and sensitivity for target molecular imaging with NanoSIMS, the addition of more affinity probes worsen the spatial resolution by increasing the linkage error from the original POI position. Therefore, this strategy would be more suitable for other SIMS techniques, such as ToF-SIMS, which works in a lower range of spatial resolution.

To produce a more accurate alternative to the enhancing strategy, further development of nanoprobe, which can offer a higher sensitivity for SIMS detection by increasing the amount of atoms of the chosen isotope, would be highly desirable. However, this is not a trivial issue and requires a very careful design to avoid the risk of precipitation and the loss of immunoaffinity. Furthermore, the production of future probes, carrying different labeling elements and different fluorophores for targeting different primary antibodies, would enable the generation of multicolor images on SIMS.

#### 4.4 DISCUSSION AIM III

Based on our  $^{13}\text{C}$  enrichment analysis and confirming what other studies also determined (Snaidero et al. 2014; Stadelmann et al. 2019), we found that the inner tongue and especially at the juxtaparanodes show higher metabolic activity rates. Supported by the NanoSIMS mapping of our iKO mice, these cytoplasm-rich compartments represent the most likely places where newly synthesized components incorporate into the myelin sheath, also in adulthood.

Thus, in the presented work, combining the capabilities of electron microscopy and nanoscale secondary ion mass spectrometry, we investigated the stability of myelinated tracts after experimentally avoiding the compaction of newly synthesized myelin in the CNS of adult mice, using a tamoxifen-inducible MBP null allele. Thanks to the combination of transmission electron microscopy, nanoscale mass spectrometry imaging, and the mouse model of adult myelin turnover, we could reveal the insertion sites of newly synthesized myelin. The determination and spatial localization of myelin turnover areas can help to understand how myelin sheaths behaves during aging, revealing further details about its dynamics and the stability of the structures and revealed that functional axon-myelin units require a continuous incorporation of newly generated myelin membranes.

However, we cannot exclude that also the outer tongue has an active role in the myelin renewal process. With our data, discriminating the tubulated leftovers from potentially outer tongues get complicated, since the association between the respective axon and the membrane tubules is commonly lost. A further and more detailed investigation could be carried in the future to resolve this uncertainty. Withal, the inclusion of light microscopy or the use of immunoprobes, detectable either by SIMS or EM, to point at specific proteins of interest could provide additional information (Agüi-Gonzalez et al. 2021).

#### 4.5 DISCUSSION AIM IV

The protocol here presented enabled a straightforward analysis of several subcellular structures, demonstrating an excellent preservation of the organelles, revealing their isotopic composition and at the same time, the localization of specific proteins of interest.

This approach enables a look into the basic chemical composition of several cellular organelles, determining the abundance of endogenous elements, like nitrogen, carbon, phosphorus, or sulfur. With this, multiple differences can be detected among the analyzed organelles. Some of them can be attributed to their already known composition, while others can be more surprising, and require further study. In addition, including pulses of isotopically labeled biomolecules in future experiments, would enable to not only analyze the chemical composition of different cell compartments with this protocol but also to address their metabolic turnover.

The main issue regarding the chemical fixation used in this protocol is that this procedure may induce strong modifications to the samples. Since it is not an instant process, until the sample gets totally fixed, the cells are slowly dying and probably acquiring some aberrant biological activity like osmotic swelling (Smith and Reese 1980). Also, depending on the chemical fixation method, some other cellular components may not get fixed and possibly relocate from their original positions (Schnell et al. 2012; Tanaka et al. 2010). The protocol here presented involves the replacement of water by organic solvents and then the sample is

embedded into a plastic resin. Consequential modifications in the ionic composition of the sample are expected, together with a considerable loss of lipids and small, non-fixable metabolites (Donselaar, van et al. 2007). Together with the intrinsic matrix effect present in biological samples (Panuwet et al. 2016), the plastic embedding may also alter the ionization of particular species, unpredictably affecting SIMS measurements. The misinterpretation of these effects should be minimized by treating all experimental and control samples following identical protocols and keeping these aspects in mind to evaluate the type of analysis that can be performed. Additionally, pre-embedding immunolabeling typically requires cell permeabilization, which also affects cell morphology (Melan 1994). Replacing the common used antibodies with nanobodies, which are considerably smaller, can facilitate the immunolabeling of POIs without requiring the permeabilization of the cellular membranes (Fang et al. 2018).

Due to the relatively long time required to obtain a NanoSIMS image, especially when using a high number of pixels ( $\geq 512 \times 512$ ), or even more when we add consecutive layers to increase the signal of low abundance ion channels, we have to expect a certain degree of drift. Minimizing this is an important aspect in this correlative approach, despite most likely it may still require a certain level of image processing to achieve an optimal overlap. For the correlation of the light microscopy image, it is important to count not only with the channel employed to visualize the POI but to also have the autofluorescence image. Since several cell elements such as cellular and nuclear edges, can be clearly visualized in all techniques, they can be used as an internal guide for the overlay of the images, without the need for additional fiducial markers. Nevertheless, the use of special tools such as gold nanoparticles (Urban et al. 2018; Agüi-Gonzalez et al. 2021b), could be useful for increasing the overlay precision since this type of probe could be visualized by all imaging methods, acting not only as a label for specific proteins but as an internal fiducial marker.

Even after optimizing the sample preparation, and due to the fragility of these thin samples, some areas of interest collapsed during the NanoSIMS imaging procedure, both during the initial implantation and the imaging phase. This could be simply avoided by reducing the applied  $\text{Cs}^+$  ion dose. Likewise, to achieve the best possible lateral resolution, the primary ion beam diameter must be limited by selecting the smallest possible aperture, which as a downside also implies the reduction of the primary ion current and a reduction of the secondary ion yield.

The main issue in biological samples in this regard is the abundance of the species of interest, which may differ in several orders of magnitude (e. g.: the natural abundance of  $^{13}\text{C}$  represents only 1.1 % against the 98.9 % for  $^{12}\text{C}$ ) and also their different ionization yields. Therefore, it is required to find a balance between increasing the spatial resolution of the SIMS images and the ability of the instrument to still detect low abundance ion species. Furthermore, we should keep in mind that the average probability of ionization is  $< 10^{-4}$ . Even counting with the high sensitivity of NanoSIMS (in the ppm to ppb range), the emitted number of ions could be insufficient to offer a good signal-to-noise ratio when working at high resolutions (Agüi-Gonzalez et al. 2019). With the NanoSIMS settings that we applied, we obtained a satisfactory spatial resolution of  $\sim 160$  nm, while still obtaining a good signal level from all of the targeted ions. Nonetheless, the low amount of signal registered for some elements, due to the absence of exogenous isotopes in the presented experiments would be overcome with the addition of isotopic labeled biomolecules in future experiments. Alternatively, other studies can simply target elements with higher natural abundance (such as calcium or sodium), in which the primary current could be further reduced obtaining a better lateral resolution and still good signal.

Despite the already discussed limitations, and that the work here presented only aimed to demonstrate the potential of this technology, we have shown that the procedure enables a

better and more specific application of SIMS in biology, by facilitating a straightforward correlation of the SIMS signals to specific cellular structures, observed in electron and fluorescence microscopy. This will enable a variety of future experiments, bringing new insights into cellular composition and metabolic turnover.

## 4.6 FINAL CONCLUSIONS

In this thesis, different approaches and tools have been presented to show how SIMS can be a suitable technique to decipher the chemical composition of biological specimens and the study of metabolic processes, enabling the visualization of a big spectrum of biomolecules at a subcellular resolution level.

As described in aim I of this work, ToF-SIMS was employed to unravel the lipid distribution across the plasma membrane of hippocampal neurons and showed how its composition was modified when changes in the activity of the nerve cells were induced with drugs. Significant alterations of lipid levels, particularly ceramides, PSs, PAs, and TGs, were observed under long incubations with TTX and BIC. These results reinforce the evidence that not only proteins, which are the most common target in biology investigations, are responsible of major modifications related to cellular behavior and suggest that membrane lipids modify their organization to fit to, or even mediating, neuronal and synaptic activity. In addition to promote further studies to address how diverse lipid species are related to physiological and pathological processes, our findings support that mass spectrometry imaging can be also employed to investigate the lipid alterations that are behind several neurodegenerative diseases as well as psychiatric conditions and how to regulate them.

Within the aim II of this thesis, different dual-probes, compatible with both SIMS and light microscopy, were presented. These dual probes enable either the detection of newly synthesized proteins or specific proteins of interest together with the visualization of other species in both negative and positive secondary ion modes. The mass limits of SIMS instruments, especially for NanoSIMS which can only detect monoatomic or small molecules of two or three atoms, require the use of alternative tools to detect the presence of particular species that overpass their detection limits. One of these alternatives is the use of rare stable isotopes (such as  $^{13}\text{C}$  or  $^{15}\text{N}$ ), which can help to visualize the presence of certain analytes. However, the multiple metabolic pathways of the cells reduce the scope of these isotope-labeled precursors and make them helpless to visualize specific species. At best, they provide an overview of certain types of biomolecules. For example, newly synthesized proteins that incorporate isotope-labeled amino acids or the localization of a particular lipid subclass when employing isotope-labeled precursors. Thus, the development of alternative probes that label specific targets is a very valuable achievement in SIMS. Additionally, the probes presented in this thesis can be detected by more than one imaging technique, becoming a considerable advantage since they also serve as internal fiducial markers and help to minimize the localization error between techniques. Furthermore, the diverse spatial resolutions achieved by the correlated modalities could help to resolve the number of probes present within analyzed volumes allowing an absolute quantification of the target while also obtaining an overview of their local chemical environment. In this regard, probes with a higher signal-to-noise ratio like the gold-conjugated nanobodies can facilitate the visualization targets with low abundance. Yet, and until SIMS turns into a more common tool for imaging in biology, the use of dual probes, which are compatible with mass spectrometry and other techniques, not only increases their usability but reinforces the trust in the results offered by SIMS.



Covered by the last two aims, the correlation of SIMS with other imaging techniques was illustrated. We proved that the combination of several imaging techniques maximizes the information obtained through one single experiment and generates synergic results that reach far beyond the scope of the individual data. On the third aim of this thesis, electron microscopy, which has traditionally been employed to analyze the structure and morphology of cells and cellular components was combined with NanoSIMS imaging to investigate the myelin turnover in adult animals. The combination of these two techniques, together with the use of an iKO mouse model, enabled to reveal the insertion sites of the newly synthesized myelin. Likewise, within aim IV, a suitable protocol was presented, showing how thanks to the correlation of NanoSIMS with CLEM and the sum of their capabilities, it was possible to obtain information that was invisible to the individual techniques. To analyze the relative positions and functions of specific proteins, one of the most common options falls onto the correlation of EM with fluorescence microscopy. The addition of SIMS into this equation includes that also the chemical composition of the imaged areas can be decoded. Following a straightforward CLEM-SIMS protocol, we could clearly visualize cellular structures with EM, specific mitochondrial markers with fluorescence microscopy, and analyzing the diverse chemical composition of selected areas of interest with NanoSIMS.

In conclusion, the SIMS imaging approaches, the protocols, and the probes presented in this thesis could help to address from a multimodal and reproducible perspective diverse questions involving the investigation of particular biomolecules, but also to reveal non-targeted information from explorative experiments, obtaining relevant insights that were not accessible through other imaging techniques.

## 5. APPENDIX

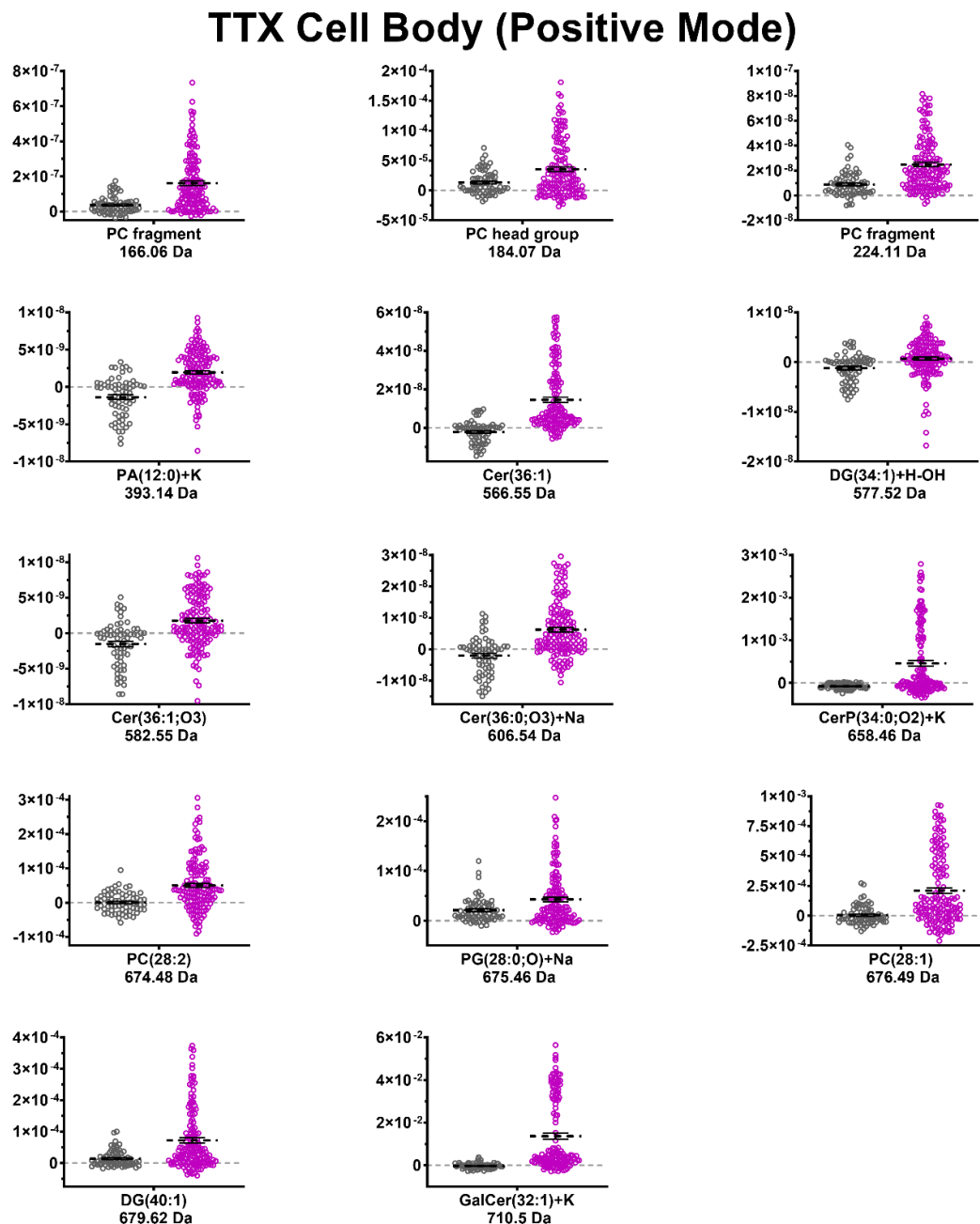


Figure A1. Lipid species that showed significant differences analyzing the CCD on cell bodies from control and TTX treated cell in positive ion mode. Figure extracted from Agüi-Gonzalez et al. (2021a), courtesy of the American Chemical Society.

## TTX Neurite (Positive Mode)

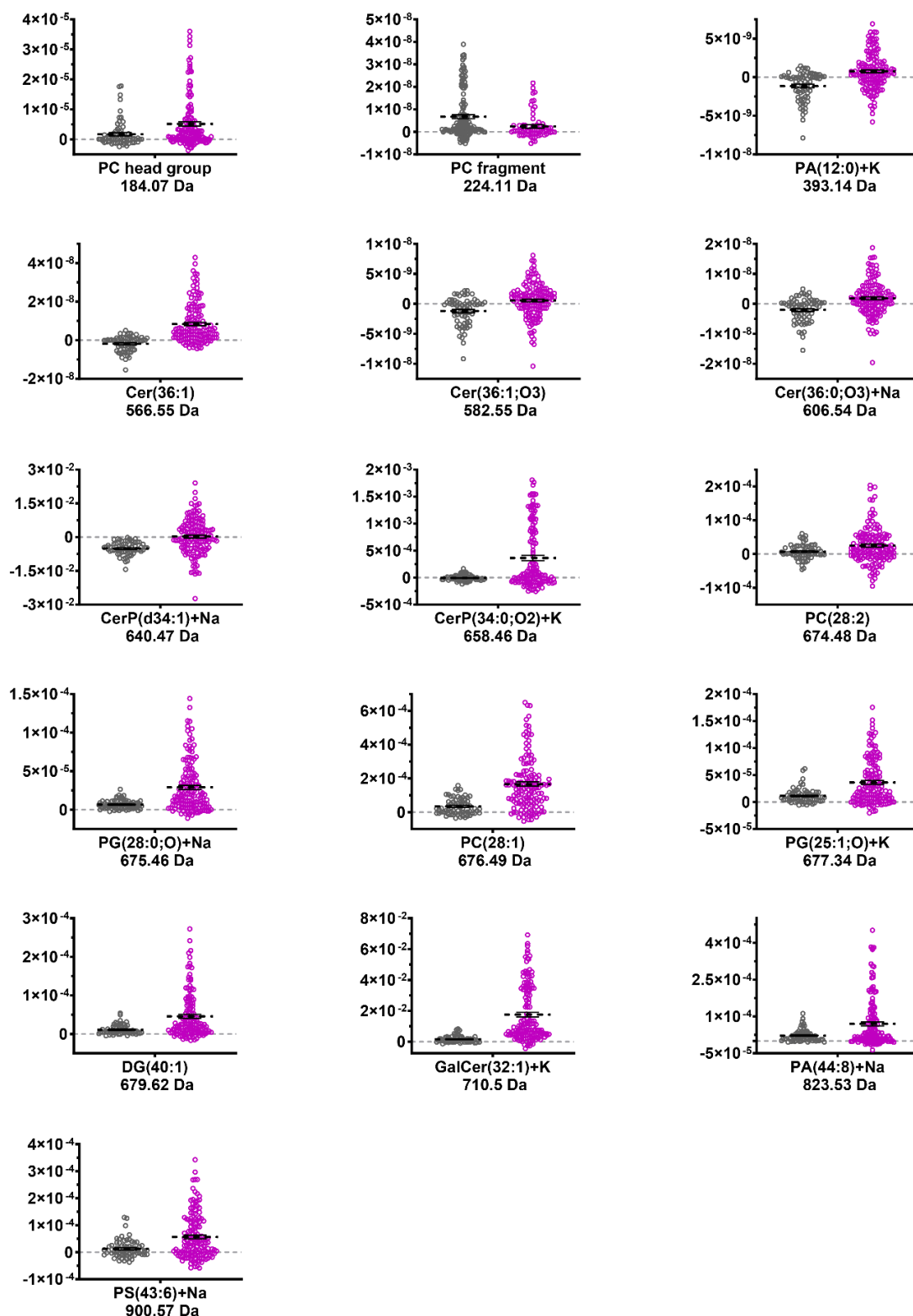


Figure A2. Lipid species that showed significant differences analyzing the CCD on neurites from control and TTX treated cell in positive ion mode. Figure extracted from Agüi-Gonzalez et al. (2021a), courtesy of the American Chemical Society.

### TTX Cell Body (Negative Mode)

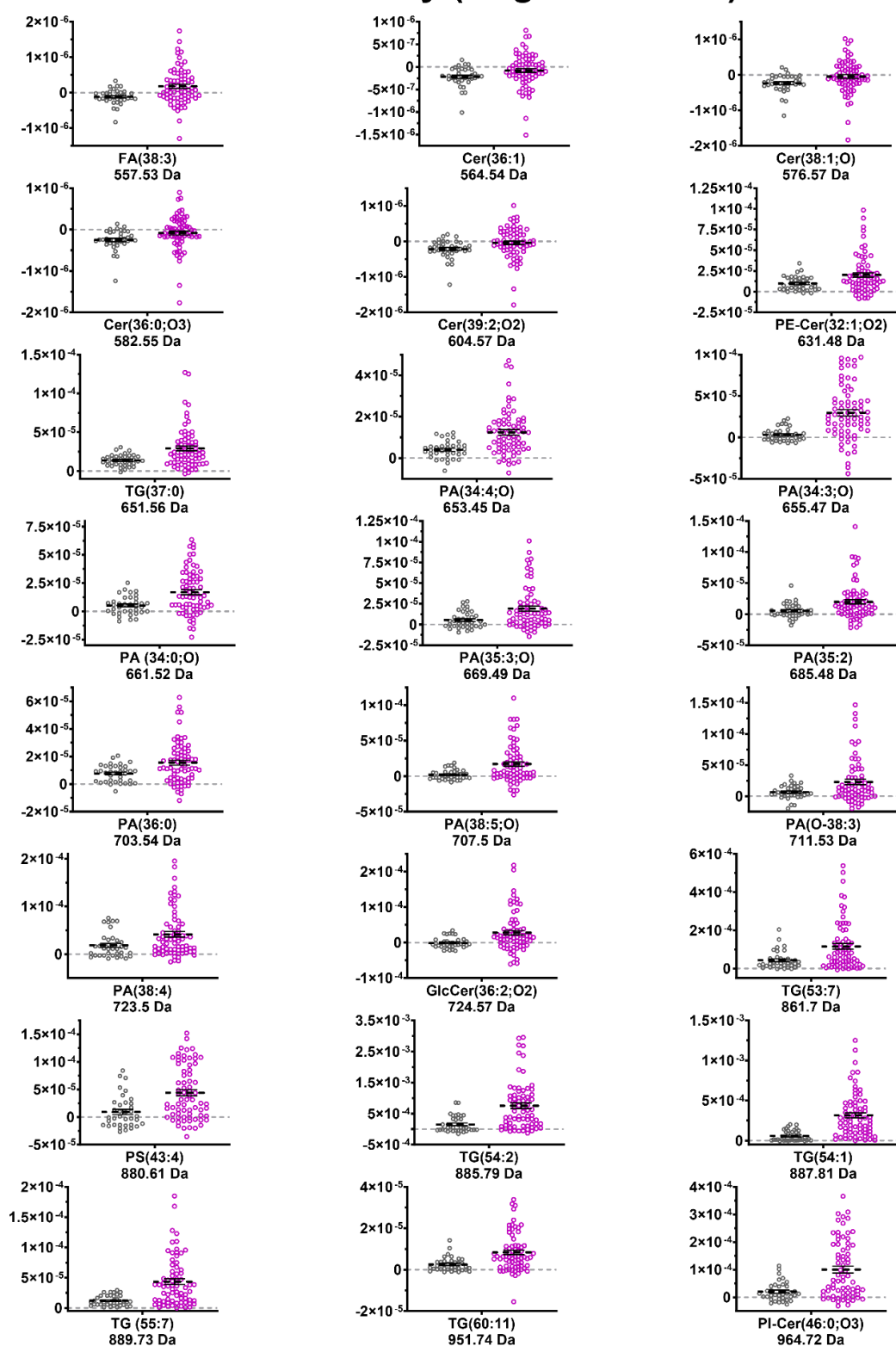


Figure A3. Lipid species that showed significant differences analyzing the CCD on cell bodies from control and TTX treated cell in negative ion mode. Figure extracted from Agüi-Gonzalez et al. (2021a), courtesy of the American Chemical Society.

## TTX Neurite (Negative Mode)

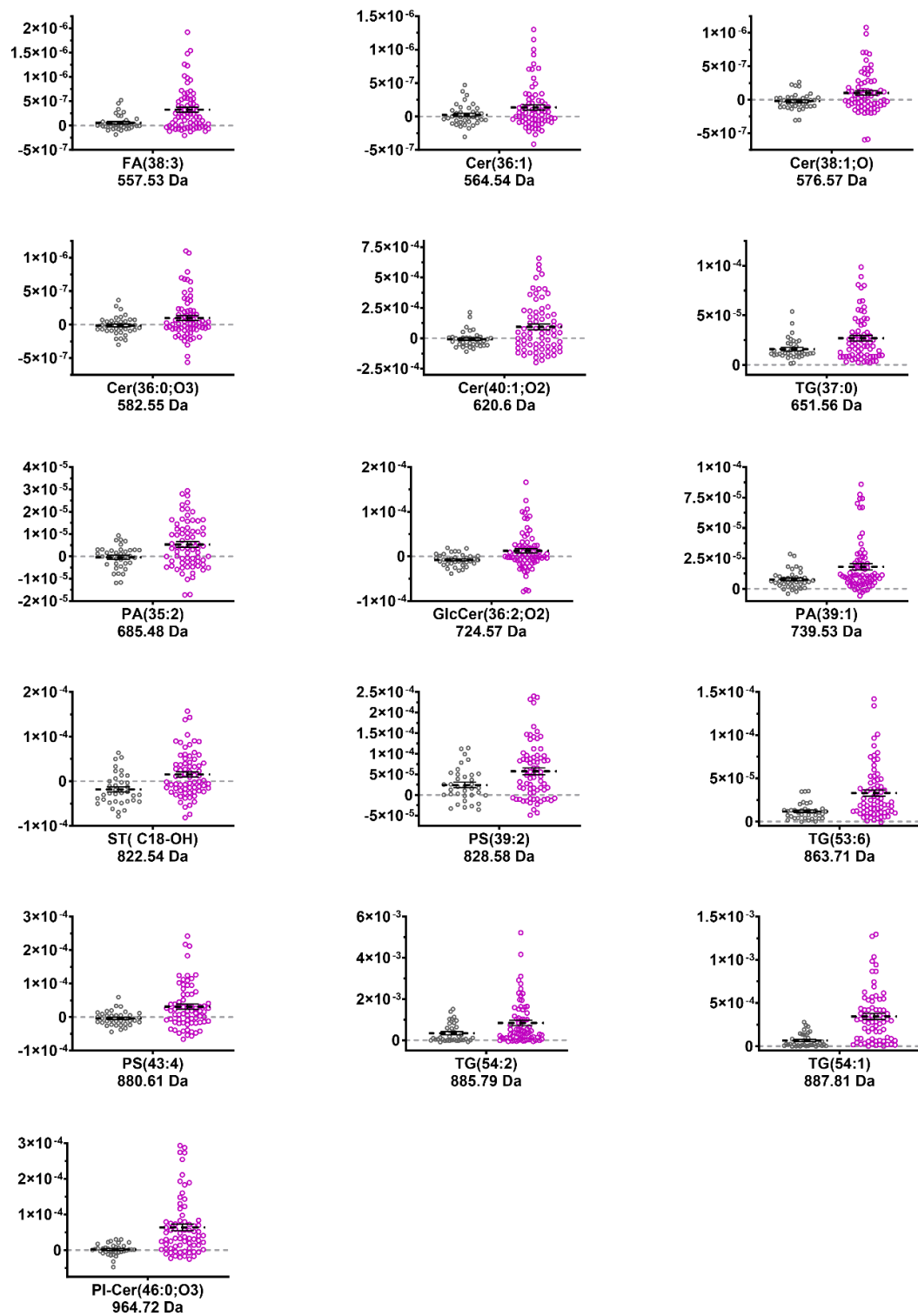


Figure A4. Lipid species that showed significant differences analyzing the CCD on neurites from control and TTX treated cell in negative ion mode. Figure extracted from Agüi-Gonzalez et al. (2021a), courtesy of the American Chemical Society.

## BIC Cell Body (Positive Mode)

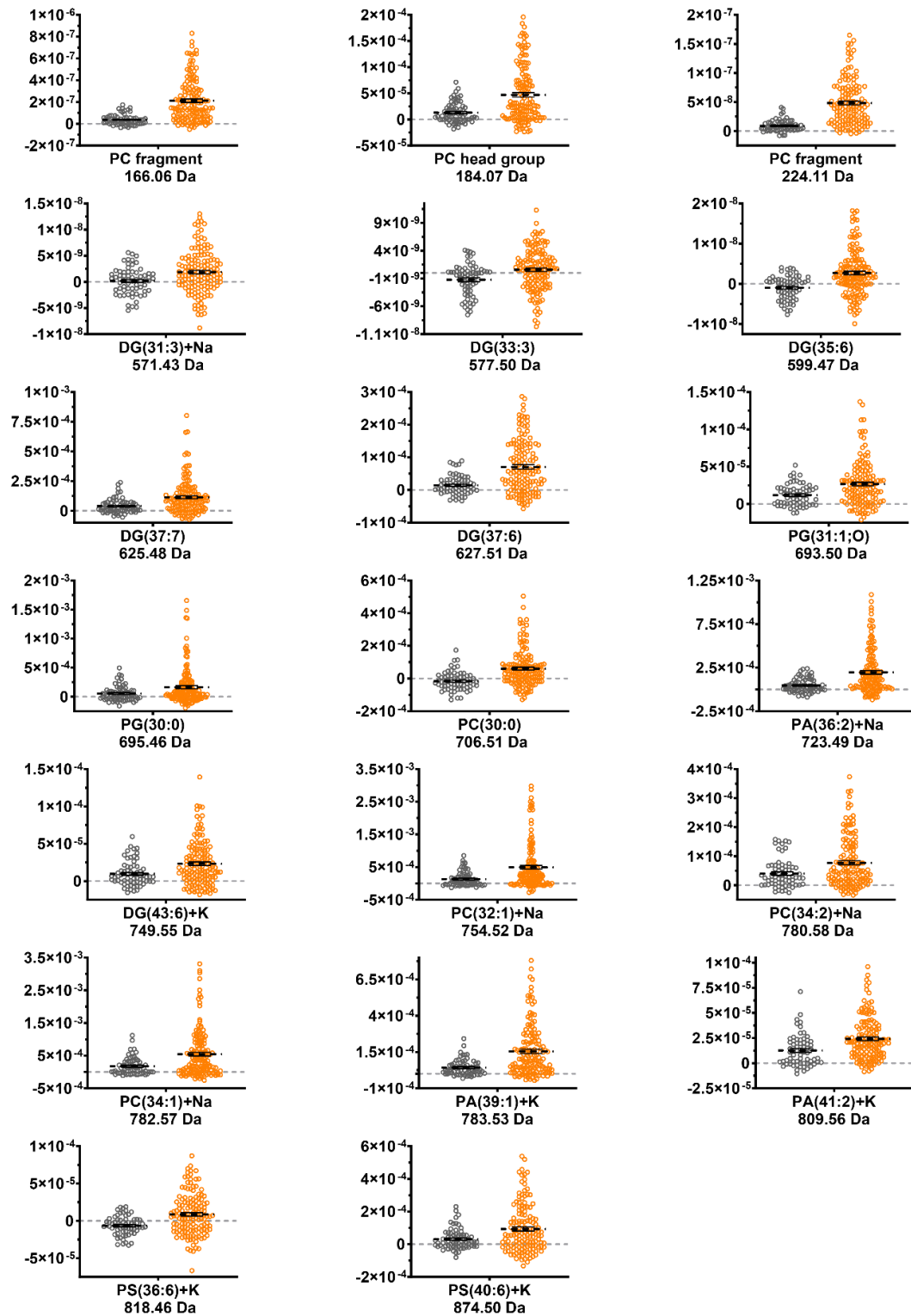


Figure A5. Lipid species that showed significant differences analyzing the CCD on cell bodies from control and BIC treated cell in positive ion mode. Figure extracted from Agüi-Gonzalez et al. (2021a), courtesy of the American Chemical Society.

### BIC Neurite (Positive mode)

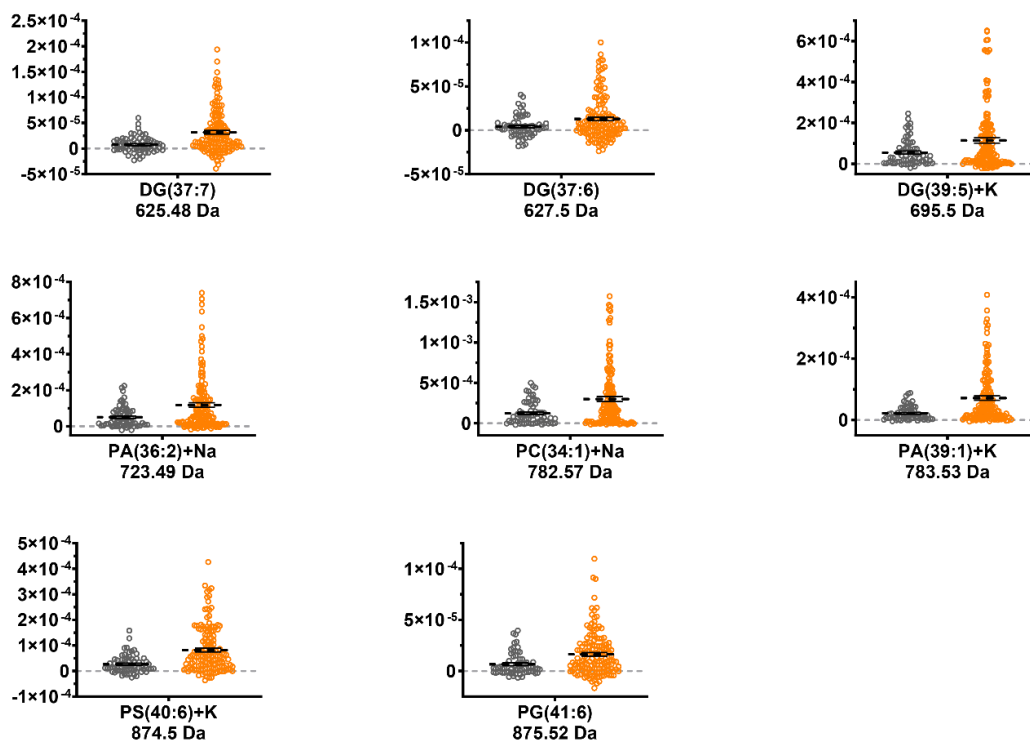


Figure A6. Lipid species that showed significant differences analyzing the CCD on neurites from control and BIC treated cell in positive ion mode. Figure extracted from Agüi-Gonzalez et al. (2021a), courtesy of the American Chemical Society.

## BIC Cell Body (Negative mode)

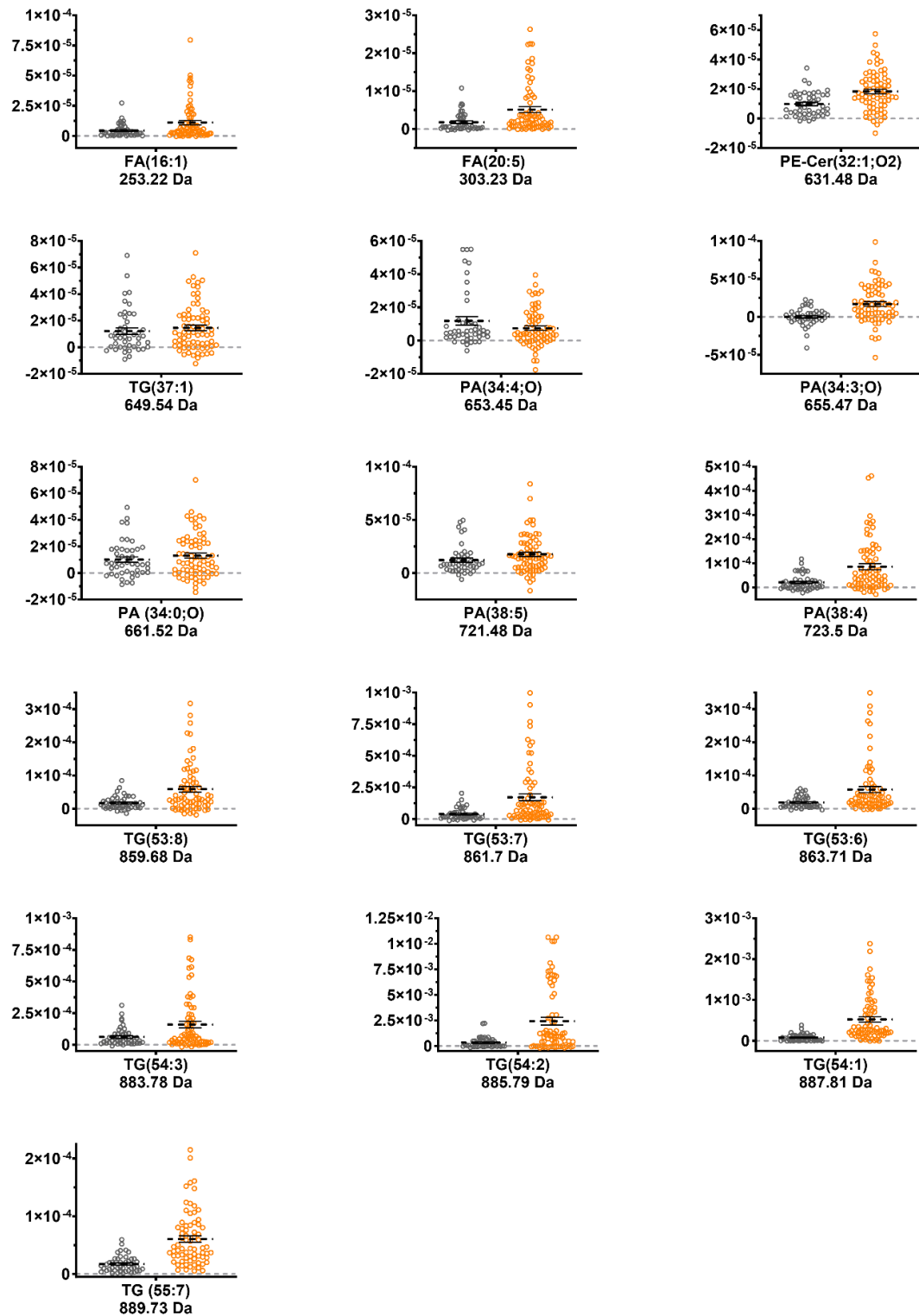


Figure A7. Lipid species that showed significant differences analyzing the CCD on cell bodies from control and BIC treated cell in negative ion mode. Figure extracted from Agüi-Gonzalez et al. (2021a), courtesy of the American Chemical Society.



### BIC Neurite (Negative mode)

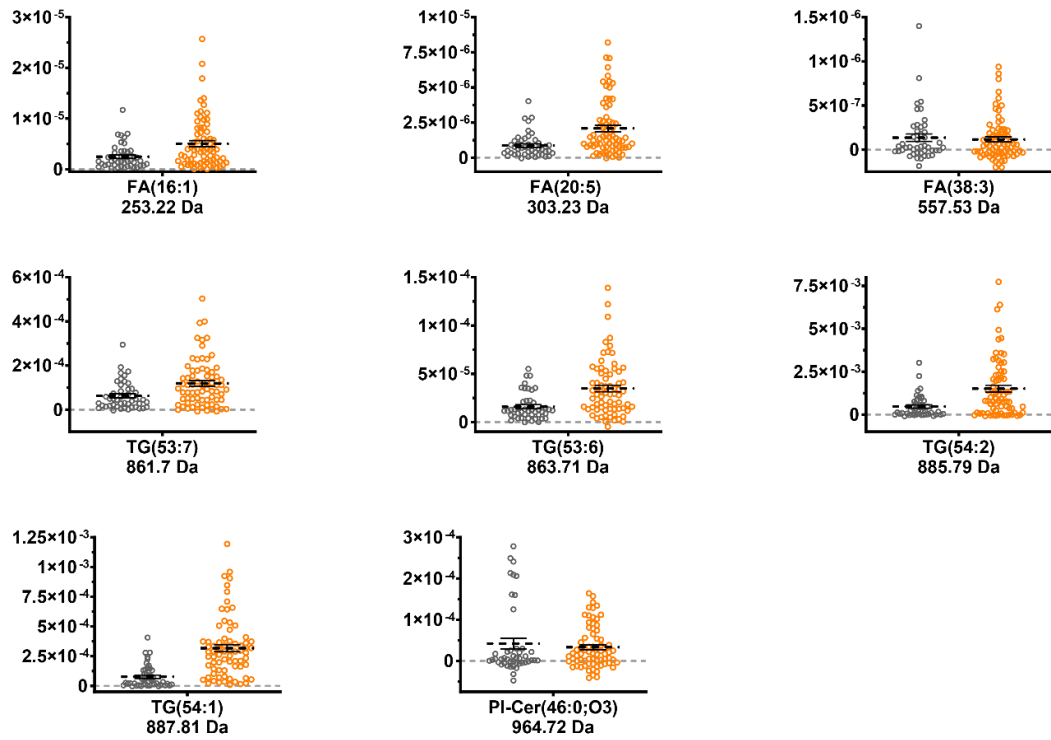


Figure A8. Lipid species that showed significant differences analyzing the CCD on neurites from control and BIC treated cell in negative ion mode. Figure extracted from Agüi-Gonzalez et al. (2021a), courtesy of the American Chemical Society.

**Table S1. Media and solutions used for the preparation of primary hippocampal neurons.**

CMF-HBSS	Calcium-, magnesium-, and bicarbonate-free Hank's balanced salt solution (BSS) buffered with 10 mM HEPES, pH 7.3	
	Component	Source
	10× Hanks' BSS	Invitrogen 14185-052
	1 M HEPES buffer, pH 7.3	Invitrogen 15630-080
Glial Medium	Minimal essential medium (MEM) supplemented with glucose (0.6% wt/vol), penicillin (100 U ml <sup>-1</sup> ), streptomycin (100 µg ml <sup>-1</sup> ), and containing 10% (vol/vol) horse serum	
	Component	Source
	MEM with Earle's salts and L-glutamine	Invitrogen 11095-080
	D-Glucose	Sigma G8769
	Penicillin-streptomycin	Invitrogen 15140-122
	Horse serum	Invitrogen 16050, SAFC Biosciences 12449, or Atlanta Biologicals S12150
Neuronal Plating Medium	MEM supplemented with glucose (0.6% wt/vol) and containing 10% (vol/vol) horse serum or 5% (vol/vol) fetal bovine serum	
	Component	Source
	MEM with Earle's salts and L-glutamine	Invitrogen 11095-080
	D-Glucose	Sigma G8769
	Horse serum or fetal bovine serum	Horse serum, see above; fetal bovine serum, Invitrogen 16000
Neuronal Maintenance Media		
N2 medium	MEM containing the N2 supplement described in ref. 22. It is prepared by combining nine parts MEM supplemented with glucose (0.6% wt/vol) and one part 10× N2 supplement.	
	10× N2 supplement contains the following ingredients prepared in MEM	
	Component	Source
	10 mM sodium pyruvate	Sigma P2256
	1 mM putrescine	Sigma P5780
	0.2 µM progesterone <sup>a</sup>	Sigma P8783
	0.3 µM selenium dioxide <sup>b</sup>	Sigma 200107
	1 mg ml <sup>-1</sup> bovine transferrin	Sigma T1428
	50 µg ml <sup>-1</sup> insulin <sup>c</sup>	Sigma I5500
	Neurobasal/B27 Medium	Prepare according to the manufacturer's instructions by supplementing Neurobasal Medium with GlutaMAX-I and B27 supplement.
Component		Source
Neurobasal Medium		Invitrogen 21103-049
GlutaMAX-I supplement		Invitrogen 35050-061
	B27 serum-free supplement	Invitrogen 17504-044

<sup>a</sup>Dissolve 63 mg progesterone in 100 ml EtOH, then dilute 1:100 in H<sub>2</sub>O to make a 20 mM stock solution.

<sup>b</sup>Dissolve 33 mg SeO<sub>2</sub> in 100 ml H<sub>2</sub>O, then dilute 1:100 in H<sub>2</sub>O to make a 30 µM stock solution.

<sup>c</sup>Dissolve 50 mg insulin in 10 ml 0.01N HCl, made by adding 86 µl concentrated HCl to 100 ml H<sub>2</sub>O.

Table extracted from Kaech and Banker (2006), courtesy of Nature.

## 6. BIBLIOGRAPHY

---

---

Adams KJ, DeBord JD, Fernandez-Lima F (2016): Lipid Specific Molecular Ion Emission as a Function of the Primary Ion Characteristics in TOF-SIMS. *J Vac Sci Technol B* 34, 051804

Agüi-Gonzalez P, Jähne S, Phan NTN (2019): SIMS Imaging in Neurobiology and Cell Biology. *J Anal At Spectrom* 34, 1355–68

Agüi-Gonzalez P, Guobin B, Gomes de Castro MA, Rizzoli SO, Phan NTN (2021a): Secondary Ion Mass Spectrometry Imaging Reveals Changes in the Lipid Structure of the Plasma Membranes of Hippocampal Neurons Following Drugs Affecting Neuronal Activity. *ACS Chem Neurosci* 12, 1542–51

Agüi-Gonzalez P, Dankovich TM, Rizzoli SO, Phan NTN (2021b): Gold-Conjugated Nanobodies for Targeted Imaging Using High-Resolution Secondary Ion Mass Spectrometry. *Nanomaterials* 11, 1797

Alza NP, Conde MA, Scodelaro-Bilbao PG, Salvador GA (2021): Neutral Lipids as Early Biomarkers of Cellular Fate: The Case of  $\alpha$ -Synuclein Overexpression. *Cell Death Dis* 12, 52

Angelo M, Bendall SC, Finck R, Hale MB, Hitzman C, Borowsky AD, Levenson RM, Lowe JB, Liu SD, Zhao S et al. (2014): Multiplexed Ion Beam Imaging of Human Breast Tumors. *Nat Med* 20, 436–42

Arrojo e Drigo R, Lev-Ram V, Tyagi S, Ramachandra R, Deerinck T, Bushong E, Phan S, Orphan V, Lechene C, Ellisman MH et al. (2019): Age Mosaicism across Multiple Scales in Adult Tissues. *Cell Metab* 30, 343-351.e3

Baudry M, Massicotte G, Hauge S (1991): Phosphatidylserine Increases the Affinity of the AMPA/Quisqualate Receptor in Rat Brain Membranes. *Behav Neural Biol* 55, 137–40

Beare-Rogers JL, Dieffenbacher A, Holm J V. (2001): Lexicon of Lipid Nutrition (IUPAC Technical Report). *Pure Appl Chem* 73, 685–744

Benninghoven A (1994): Chemical Analysis of Inorganic and Organic Surfaces and Thin Films by Static Time-of-Flight Secondary Ion Mass Spectrometry (TOF-SIMS). *Angew Chemie Int Ed* 33, 1023–43

Berrueta Razo I, Sheraz S, Henderson A, Lockyer NP, Vickerman JC (2015): Mass Spectrometric Imaging of Brain Tissue by Time-of-Flight Secondary Ion Mass Spectrometry - How Do Polyatomic Primary Beams C 60 + , Ar 2000 + , Water-Doped Ar 2000 + and (H 2 O) 6000 + Compare? *Rapid Commun Mass Spectrom* 29, 1851–62

Bittman R: Glycerolipids: Chemistry. In: Gordon C K Roberts (Eds.): *Encyclopedia of Biophysics*. Springer, Berlin/Heidelberg 2013, 907–14

Blitterswijk WJ van, Luit AH van der, Veldman RJ, Verheij M, Borst J (2003): Ceramide: Second Messenger or Modulator of Membrane Structure and Dynamics? *Biochem J* 369, 199–211

Boxer SG, Kraft ML, Weber PK (2009): Advances in Imaging Secondary Ion Mass Spectrometry for Biological Samples. *Annu Rev Biophys* 38, 53–74

Bozzatello P, Brignolo E, Grandi E De, Bellino S (2016): Supplementation with Omega-3 Fatty Acids in Psychiatric Disorders: A Review of Literature Data. *J Clin Med* 5, 67

Calvano CD, Ventura G, Sardanelli AMM, Savino L, Losito I, De-Michele G, Palmisano F, Cataldi TRI (2019): Searching for Potential Lipid Biomarkers of Parkinson's Disease in Parkin-Mutant Human Skin Fibroblasts by HILIC-ESI-MS/MS: Preliminary Findings. *Int J Mol Sci* 20, 3341

Chazotte B (2011): Labeling Mitochondria with MitoTracker Dyes. *Cold Spring Harb Protoc* 8, 990-2

- Chernushevich IV, Loboda AV, Thomson BA (2001): An Introduction to Quadrupole-Time-of-Flight Mass Spectrometry. *J Mass Spectrom* 36, 849–65
- Cremesti AE, Goni FM, Kolesnick R (2002): Role of Sphingomyelinase and Ceramide in Modulating Rafts: Do Biophysical Properties Determine Biologic Outcome? *FEBS Lett* 531, 47–53
- Cunha MML da, Trepout S, Messaoudi C, Wu TD, Ortega R, Guerquin-Kern JL, Marco S (2016): Overview of Chemical Imaging Methods to Address Biological Questions. *Micron* 84, May 23–36
- Devaux PF, Herrmann A, Ohlwein N, Kozlov MM (2008): How Lipid Flippases Can Modulate Membrane Structure. *Biochim Biophys Acta - Biomembr* 1778, 1591–1600
- Dickson EJ (2019): Recent Advances in Understanding Phosphoinositide Signaling in the Nervous System. *F1000Res* 8, 278
- Dieterich DC, Hodas JJJ, Gouzer G, Shadrin IY, Ngo JT, Triller A, Tirrell DA, Schuman EM (2010): In Situ Visualization and Dynamics of Newly Synthesized Proteins in Rat Hippocampal Neurons. *Nat Neurosci* 13, 897–905
- Donselaar E van, Posthuma G, Zeuschner D, Humbel BM, Slot JW (2007): Immunogold Labeling of Cryosections from High-Pressure Frozen Cells. *Traffic* 8, 471–85
- Dörrbaum AR, Kochen L, Langer JD, Schuman EM (2018): Local and Global Influences on Protein Turnover in Neurons and Glia. *Elife* 7, e34202
- Eachambadi RT, Boschker HTS, Franquet A, Spampinato V, Hidalgo-Martinez S, Valcke R, Meysman FJR, Manca JV. (2021): Enhanced Laterally Resolved ToF-SIMS and AFM Imaging of the Electrically Conductive Structures in Cable Bacteria. *Anal Chem* 93, 7226–34
- Eehalt R, Keller P, Haass C, Thiele C, Simons K (2003): Amyloidogenic Processing of the Alzheimer  $\beta$ -Amyloid Precursor Protein Depends on Lipid Rafts. *J Cell Biol* 160, 113–23
- El-Bacha T, and Torres AG: Phospholipids: Physiology. In: Caballero B, Finglas PM, Toldrá F (Eds.): *Encyclopedia of Food and Health*. Elsevier, Amsterdam 2016
- Fahy E, Subramaniam S, Brown HA, Glass CK, Merrill AH, Murphy RC, Raetz CRH, Russell DW, Seyama Y, Shaw W et al. (2005): A Comprehensive Classification System for Lipids. *J Lipid Res* 46, 839–61
- Fahy E, Subramaniam S, Murphy RC, Nishijima M, Raetz CRH, Shimizu T, Spener F, Meer G van, Wakelam MJO, Dennis EA (2009): Update of the LIPID MAPS Comprehensive Classification System for Lipids. *J Lipid Res* 50, S9–14
- Fahy E, Cotter D, Sud M, Subramaniam S (2011): Lipid Classification, Structures and Tools. *Biochim Biophys Acta - Mol Cell Biol Lipids* 1811, 637–47
- Fang T, Lu X, Berger D, Gmeiner C, Cho J, Schalek R, Ploegh H, Lichtman J (2018): Nanobody Immunostaining for Correlated Light and Electron Microscopy with Preservation of Ultrastructure. *Nat Methods* 15, 1029–32
- Farooqui AA, Horrocks LA, Farooqui T (2000): Glycerophospholipids in Brain: Their Metabolism, Incorporation into Membranes, Functions, and Involvement in Neurological Disorders. *Chem Phys Lipids* 106, 1–29
- Fisher GL, Hammond JS, Larson PE, Bryan SR, Heeren RMA (2016): Parallel Imaging MS/MS TOF-SIMS Instrument. *J Vac Sci Technol B* 34, 03H126
- Fletcher JS (2015): Latest Applications of 3D ToF-SIMS Bio-Imaging. *Biointerphases* 10, 018902
- Fletcher JS, Vickerman JC (2010): A New SIMS Paradigm for 2D and 3D Molecular Imaging of Bio-Systems. *Anal Bioanal Chem* 396, 85–104

- Fletcher JS, Lockyer NP, Vaidyanathan S, Vickerman JC (2007): TOF-SIMS 3D Biomolecular Imaging of *Xenopus Laevis* Oocytes Using Buckminsterfullerene (C<sub>60</sub>) Primary Ions. *Anal Chem* 79, 2199–2206
- Fletcher JS, Rabbani S, Henderson A, Blenkinsopp P, Thompson SP, Lockyer NP, Vickerman JC (2008a): A New Dynamic in Mass Spectral Imaging of Single Biological Cells. *Anal Chem* 80, 9058–64
- Fletcher JS, Henderson A, Biddulph GX, Vaidyanathan S, Lockyer NP, Vickerman JC (2008b): Uncovering New Challenges in Bio-Analysis with ToF-SIMS. *Appl Surf Sci* 255, 1264–70
- Fornai L, Angelini A, Klinkert I, Giskes F, Kiss A, Eijkel G, Hove EAAA, Klerk LA, Fedrigo M, Pieraccini G et al. (2012): Three-Dimensional Molecular Reconstruction of Rat Heart with Mass Spectrometry Imaging. *Anal Bioanal Chem* 404, 2927–38
- Fornasiero EF, Mandad S, Wildhagen H, Alevra M, Rammner B, Keihani S, Opazo F, Urban I, Ischebeck T, Sakib MS et al. (2018): Precisely Measured Protein Lifetimes in the Mouse Brain Reveal Differences across Tissues and Subcellular Fractions. *Nat Commun* 9, 4230
- Frisz JF, Lou K, Klitzing HA, Hanafin WP, Lizunov V, Wilson RL, Carpenter KJ, Kim R, Hutcheon ID, Zimmerberg J et al. (2013): Direct Chemical Evidence for Sphingolipid Domains in the Plasma Membranes of Fibroblasts. *Proc Natl Acad Sci* 110, E613–22
- Gardiner AT, Naydenova K, Castro-Hartmann P, Nguyen-Phan TC, Russo CJ, Sader K, Hunter CN, Cogdell RJ, Qian P (2021): The 2.4 Å Cryo-EM Structure of a Heptameric Light-Harvesting 2 Complex Reveals Two Carotenoid Energy Transfer Pathways. *Sci Adv* 7, eabe4650
- González de San Román E, Manuel I, Giralt MT, Ferrer I, Rodríguez-Puertas R (2017): Imaging Mass Spectrometry (IMS) of Cortical Lipids from Preclinical to Severe Stages of Alzheimer's Disease. *Biochim Biophys Acta - Biomembr* 1859, 1604–14
- Gorman BL, Kraft ML (2020): High-Resolution Secondary Ion Mass Spectrometry Analysis of Cell Membranes. *Anal Chem* 92, 1645–52
- Guerquin-Kern J-L, Wu T-D, Quintana C, Croisy A (2005): Progress in Analytical Imaging of the Cell by Dynamic Secondary Ion Mass Spectrometry (SIMS Microscopy). *Biochim Biophys Acta - Gen Subj* 1724, 228–38
- Gyngard F, Steinhauser ML (2019): Biological Explorations with Nanoscale Secondary Ion Mass Spectrometry. *J Anal At Spectrom* 34, 1534–45
- Hanrieder J, Phan NTN, Kurczy ME, Ewing AG (2013a): Imaging Mass Spectrometry in Neuroscience. *ACS Chem Neurosci* 4, 666–79
- Hanrieder J, Malmberg P, Lindberg OR, Fletcher JS, Ewing AG (2013b): Time-of-Flight Secondary Ion Mass Spectrometry Based Molecular Histology of Human Spinal Cord Tissue and Motor Neurons. *Anal Chem* 85, 8741–48
- Harayama T, Riezman H (2018): Understanding the Diversity of Membrane Lipid Composition. *Nat Rev Mol Cell Biol* 19, 281–96
- Hashimoto M, and Hossain S : Fatty Acids: From Membrane Ingredients to Signaling Molecules. In: Viduranga Waisundara (Eds.): *Biochemistry and Health Benefits of Fatty Acids*. IntechOpen, London 2018, 1–15
- He C, Fong LG, Young SG, Jiang H (2017): NanoSIMS Imaging: An Approach for Visualizing and Quantifying Lipids in Cells and Tissues. *J Investig Med* 65, 669–72
- He C, Weston TA, Jung RS, Heizer P, Larsson M, Hu X, Allan CM, Tontonoz P, Reue K, Beigneux AP et al. (2018): NanoSIMS Analysis of Intravascular Lipolysis and Lipid Movement across Capillaries and into Cardiomyocytes. *Cell Metab* 27, 1055-1066.e3

- Heo S, Diering GH, Na CH, Nirujogi RS, Bachman JL, Pandey A, Haganir RL (2018): Identification of Long-Lived Synaptic Proteins by Proteomic Analysis of Synaptosome Protein Turnover. *Proc Natl Acad Sci* 115, E3827–36
- Holthuis JCM, Menon AK (2014): Lipid Landscapes and Pipelines in Membrane Homeostasis. *Nature* 510, 48–57
- McNaught AD and Wilkinson (Eds.): IUPAC: The IUPAC Compendium of Chemical Terminology (the "Gold Book"). 2<sup>nd</sup> edition; Blackwell Scientific Publications, Oxford 2019
- Jähne S, Mikulasch F, Heuer HGH, Truckenbrodt S, Agüi-Gonzalez P, Grewe K, Vogts A, Rizzoli SO, Priesemann V (2021): Presynaptic Activity and Protein Turnover Are Correlated at the Single-Synapse Level. *Cell Rep* 34, 108841
- Jiang H, Passarelli MK, Munro PMG, Kilburn MR, West A, Dollery CT, Gilmore IS, Rakowska PD (2017): High-Resolution Sub-Cellular Imaging by Correlative NanoSIMS and Electron Microscopy of Amiodarone Internalisation by Lung Macrophages as Evidence for Drug-Induced Phospholipidosis. *Chem Commun* 53, 1506–9
- Johnston GAR (2013): Advantages of an Antagonist: Bicuculline and Other GABA Antagonists. *Br J Pharmacol* 169, 328–36
- Kabatas S, Vreja IC, Saka SK, Höschel C, Kröhnert K, Opazo F, Rizzoli SO, Diederichsen U (2015): A Contamination-Insensitive Probe for Imaging Specific Biomolecules by Secondary Ion Mass Spectrometry. *Chem Commun* 51, 13221–24
- Kabatas S, Agüi-Gonzalez P, Saal K, Jähne S, Opazo F, Rizzoli SO, Phan NTN (2019a): Boron-Containing Probes for Non-optical High-Resolution Imaging of Biological Samples. *Angew Chemie Int Ed* 58, 3438–43
- Kabatas S, Agüi-Gonzalez P, Hinrichs R, Jähne S, Opazo F, Diederichsen U, Rizzoli SO, Phan NTN (2019b): Fluorinated Nanobodies for Targeted Molecular Imaging of Biological Samples Using Nanoscale Secondary Ion Mass Spectrometry. *J Anal At Spectrom* 34, 1083–87
- Kaech S, Banker G (2006): Culturing Hippocampal Neurons. *Nat Protoc* 1, 2406–15
- Kanno K, Wu MK, Scapa EF, Roderick SL, Cohen DE (2007): Structure and Function of Phosphatidylcholine Transfer Protein (PC-TP)/StarD2. *Biochim Biophys Acta - Mol Cell Biol Lipids* 1771, 654–62
- Kasimova MA, Tarek M, Shaytan AK, Shaitan K V., Delemotte L (2014): Voltage-Gated Ion Channel Modulation by Lipids: Insights from Molecular Dynamics Simulations. *Biochim Biophys Acta - Biomembr* 1838, 1322–31
- Kikuma J, Imai H (2001): Yield Enhancement Effect of Low-Energy O<sub>2</sub><sup>+</sup> Ion Bombardment in Ga Focused Ion Beam SIMS. *Surf Interface Anal* 31, 901–4
- Kim HY, Huang BX, Spector AA (2014): Phosphatidylserine in the Brain: Metabolism and Function. *Prog Lipid Res* 56, *Prog Lipid Res* 56, 1–18
- Kim S, Chen J, Cheng T, Gindulyte A, He J, He S, Li Q, Shoemaker BA, Thiessen PA, Yu B et al. (2021): PubChem in 2021: New Data Content and Improved Web Interfaces. *Nucleic Acids Res* 49, D1388–95
- Kim T, Gondré-Lewis MC, Arnaoutova I, Loh YP (2006): Dense-Core Secretory Granule Biogenesis 21, 124–33
- Kind T, Liu KH, Lee DY, Defelice B, Meissen JK, Fiehn O (2013): LipidBlast in Silico Tandem Mass Spectrometry Database for Lipid Identification. *Nat Methods* 10, 755–58
- Kita NT, Ushikubo T, Fu B, Valley JW (2009): High Precision SIMS Oxygen Isotope Analysis and the Effect of Sample Topography. *Chem Geol* 264, 43–57

- Kollmer F. (2004): Cluster Primary Ion Bombardment of Organic Materials. *Appl Surf Sci* 231–232, 153–58
- Kollmer F, Paul W, Krehl M, Niehuis E (2013): Ultra High Spatial Resolution SIMS with Cluster Ions - Approaching the Physical Limits. *Surf Interface Anal* 45, 312–14
- Kraft ML (2017): Sphingolipid Organization in the Plasma Membrane and the Mechanisms That Influence It. *Front Cell Dev Biol* 4, 154
- Kraft ML, Klitzing HA (2014): Imaging Lipids with Secondary Ion Mass Spectrometry. *Biochim Biophys Acta* 1841, 1108–19
- Kurczyk ME, Piehowski PD, Parry SA, Jiang M, Chen G, Ewing AG, Winograd N (2008): Which Is More Important in Bioimaging SIMS Experiments—The Sample Preparation or the Nature of the Projectile? *Appl Surf Sci* 255, 1298–1304
- Lago J, Rodríguez L, Blanco L, Vieites J, Cabado A (2015): Tetrodotoxin, an Extremely Potent Marine Neurotoxin: Distribution, Toxicity, Origin and Therapeutical Uses. *Mar Drugs* 13, 6384–6406
- Lanekoff I, Kurczyk ME, Adams KL, Malm J, Karlsson R, Sjövall P, Ewing AG (2011): An in Situ Fracture Device to Image Lipids in Single Cells Using ToF-SIMS. *Surf Interface Anal* 43, 257–60
- Lange F, Agüi-Gonzalez P, Riedel D, Phan NTN, Jakobs S, Rizzoli SO (2021): Correlative Fluorescence Microscopy, Transmission Electron Microscopy and Secondary Ion Mass Spectrometry (CLEM-SIMS) for Cellular Imaging. *PLoS One* 16, e0240768
- Lauwers E, Goodchild R, Verstreken P (2016): Membrane Lipids in Presynaptic Function and Disease. *Neuron* 90, 11–25
- Leventis PA, Grinstein S (2010): The Distribution and Function of Phosphatidylserine in Cellular Membranes. *Annu Rev Biophys* 39, 407–27
- Lovrić J, Dunevall J, Larsson A, Ren L, Andersson S, Meibom A, Malmberg P, Kurczyk ME, Ewing AG (2017): Nano Secondary Ion Mass Spectrometry Imaging of Dopamine Distribution Across Nanometer Vesicles. *ACS Nano* 11, 3446–55
- MacDonald GE, Lada RR, Caldwell CD, Udenigwe C, MacDonald MT (2019): Potential Roles of Fatty Acids and Lipids in Postharvest Needle Abscission Physiology. *Am J Plant Sci* 10, 1069–89
- Magee CW, Honig RE and Evans CA: Depth Profiling by SIMS: Depth Resolution, Dynamic Range and Sensitivity B.T. In: Benninghoven A, Giber J, László J, Riedel M, and Werner HW (Eds.) *Second Ion Mass Spectrometry SIMS III*, Springer, Berlin/Heidelberg 1982, 172–85
- Maidorn M, Olichon A, Rizzoli SO, Opazo F (2019): Nanobodies Reveal an Extra-Synaptic Population of SNAP-25 and Syntaxin 1A in Hippocampal Neurons. *MAbs* 11, 305–21
- Maier MA, Jayaraman M, Matsuda S, Liu J, Barros S, Querbes W, Tam YK, Ansell SM, Kumar V, Qin J et al. (2013): Biodegradable Lipids Enabling Rapidly Eliminated Lipid Nanoparticles for Systemic Delivery of RNAi Therapeutics. *Mol Ther* 21, 1570–78
- Malherbe J, Penen F, Isaure M-P, Frank J, Hause G, Dobritsch D, Gontier E, Horr ard F, Hillion F, Schauml ffel D (2016): A New Radio Frequency Plasma Oxygen Primary Ion Source on Nano Secondary Ion Mass Spectrometry for Improved Lateral Resolution and Detection of Electropositive Elements at Single Cell Level. *Anal Chem* 88, 7130–36
- Mart nez-Gardeazabal J, Gonz lez de San Rom n E, Moreno-Rodr guez M, Llorente-Ovejero A, Manuel I, Rodr guez-Puertas R (2017): Lipid Mapping of the Rat Brain for Models of Disease. *Biochim Biophys Acta - Biomembr* 1859, 1548–57
- Massonnet P, Heeren RMA (2019): A Concise Tutorial Review of TOF-SIMS Based Molecular and Cellular Imaging. *J Anal At Spectrom* 34, 2217–28

- Melan MA: Overview of Cell Fixation and Permeabilization. In: Javois LC (Eds.): *Immunocytochemical Methods and Protocols*. Humana Press, New Jersey 1994, vol 34
- Mencarelli C, Martinez-Martinez P (2013): Ceramide Function in the Brain: When a Slight Tilt Is Enough. *Cell Mol Life Sci* 70, 181–203
- Merrill CB, Basit A, Armirotti A, Jia Y, Gall CM, Lynch G, Piomelli D (2017): Patch Clamp-Assisted Single Neuron Lipidomics. *Sci Rep* 7, 5318
- Meschkat M, Steyer AM, Weil M-T, Kusch K, Jahn O, Piepkorn L, Agüi-Gonzalez P, Phan NTN, Ruhwedel T, Sadowski B et al. (2022): White Matter Integrity in Mice Requires Continuous Myelin Synthesis at the Inner Tongue. *Nat Commun* 13, 1163
- Michalowski PP, Caban P, Baranowski J (2019): Secondary Ion Mass Spectrometry Investigation of Carbon Grain Formation in Boron Nitride Epitaxial Layers with Atomic Depth Resolution. *J Anal At Spectrom* 34, 848–53
- Möbius W, Posthuma G (2019): Sugar and Ice: Immunoelectron Microscopy Using Cryosections According to the Tokuyasu Method. *Tissue Cell* 57, 90–102
- Morphew MK : 3D Immunolocalization with Plastic Sections. In: *Methods Cell Biology*, Academic Press, Massachusetts 2007, vol 79, 493–513
- Mouritsen OG : *Life — As a Matter of Fat. The Emerging Science of Lipidomics*. Springer Berlin, Heidelberg 2005
- Murray J, Cuccia L, Ianoul A, Cheetham JJ, Johnston LJ (2004): Imaging the Selective Binding of Synapsin to Anionic Membrane Domains. *ChemBioChem* 5, 1489–94
- Muyldermans S (2013): Nanobodies: Natural Single-Domain Antibodies. *Annu Rev Biochem* 82, 775–97
- Neikov OD, and Yefimov NA: Powder Characterization and Testing. In: Oleg D. Neikov, Stanislav S. Naboychenko, Nikolay A. Yefimov (Eds.): *Handb. Non-Ferrous Met. Powders*. 2<sup>nd</sup> edition; Elsevier Amsterdam 2019, 3–62
- Nuñez J, Renslow R, Cliff JB, Anderton CR (2018): NanoSIMS for Biological Applications: Current Practices and Analyses. *Biointerphases* 13, 03B301
- Nygren H, Börner K, Malmberg P, Hagenhoff B (2006): Localization of Cholesterol in Rat Cerebellum with Imaging TOF-SIMS. *Appl Surf Sci* 252, 6975–81
- Opazo F, Levy M, Byrom M, Schäfer C, Geisler C, Groemer TW, Ellington AD, Rizzoli SO (2012): Aptamers as Potential Tools for Super-Resolution Microscopy. *Nat Methods* 9, 938–39
- Oran U: *Surface Chemical Characterization of Plasma-Chemically Deposited Polymer Films by Time of Flight Static Secondary Ion Mass Spectrometry*. Dissertation. Freie Universität Berlin, 2005
- Pacholski ML, Winograd N (1999): Imaging with Mass Spectrometry. *Chem Rev* 99, 2977–3006
- Panuwet P, Hunter RE, D'Souza PE, Chen X, Radford SA, Cohen JR, Marder ME, Kartavenka K, Ryan PB, Barr DB (2016): Biological Matrix Effects in Quantitative Tandem Mass Spectrometry-Based Analytical Methods: Advancing Biomonitoring. *Crit Rev Anal Chem* 46, 93–105
- Passarelli MK, Ewing AG, Winograd N (2013): Single-Cell Lipidomics: Characterizing and Imaging Lipids on the Surface of Individual *Aplysia Californica* Neurons with Cluster Secondary Ion Mass Spectrometry. *Anal Chem* 85, 2231–38
- Passarelli MK, Pirkl A, Moellers R, Grinfeld D, Kollmer F, Havelund R, Newman CF, Marshall PS, Arlinghaus H, Alexander MR et al. (2017): The 3D OrbiSIMS—Label-Free Metabolic Imaging with Subcellular Lateral Resolution and High Mass-Resolving Power. *Nat Methods* 14, 1175–83



- Passarelli MK, Winograd N (2011): Lipid Imaging with Time-of-Flight Secondary Ion Mass Spectrometry (ToF-SIMS). *Biochim Biophys Acta - Mol Cell Biol Lipids* 1811, 976–90
- Paul-Gilloteaux P, Heiligenstein X, Belle M, Domart M-C, Larijani B, Collinson L, Raposo G, Salamero J (2017): EC-CLEM: Flexible Multidimensional Registration Software for Correlative Microscopies. *Nat Methods* 14, 102–3
- Phan NTN, Munem M, Ewing AG, Fletcher JS (2017): MS/MS Analysis and Imaging of Lipids across *Drosophila* Brain Using Secondary Ion Mass Spectrometry. *Anal Bioanal Chem* 409, 3923–32
- Philipsen MH, Phan NTN, Fletcher JS, Malmberg P, Ewing AG (2018): Mass Spectrometry Imaging Shows Cocaine and Methylphenidate Have Opposite Effects on Major Lipids in *Drosophila* Brain. Research-article. *ACS Chem Neurosci* 9, 1462–68
- Piomelli D, Astarita G, Rapaka R (2007): A Neuroscientist's Guide to Lipidomics. *Nat Rev Neurosci* 8, 743–54
- Politzer P, Murray JS (2018): Electronegativity—a Perspective. *J Mol Model* 24, 214
- Popczun NJ, Breuer L, Wucher A, Winograd N (2017): On the SIMS Ionization Probability of Organic Molecules. *J Am Soc Mass Spectrom* 28, 1182–91
- Poveda JA, Giudici AM, Renart ML, Molina ML, Montoya E, Fernández-Carvajal A, Fernández-Ballester G, Encinar JA, González-Ros JM (2014): Lipid Modulation of Ion Channels through Specific Binding Sites. *Biochim Biophys Acta - Biomembr* 1838, 1560–67
- Priebe A, Xie T, Bürki G, Pethö L, Michler J (2020): The Matrix Effect in TOF-SIMS Analysis of Two-Element Inorganic Thin Films. *J Anal At Spectrom* 35, 1156–66
- Puchkov D, Haucke V (2013): Greasing the Synaptic Vesicle Cycle by Membrane Lipids. *Trends Cell Biol* 23, 493–503
- Rabbani S, Barber A, Fletcher JS, Lockyer NP and Vickerman JC (2013): Enhancing Secondary Ion Yields in Time of Flight-Secondary Ion Mass Spectrometry Using Water Cluster Primary Beams. *Anal. Chem.* 85, 5654–58
- Raben DM, Barber CN (2017): Phosphatidic Acid and Neurotransmission. *Adv Biol Regul* 63, 15–21
- Ren L, Dowlatshahi Pour M, Malmberg P, Ewing AG (2019): Altered Lipid Composition of Secretory Cells Following Exposure to Zinc Can Be Correlated to Changes in Exocytosis. *Chem – A Eur J* 25, 5406–11
- Rheenen J van, Mulugeta Achame E, Janssen H, Calafat J, Jalink K (2005): PIP2 Signaling in Lipid Domains: A Critical Re-Evaluation. *EMBO J* 24, 1664–73
- Rizzoli S. O. (2014): Synaptic Vesicle Recycling: Steps and Principles. *EMBO J* 33, 788–822
- Rizzoli Silvio O., Betz WJ (2005): Synaptic Vesicle Pools. *Nat Rev Neurosci* 6, 57–69
- Rogge A, Flintrop CM, Iversen MH, Salter I, Fong AA, Vogts A, Waite AM (2018): Hard and Soft Plastic Resin Embedding for Single-Cell Element Uptake Investigations of Marine-Snow-Associated Microorganisms Using Nano-Scale Secondary Ion Mass Spectrometry. *Limnol Oceanogr Methods* 16, 484–503
- Rohrbough J, Broadie K (2005): Lipid Regulation of the Synaptic Vesicle Cycle. *Nat Rev Neurosci* 6, 139–50
- Rolandi R, Robello M, Mao C, Mainardi P, Besio G (1990): Adsorption of  $\gamma$ -Aminobutyric Acid to Phosphatidylserine Membranes. *Cell Biophys* 16, 71
- Rosen H, Goetzl EJ (2005): Sphingosine 1-Phosphate and Its Receptors: An Autocrine and Paracrine Network. *Nat Rev Immunol* 5, 560–70

- Rostaing P, Weimer RM, Jorgensen EM, Triller A, Bessereau J-L (2004): Preservation of Immunoreactivity and Fine Structure of Adult *C. Elegans* Tissues Using High-Pressure Freezing. *J Histochem Cytochem* 52, 1–12
- Rueden CT, Schindelin J, Hiner MC, DeZonia BE, Walter AE, Arena ET, Eliceiri KW (2017): ImageJ2: ImageJ for the next Generation of Scientific Image Data. *BMC Bioinformatics* 18, 529
- Saka SK, Vogts A, Kröhnert K, Hillion F, Rizzoli SO, Wessels JT (2014): Correlated Optical and Isotopic Nanoscopy. *Nat Commun* 5, 3664
- Schnell U, Dijk F, Sjollem KA, Giepmans BNG (2012): Immunolabeling Artifacts and the Need for Live-Cell Imaging. *Nat Methods* 9, 152–58
- Schumacher D, Helma J, Schneider AFL, Leonhardt H, Hackenberger CPR (2018): Nanobodies: Chemical Functionalization Strategies and Intracellular Applications. *Angew Chemie Int Ed* 57, 2314–33
- Scigelova M, Makarov A (2006): Orbitrap Mass Analyzer - Overview and Applications in Proteomics. *Proteomics* 6, 16–21
- Senyo SE, Steinhauser ML, Pizzimenti CL, Yang VK, Cai L, Wang M, Wu T Di, Guerquin-Kern JL, Lechene CP, Lee RT (2013): Mammalian Heart Renewal by Pre-Existing Cardiomyocytes. *Nature* 493, 433–36
- Shamim A, Mahmood T, Ahsan F, Kumar A, Bagga P (2018): Lipids: An Insight into the Neurodegenerative Disorders. *Clin Nutr Exp* 20, 1–19
- Silva LC, Almeida RFM de, Castro BM, Fedorov A, Prieto M (2007): Ceramide-Domain Formation and Collapse in Lipid Rafts: Membrane Reorganization by an Apoptotic Lipid. *Biophys J* 92, 502–16
- Sims P.A., Hardin J.D: Fluorescence-Integrated Transmission Electron Microscopy Images. In: Kuo J. (Eds.): *Methods in Molecular Biology*, Humana Press, New Jersey 2007, vol 369, 291-308
- Singh AV, Jungnickel H, Leibrock L, Tentschert J, Reichardt P, Katz A, Laux P, Luch A (2020): ToF-SIMS 3D Imaging Unveils Important Insights on the Cellular Microenvironment during Biomineralization of Gold Nanostructures. *Sci Rep* 10, 261
- Sjövall P, Johansson B, Lausmaa J (2006): Localization of Lipids in Freeze-Dried Mouse Brain Sections by Imaging TOF-SIMS. *Appl Surf Sci* 252, 6966–74
- Smith JE, Reese TS (1980): Use of Aldehyde Fixatives to Determine the Rate of Synaptic Transmitter Release. *J Exp Biol* 89, 19–29
- Snaidero N, Möbius W, Czopka T, Hekking LHP, Mathisen C, Verkleij D, Goebbels S, Edgar J, Merkler D, Lyons DA et al. (2014): Myelin Membrane Wrapping of CNS Axons by PI(3,4,5)P3-Dependent Polarized Growth at the Inner Tongue. *Cell* 156, 277–90
- Sograte-Idrissi S: Optimization of Tools for Multiplexed Super Resolution Imaging of the Synapse. Dissertation University Medical Center Göttingen, 2019
- Sograte-Idrissi S, Schlichthaerle T, Duque-Afonso CJ, Alevra M, Strauss S, Moser T, Jungmann R, Rizzoli SO, Opazo F (2020): Circumvention of Common Labelling Artefacts Using Secondary Nanobodies. *Nanoscale* 12, 10226–39
- Spiegel S, Milstien S (1995): Sphingolipid Metabolites: Members of a New Class of Lipid Second Messengers. *J Membr Biol* 146, 225–37
- Stadelmann C, Timmler S, Barrantes-Freer A, Simons M (2019): Myelin in the Central Nervous System: Structure, Function, and Pathology. *Physiol Rev* 99, 1381–1431
- Staunton J, Weissman KJ (2001): Polyketide Biosynthesis: A Millennium Review. *Nat Prod Rep* 18, 380-416

- Steinhauser ML, Lechene CP (2013): Quantitative Imaging of Subcellular Metabolism with Stable Isotopes and Multi-Isotope Imaging Mass Spectrometry. *Semin Cell Dev Biol* 24, 661–67
- Stephenson DJ, Hoeflerlin LA, Chalfant CE (2017): Lipidomics in Translational Research and the Clinical Significance of Lipid-Based Biomarkers. *Transl Res* 189, November 13–29
- Sud M, Fahy E, Cotter D, Brown A, Dennis EA, Glass CK, Merrill AH, Murphy RC, Raetz CRH, Russell DW et al. (2007): LMSD: LIPID MAPS Structure Database. *Nucleic Acids Res* 35, D527–32
- Tanaka KAK, Suzuki KGN, Shirai YM, Shibutani ST, Miyahara MSH, Tsuboi H, Yahara M, Yoshimura A, Mayor S, Fujiwara TK et al. (2010): Membrane Molecules Mobile Even after Chemical Fixation. *Nat Methods* 7, 865–66
- Tanguy E, Wang Q, Moine H, Vitale N (2019): Phosphatidic Acid: From Pleiotropic Functions to Neuronal Pathology. *Front Cell Neurosci* 13, 2
- Tettey P, Mei IA van der (2014): Lipids in Multiple Sclerosis: Adverse Lipid Profiles, Disability and Disease Progression. *Clin Lipidol* 9, 473–75
- Thiery-Lavenant G, Guillermier C, Wang M, Lechene C (2014): Detection of Immunolabels with Multi-Isotope Imaging Mass Spectrometry. *Surf Interface Anal* 46, 147–49
- Tian H, Maciążek D, Postawa Z, Garrison BJ, Winograd N (2016): CO<sub>2</sub>Cluster Ion Beam, an Alternative Projectile for Secondary Ion Mass Spectrometry. *J Am Soc Mass Spectrom* 27, 1476–82
- Tian H, Six DA, Krucker T, Leeds JA, Winograd N (2017): Subcellular Chemical Imaging of Antibiotics in Single Bacteria Using C 60 -Secondary Ion Mass Spectrometry. *Anal Chem* 89, 5050–57
- Toyama BH, Savas JN, Park SK, Harris MS, Ingolia NT, Yates JR, Hetzer MW (2013): Identification of Long-Lived Proteins Reveals Exceptional Stability of Essential Cellular Structures. *Cell* 154, 971–82
- Toyama BH, Arrojo e Drigo R, Lev-Ram V, Ramachandra R, Deerinck TJ, Lechene C, Ellisman MH, Hetzer MW (2019): Visualization of Long-Lived Proteins Reveals Age Mosaicism within Nuclei of Postmitotic Cells. *J Cell Biol* 218, 433–44
- Tracey TJ, Steyn FJ, Wolvetang EJ, Ngo ST (2018): Neuronal Lipid Metabolism: Multiple Pathways Driving Functional Outcomes in Health and Disease. *Front Mol Neurosci* 11, 10
- Truckenbrodt S, Viplav A, Jähne S, Vogts A, Denker A, Wildhagen H, Fornasiero EF, Rizzoli SO (2018): Newly Produced Synaptic Vesicle Proteins Are Preferentially Used in Synaptic Transmission. *EMBO J* 37, e98044
- Turrigiano GG, Leslie KR, Desai NS, Rutherford LC, Nelson SB (1998): Activity-Dependent Scaling of Quantal Amplitude in Neocortical Neurons. *Nature* 391, 892–96
- Urban NT, Foreman MR, Hell SW, Sivan Y (2018): Nanoparticle-Assisted STED Nanoscopy with Gold Nanospheres. *ACS Photonics* 5, 2574–83
- Vance JE (2008): Thematic Review Series: Glycerolipids. Phosphatidylserine and Phosphatidylethanolamine in Mammalian Cells: Two Metabolically Related Aminophospholipids. *J Lipid Res* 49, 1377–87
- Vaqas B, Balog J, Roncaroli F, Takats Z, O'Neill K (2015): Abstract LB-287: IKnife in Neurosurgery: Intraoperative Real-Time, in Vivo Biochemical Characterization of Brain Tumors with High Spatial Resolution. *Cancer Res* 75, LB-287
- Vázquez L, Corzo-Martínez M, Arranz-Martínez P, Barroso E, Reglero G and Torres C: Bioactive Lipids. In: Mérillon JM., Ramawat K. (Eds.) *Bioactive Molecules in Food*. Springer International Publishing 2018, 1–61
- Voelker DR (1990): Lipid Transport Pathways in Mammalian Cells. *Experientia* 46, 569–79

- Voelker DR: Glycerolipid Structure, Function, and Synthesis in Eukaryotes. In: William LJ and Lane MD Encyclopedia of Biological Chemistry. 2<sup>nd</sup> edition; Academic Press, Massachusetts. 2013, 412–18
- Vreja IC, Kabatas S, Saka SK, Kröhnert K, Höschel C, Opazo F, Diederichsen U, Rizzoli SO (2015): Secondary-Ion Mass Spectrometry of Genetically Encoded Targets. *Angew Chemie Int Ed* **54**, 5784–88
- Wang Q, Chan TR, Hilgraf R, Fokin V V., Sharpless KB, Finn MG (2003): Bioconjugation by Copper(I)-Catalyzed Azide-Alkyne [3 + 2] Cycloaddition. *J Am Chem Soc* **125**, 3192–93
- Weber M, Leutenegger M, Stoldt S, Jakobs S, Mihaila TS, Butkevich AN, Hell SW (2021): MINSTED Fluorescence Localization and Nanoscopy. *Nat Photonics* **15**, 361–66
- Weil M-T, Ruhwedel T, Meschkat M, Sadowski B and Möbius W: Transmission Electron Microscopy of Oligodendrocytes and Myelin. In: Lyons D, Kegel L (Eds.) *Oligodendrocytes. Methods in Molecular Biology*. Humana Press, New York 2019
- Wilde PJ: Lipid Digestion and Absorption. In: Reference Module in Biomedical Sciences. Elsevier, Amsterdam 2014
- Wilson RL, Frisz JF, Hanafin WP, Carpenter KJ, Hutcheon ID, Weber PK, Kraft ML (2012): Fluorinated Colloidal Gold Immunolabels for Imaging Select Proteins in Parallel with Lipids Using High-Resolution Secondary Ion Mass Spectrometry. *Bioconjug Chem* **23**, 450–60
- Winograd N (2018): Gas Cluster Ion Beams for Secondary Ion Mass Spectrometry. *Annu Rev Anal Chem* **11**, 29–48
- Winograd N, Postawa Z, Cheng J, Szakal C, Kozole J, Garrison BJ (2006): Improvements in SIMS Continue. Is the End in Sight? *Appl Surf Sci* **252**, 6836–43
- Yang S-T, Kreutzberger AJB, Lee J, Kiessling V, Tamm LK (2016): The Role of Cholesterol in Membrane Fusion. *Chem Phys Lipids* **199**, 136–43
- Yoon S, Lee TG (2018): Biological Tissue Sample Preparation for Time-of-Flight Secondary Ion Mass Spectrometry (ToF-SIMS) Imaging. *Nano Converg* **5**, 24
- Zhang J: Amphiphilic Molecules. In: Drioli E and Giorno L (Eds.) *Encyclopedia of Membranes*. Springer Berlin/Heidelberg 2016, 72–75
- Zhang YH, Vasko MR, Nicol GD (2002): Ceramide, a Putative Second Messenger for Nerve Growth Factor, Modulates the TTX-resistant Na<sup>+</sup> Current and Delayed Rectifier K<sup>+</sup> Current in Rat Sensory Neurons. *J Physiol* **544**, 385–402

## ACKNOWLEDGEMENTS

---

First, I would like to thank my two supervisors, Prof. Silvio Rizzoli and Dr. Nhu Phan for giving me the opportunity to work in such a great environment and getting involved in all these exciting projects. I really appreciate how you both have guided me through these years sharing with me your experience and knowledge and teaching me how to deal with a completely new world and all the challenges that came with it.

I would also like to thank Dr. Felipe Opazo and Dr. Livia de Hoz for their support in my very initial steps working in a lab, sharing with me your scientific passion and experience, and being patient enough to deal with a totally naive student. Thanks to you both I felt inspired and encouraged to pursue this path.

Thanks to the entire Rizzoli lab because directly or indirectly you have all contributed to this work as well as to my personal and professional growth. In particular, I would like to thank Dr. Shama Sograte Idrissi, Dr. Selda Kabatas, Dr. Manuel Maidorn, Dr. Angela Gomes de Castro, and Natalia Waal for all the insights and motivation provided from the very beginning. Also, thanks to Dr. Eugenio Fornasiero and Dr. Sebastian Jähne for the scientific discussions and for the uncountable times that you patiently answered my random questions. I would also like to thank the members of our small NanoSIMS family, but especially Katharina Grewe for being always there, supporting us and putting out all the fires. Thanks to all the technicians, collaborators, and colleagues that have been involved in the work here presented, and special thanks to Anita-Karina Jaehnke, Christin Wiemuth, Regina Sommer-Kluß, and Omar Díaz for being always so accessible and helpful with the bureaucratic and IT difficulties.

Facing a doctorate has been pretty hard sometimes but having you all around made everything easier and nicer. Thank you so much!

## CURRICULUM VITAE

---

Paola Agüi González was born in Santa Cruz de Tenerife (Canary Islands, Spain) on the 29th of October 1990. In September 2008, she began her medical studies at the University of La Laguna (Santa Cruz de Tenerife, Spain), finishing the degree in September 2016, after accomplishing the clinical rotation year at the Hospital of S. Maria della Misericordia in Perugia (Italy). To gain some experience in the lab, from September to December 2016, she did an internship at the Cognitive Neurophysiology Lab in the Max Planck Institute for Experimental Medicine (Göttingen, Germany) under the supervision of Dr. Livia de Hoz. Then, from April 2017 to October 2017, she worked as a Research Assistant at the Molecular Probes for Quantitative Neurosciences Lab, (University Medical Center Göttingen, Germany) under the supervision of Dr. Felipe Opazo. Immediately after, in October 2017, she joined the Department of Neuro- and Sensory Physiology, University Medical Center (Göttingen, Germany) as a Research Assistant until she began her Doctor of Medicine studies in June 2018.

Her doctoral research (June 2018 – June 2022), was supervised by Prof. Silvio O. Rizzoli and Dr. T.N. Nhu Phan. The research was mainly performed in the Department of Neuro- and Sensory Physiology, and the Center for Biostructural Imaging of Neurodegeneration (BIN), both at the University Medical Center (Göttingen, Germany). She also visited the Department of Chemistry and Molecular Biology at the University of Gothenburg (Sweden) to perform the analysis of the samples with ToF-SIMS. In parallel, since November 2021, she is pursuing an online master's in clinical Trials Monitoring and Pharmaceutical Development, at the University of Antonio de Nebrija (Madrid, Spain).

In addition to the ones included on her thesis, during her doctoral studies she co-authored further scientific publications:

Kabatas Glowacki S\*, **Agüi-Gonzalez P\***, Sograte-Idrissi S, Jähne S, Opazo F, Phan NTN, Rizzoli, SO (2022): An iodine-containing probe as a tool for molecular detection in secondary ion mass spectrometry. *Chem Commun* 58, 7558-7561

Dankovich TM, Kaushik R, Olsthoorn LHM, Petersen GC, Giro PE, Kluever V, **Agüi-Gonzalez P**, Grewe K, Bao G, Beuermann S et al. (2021): Extracellular Matrix Remodeling through Endocytosis and Resurfacing of Tenascin-R. *Nat Commun* 12, 1–23

Jähne S, Mikulasch F, Heuer HGH, Truckenbrodt S, **Agüi-Gonzalez P**, Grewe K, Vogts A, Rizzoli SO, Priesemann V (2021): Presynaptic Activity and Protein Turnover Are Correlated at the Single-Synapse Level. *Cell Rep* 34, 108841

*\*both authors contributed equally to this work*